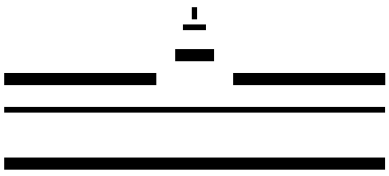

WESTFÄLISCHE
WILHELMS-UNIVERSITÄT
MÜNSTER

# Comparing the complete and the point electrode model for combining tCS and EEG

– Masterarbeit –


Westfälische Wilhelms-Universität Münster
Fachbereich Mathematik und Informatik

**Betreuer:** Carsten Wolters [1]
Sampsa Pursiainen [2]

**Gutachter:** Martin Burger [3]
Sampsa Pursiainen[2]

**Eingereicht von:** Britte Agsten


Münster, 16. März 2015


[1]Institut für Biomagnetismus und Biosignalanalyse, WWU Münster
[2]Department of Mathematics and System Analysis, Aalto University, Finnland
[3]Institut für Numerische und Angewandte Mathematik, WWU Münster

# Abstract

This work compares two different models for current density modeling and EEG measurements in combined transcranial current stimulation (tCS) and electroencephalography (EEG).
The first one, the point electrode model (PEM) for EEG in combination with a complex form of the gap model for the tCS, is the current standard for forward simulations in EEG and tES. The other one, the complete electrode model (CEM), describes a more detailed model which incorporates shunting effects in the electrodes, i.e. a current circulation between the electrode and the head. It was the question of interest if the simulations using the CEM differ significantly from the standard simulations. For the normal EEG this question was already investigated before and answered negatively. However, stimulation currents are much higher than currents due to brain sources. Therefore, if one wants to compute artifacts in the EEG due to the tES stimulation, even little differences might matter if compared to the actual brain activity.
In this work, those differences were explored numerically using the finite element method (FEM) in combination with a highly realistic head model. The results revealed that the differences are very small compared to the actual strength of the applied current. This holds even more for the current distribution inside of the head, where differences occur rather next to the electrodes than inside of the brain and are small if they exist. However, results differ significantly if compared to potentials evoked by brain activity. This shows that the more accurate CEM will be relevant if tES forward simulations are combined with real EEG measurements in the future.

# Acknowledgements

I would like to thank Carsten Wolters and Sampsa Pursiainen, my research supervisors, for their very nice and helpful support and for giving me the opportunity to work on this very interesting topic. I do not take it for granted to work with people who are such enthusiastic about their profession.
Moreover, I would like to thank Sven Wagner, for his helpful advice and assistance and for co-reading this work.
Special thanks go also to my parents, for their patient support and encouragement throughout my study.
Thanks to Florian for his great emotional and intellectual support and for looking over this thesis as well, this work couldn't have been done without you.
Finally, I want to thank Yann and David for giving me some final and valuable tips.

# Contents

# 1. Introduction

Non-invasive brain stimulation (NIBS) has become an important instrument in both medical therapy and neurological research [25]. It is known for quite a while that different brain activities are always accomponied by corresponding brain oscillations, at which localization, strength and frequency differ for different activities. This can be recorded via electroencephalography (EEG). However, normal measurements could never reveal if those correlations are due to a causal link [13]. This is why causality has been classically investigated using patients with specific neurological disorders.
Since brain stimulations aim to manipulate brain currents in a controlled way, they give a new opportunity to investigate those causalities. With the help of stimulation one now has the opportunity to show that generated brain activity can directly influence cognitive processes [13, 25]. Moreover, systematic stimulation can also induce long-term effects on brain activity [35], which holds for TMS as well as for tES. This is the foundation of a lot of new therapies for neurological diseases, such like depression [29], Parkinson's disease [9, 19], Alzheimer's disease [43, 2], stroke [7, 54] or memory loss [17]. It is also shown that NIBS might help in the treatment of chronical pain [20].

A promising and - in its current form - relatively new method of brain stimulation is transcranial electric stimulation (tES). In this technique, in use of two or more scalp electrodes attached to the skin, a low current is applied to the head. It has been shown that parts of this current pass the skull and are able to increase or decrease cerebral excitability [25].
Early methods of tES were already used at the beginning of the 20th century, when electric pulses were applied to induce a sleep-like state in the subject, also called electrosleep [11]. Since then a lot of different forms of tES have been developed [11]. A basis for the contemporary form of the tES was laid at the end of the last century, when it was found that applied direct current can produce long-lasting effects on the brain. (Priori et al. 1998 [37], Nitsche and Paulus 2000 [28]). Modern forms developed since then can be differed by their wave forms, including at least direct, alternating and random noise currents (tDCS, tACS and tRNS) [35, 11].
An obvious, yet important advantage of tES is its painless and non-invasive application [28]. Moreover, because tACS can directly apply certain frequencies, it does not entrain additional frequencies present in pulsed stimulation like repetitive transcranial stimulation (rTMS) [13], [50]. It is also a quiet form of stimulation and does not generate disturbing factors like noise [13].

To investigate the reaction of the brain to systematic changes in brain oscillations one often combines tES and EEG measurements (see e.g. [12, 57]). However, a disturbing

factor is the occurence of strong artifacts in the EEG measurements due to the stimulation itself.
This thesis aims to compare two different numerical modeling approaches to simulate those artifacts. One of these models is the point electrode model (PEM), which is the current standard model in EEG: It simply assumes, that each electrode is a passive point on the surface of the head .
The other model chooses a more complex approach: Since electrodes are in fact no neutral elements, but have certain electric properties themselves, they can influence the current distribution in the head. This influence occurs due to "'shunting effects"' in the electrodes. The complete electrode model (CEM) takes those shunting effects into account. It was originally developed for the electrical impedance tomography (EIT) (see e.g. [51]) and has already been applied to the EEG forward simulation previously [33, 39]. However, it was shown in [39], that differences between PEM and CEM are very small in context of the normal EEG.
Given this result, the question arises if these effects might be relevant in combined EEG and tES stimulation anyway. This idea is based on the fact that the applied currents in the tES (e.g.$1\,mA$) are usually much stronger than those evoked by brain activity (e.g.$50\,nAm$). Therefore small errors concerning the artifacts may already be significant when compared to the magnitude of brain currents.

The work is mainly based on a code which was originally developed for the comparison of CEM and PEM concerning lead field matrices in EEG and was used in [39]. It was modified to simulate the potential distribution and the EEG measurements for combined EEG and tES instead.
Simulations were done using a highly realistic six compartment head model. An electrode configuration of 77 electrodes was attached to the head. Two additional electrodes were placed above the ears, serving as anode and cathode. Skin and electrode potentials as well as currents in the head were then simulated for a total current of $1mA$.
The results show that all models lead to similar distributions of currents and potentials. Similarity holds especially for current distributions in the head, suggesting that the use of CEM and PEM does not lead to significant differences in the forward simulation of normal tES. Distribution differences mainly occur next to the EEG electrodes. The simulations of EEG measurements delivered only small differences as well, if the errors were compared to the overall magnitude of the potentials. However, if the measurement errors were compared to potentials evoked by brain activity they became highly significant. This suggests that for an accurate forward simulation of tES evoked artifacts in the EEG the CEM should be incorporated in the future.

The thesis is organized as follows: Chapter 2 gives the most important background information, including a few neurological basics, a short introduction to electromagnetic fields, as well as further information about the function of tES and EEG. The latter part includes information about the lead field matrix $L$, which plays an important role in EEG forward modelling and a more vivid explanation of the shunting effects.
Chapter 3 gives a detailed mathematical description of the different approaches, covering the underlying equations as well as the weak forms of the different models. Chapter 4

describes the numerical approach, i.e. the FEM discretization and a short description of the original code and the modifications that were made.
The numerical experiments are explained in Chapter 5, followed by a detailed presentation of the results in Chapter 6. Finally the discussion is given in chapter 7.
The appendix includes additional information like important mathematical basics and a proof that the described models have a unique solution. Moreover, the attached CD includes the basic code as well as all data and some additional programs as supplementary material.

# 2. Background information

## 2.1. Neurological Basics

The first section shall give a short overview about neurological basics. In preparation for Chapter 5 and 6, Section 2.1.1 and Section 2.1.2 give a very rough description of the most important tissues and structures of the brain. However, this part is primarily supposed to give an idea of electrical activity in the brain and thereby of the functioning of tES and EEG.

### 2.1.1. The brain and its cells

The human brain is a highly complex structure. It consists of a large number of smaller and highly specialized parts, which are able to control basic bodily functions as well as higher cognitive processes. Next to the spinal cord it forms a main part of the central nervous system, which is responsible for the management of nearly all information gathered in the human body [41].

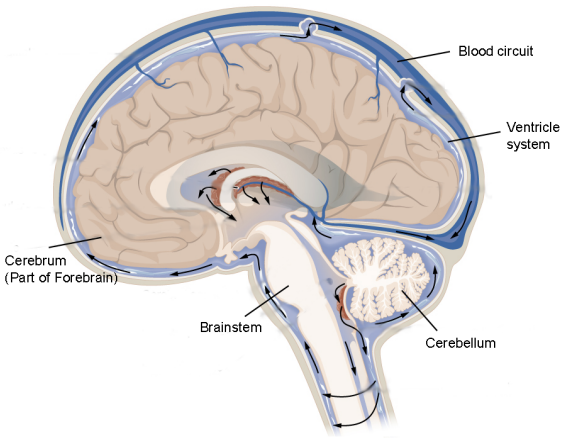


***Figure 2.1.:*** *sagittal cut through the brain, showing main parts and structures of the brain, picture source: wikimedia*

The brain mainly consists of neuronal tissue, which is basically characterized by a complex network of *neurons*.
Neurons are highly specialized cells which are responsible for all kinds of information processing in the body. Their main function is the communication with other neurons, which can be realized through a large number of connections between the cells. Information is transferred via the axons, long extensions of the cells, which serve as a conductor for short electric waves - the action potentials. Each axon is connected to another nerve cell which receives the information. Information will either inhibit or excite a new action potential in the target neuron [41]. This way neurons can form complex information patterns. (Section 2.1.3 will give a more detailed overview about neuronal

signals.)
However, neurons are not the only cells of neural tissue. There is also a number of supporting cell, which can be found in the tissue, the *glia cells*. These are even more numerous in neural tissue and have different functions, as there are different types of these cells. One of the most prominent types is given by the *Oligodendrocytes*, which lay a lipid-rich wrapping around some axons. This wrapping is called myelin and improve the current flow along an axon [41]. It is because of the myelin at important axons that neuronal tissue is often subdivided into two different main parts: *white matter* is tissue, which is rich in axons (because - due to the lipid - it has a light appearance in examined brains) and *gray matter* which refers to tissue rich in cell bodies.

Neuronal tissue in the brain is interspersed with other structures, like blood vessels and the ventricle system. The latter one describes a system of spaces, which are filled with the so-called cerebrospinalfluid(CSF). This clear liquor circulates through the brain and - besides having diverse regulating functions - serves as a buffer between brain and skull [49].

### 2.1.2. Functional structure of the brain

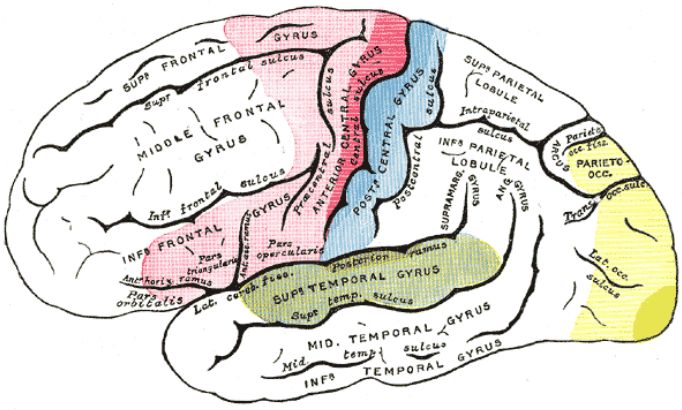


***Figure 2.2.:*** *Primary cortices in the brain, Red: Motor cortices, Blue: Somato sensory centers, Green: Auditory centers, Yellow: Visual centers (source: wikimedia)*

As already indicated above, the brain consists of many different parts which are locally specialized into different brain functions. The most obvious subdivision is the seperation into the three main parts, namely brainstem, cerebellum and forebrain (cf. fig. 2.1). While the first two are responsible for processes like life-sustaining functions (brainstem) or coordination and learning (cerebellum), all higher and conscious brain functions can be localized in the forebrain [41]. It is not the topic of this thesis to explain the organization of the brain in detail, but localization of brain functions is obviously of great relevance in a targeted stimulation of the brain. Therefore, this part shall at least give a short overview about the neocortex, which is the the youngest and most organized part of the forebrain and represents the main part of the cerebral hemispheres [49]:
The neurocortex can be roughly divided into three different parts: The primary cortices, the secondary cortices and the association cortices [49]. The first term describes those parts of the cortex which are directly linked to sensory information and motorical

processes - including the visual system, the auditory system, the somato sensory system and the motor system. Primary cortices are responsible for all processes which deal with pure sensory information, i.e. all processes which do not include interpretation in any way. In contrast, evaluative processes concerning sensory information are localized in the correspondent secondary cortices of the brain, which are normally localized next to the primary centers [49]. Finally, the association cortices describe all cortices which cannot be linked to sensory informations but reorganize information from different parts in the neocortex.
In contemporary tES studies the investigation of primary cortices is very prominent. This is due to the fact that stimulation of the corresponding centers can be directly linked to behavior or sensory experience in those areas. For instance, the first studies concerning tES concentrated on the excitability of the primary motor cortex, which is important for the control of movement [37], [28].

### 2.1.3. How can electrical currents reflect and influence brain activity?

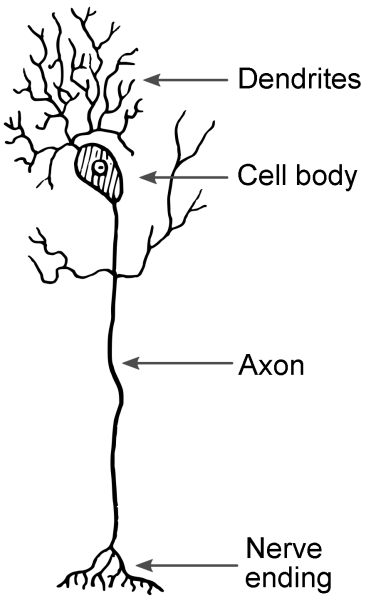


***Figure 2.3.:*** *Illustration of a typical nerve cell (source:wikimedia)*

The functioning of EEG and tES both relies on the fact that brain activity can be reflected by electrical currents. This section shall give a deeper insight into the mechanism of electrical currents in the brain. Section 2.1.1 already stated that electric activity in neuronal tissue is given by action potentials travelling along the axons of the neurons, and one could assume these to be the currents measured by an EEG. However, electrical activity in the brain is more complex and therefore we need to take a closer look at the mechanism of neuronal activity:

Fig. 2.3 gives an exemplified impression of a typical structure of a neuron.[1] Neurons gather information at the dendritic branches arising from their cell body, while information is forwarded by the axon, a unique extension that is linked to the dendrite of another cell. The link between dendrite and axon is called the *synapse* (cf. figure 2.4).
The transfer of information at synapses is given by biochemical processes occuring at the pre- and postsynaptic membran, i.e. the membrans of axon

[1] The cells in nervous tissue (neurons as well as the supporting glia cells) form the most variable cell type in the human body, since they are highly specialized. For example, the numbers of dendrites or length of the axon differ strongly [41].

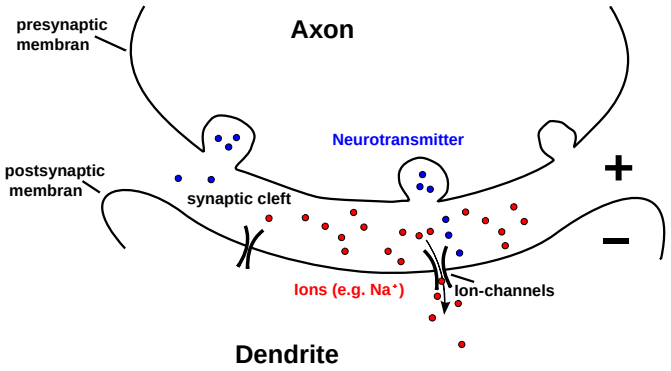


***Figure 2.4.:*** *Formation of postsynaptic potentials - (freely adapted from [16])*

and dendrite. In the synaptic cleft (the space between the cells), as well as in the involved cells, a number of different ions ($Na^+, Ca^{2+}, K^+Cl^-$) can be found. However, in the resting state of the synapse the distribution of those ions is in an unbalanced state. While the inside of the target neuron is mainly dominated by potassium-ions ($K^+$), the synaptic cleft contains more sodium ($Na^+$) and chlorid ($Cl^-$). This does not only lead to a concentration gradient, but also to a difference in electric potential. Therefore, in its resting state there is a negative potential gradient between target neuron and the outside of the cell [16].
If an action potential is triggered and reaches the end of the axon, several neurotransmitters (e.g. glutamate) will be released, which open ion channels in the postsynaptic membran (cf. figure 2.4). Ion channels are selective openings specialized to one sort of ions, which are allowed to pass the channel. Due to diffusion processes those ions will travel along their concentration gradient as soon as the channel is open. This effect changes the electric potential inside of the target neuron: If $K^+$ is released into the synaptic cleft or $Cl^-$ flows into the cell, the potential inside of the neuron decreases even more (hyperpolarization). However, if sodium flows into the cell, the cell gets depolarized. The sum of postsynaptic potentials (PSPs) now decides wether an action potential is triggered at the axon hillock (the part of the neuron which is located where the axon emerges from the cell). If the depolarization is strong enough to reach a certain threshold, a wave of depolarization - the action potential - will be triggered and move down the axon. Therefore, the depolarizating potentials are also called excitatory PSPs (EPSPs), while the hyperpolarizationg potentials are called inhibitory PSPs (IPSPs).

### Reflecting brain activity (EEG)

The processes described above deliver two different forms of electric activity which can be detected in the brain: action potentials and PSPs (cf. figure 2.5).
The first one - the action potential - represents a very short current change in the involved axons ($\sim 1ms$). It is followed by a wave of repolarization of longer spatial extent

[14, 22].
PSPs on the other hand are much weaker than the action potential, but have a much larger latency [14]. They are supposed to cause a current dipole around the involved neuron, because they change the extracellular charges at the synapses, while positive charges flow in direction of the cell body [22].

Although action potentials are much stronger than PSPs, it is assumed that current activity measured by the EEG arises mainly from the PSPs [14, 22]. This is mainly because the former last not long enough to be identified: Because of their short appearance and the repolarization wave, it is very unlikely that currents of adjacent axons summate, since they would have to occur at exactly the same time[2]. It is more likely that neurons fire slightly after each other, which leads to the effect that they cancel each other [22]. Therefore, one assumes that EEG signals mainly occur due to PSPs. [14, 22].

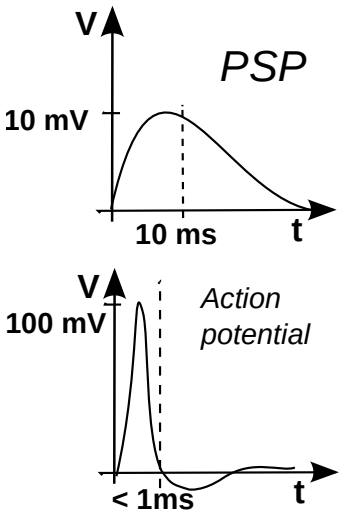


***Figure 2.5.:*** *Comparison of action potentials and PSP*

### Influencing brain activity (tES)

Similar to the EEG, tES has an effect on PSPs, but not directly on action potentials. In contrast to TMS, which can indeed induce currents high enough to trigger action potentials of resting neurons, the applied currents due to tES are too weak to do so. However, it was shown that tDCS can increase or decrease the cortical excitability [28]. It is assumed that those influences are due to spontaneous and long-lasting effects on the membran potentials described above [35, 21].

## 2.2. Maxwell equations and quasi-static approach

To find an appropriate model for the phenomena inside of the head we need a basic idea of electromagnetism. Electromagnetism is a branch of physics which studies the behavior of electric and magnetic fields. Those fields cannot be studied independently, because they strongly influence each other, if they change their behavior over time. This is why one the term *electrodynamics* is often used here.
However, for steady electric or magnetic fields those phenomena can be studied separately as it is done in *electrostatics* and *magnetostatics*.
Fortunately, one can assume a nearly static behavior of electromagnetic fields as soon

[2]However, it is of course possible to measure action potentials with other methods, e.g. by microelectrodes inserted into the brain [22]

as the frequencies are low enough, which is normally fulfilled in brain modelling. This is called the *quasi-static approach* and highly simplifies our work here.

The quasi-static approach is based on the *Maxwell equations*, which play a prominent role in electromagnetism. Hence they are been described in the first paragraph. We will also learn about certain properties a tissue should have in order to work with these equations properly. We will then give a short introduction to the quasi-static approach.

### 2.2.1. Maxwell equations

In combination with the *Lorentz equation*[3], the Maxwell equations form the fundament of electromagnetism. While the Lorentz equation describes the magnetic and electrical forces on a moving charge, the latter describe the relationship between electrical and magnetic forces [31]. Those equation are as follows:

| | **Microscopic Case** | **Macroscopic Case** | |
|---|---|---|---|
| Gauss's Law | $\nabla \cdot E = \frac{\rho_t}{\epsilon_0}$ | $\nabla \cdot D = \rho$ | (2.1) |
| Maxwell-Faraday equation | $\nabla \times E = -\frac{\partial B}{\partial t}$ | $\nabla \times E = -\dfrac{\partial B}{\partial t}$ | (2.2) |
| Gauss's Law for magnetism | $\nabla \cdot B = 0$ | $\nabla \cdot B = 0$ | (2.3) |
| Maxwell-Ampere equation | $\nabla \times B = \frac{J_t}{\epsilon_0 c^2} + \frac{1}{c^2}\frac{\partial E}{\partial t}$ | $\nabla \times H = J + \dfrac{\partial D}{\partial t}$ | (2.4) |

We see that there are in fact two different versions of the Maxwell equations. The microscopic equations describe electromagnetical forces on electrical charges in every detail on a very low level and unaffected of tissue effects, i.e. in vacuum. However, for a proper model in tissues this would mean that we had to take every factor and every charge of the tissue into account, even on a atomar level, which is clearly not possible under most circumstances (and cannot be calculated without quantum mechanics). Hence there is a simplification at a macroscopic level. It is the idea here that - although there are a lot of tiny forces in the fields we do not know - there is a overall behavior of the fields if we look at the tissue in its entirety [31].

The equations mainly describe the interactions of the electrical fields $E$ and $D$ and the magnetic forces $B$ and $H$ with the current density $J$ and the charge density $\rho$.
In short the *electrical field* $E$ is a vector field describing the force due to charges (or magnetic fields) in the tissue. It mainly acts on other surrounding static charges. The *magnetic induction* $B$ on the other hand describes the magnetic force density due to a current carrying conductor or another magnet. This field only acts on moving charges,

[3] described by Hendrik A. Lorentz. This should not be confused with the *Lorenz gauge condition* (Ludvig Lorenz), which is also important in electromagnetism, especially in matters of the quasi-static approach

e.g. another current carrying medium [30].
Currents are represented in form of the current density $J$, i.e. a vector field describing the current per area. The charge density $\rho$ is a vector field as well, symbolizing the charge per area.

In the macroscopic case the electric field $E$ is partly displaced by the *electric displacement field* $D$. Similarly the magnetic induction $B$ is partly displaced by the *magnetic field intensity* $H$. These are macroscopic measurements, helping to describe the macroscopic fields properly. The important thing about those new fields is the fact that they take material effects (dielectric effects and material magnetism) into account, which were not relevant in the microscopic case [31]. Those fields describe the electric and magnetic forces in a slightly different way, therefore they are measured in other units than the fields $E$ and $B$. Hence, units of equations 2.1 and 2.4 change as well.

### Some important tissue properties

If we look at the macroscopic equations we notice that with $D$ and $H$ we have two more unknown vector fields here. To work with the equations properly we need further information about the connection between the relevant fields. This is were it is advantageous for the tissue to fullfill certain conditions, namely to be an *linear dielectric*, *linear conductive* and *linear magnetic* medium [31]. Mathematically this means that the behavior of the fields $D$, $H$ and $J$ can be assumed to be proportional to the fields $E$ or $B$:

$$\text{linear dielectric:} \quad D = \epsilon E \tag{2.5}$$
$$\text{linear conductive:} \quad J = \sigma E \tag{2.6}$$
$$\text{linear magnetic:} \quad H = \mu B \tag{2.7}$$

In each case the relationship is characterized by a certain material-dependent parameter. These are: The *permittivity* $\epsilon$, the *conductivity* $\sigma$ and the *magnetic permeability* $\mu$.
One can assume such a linear behavior for most living tissues [31]. Anyway, all these parameters can be auxiliary parameters at most, as they give just an approximated description of the macroscopic behavior of the tissues. They describe certain phenomena concerning the distribution of charges in a macroscopic tissue. For example, the dielectric constant (or permittivity) $\epsilon$ can give a rough description of polarities occuring in a tissue if charges are bound to a certain place, like it is the case for electrons and protons of a fixed atom. On the other hand, the conductivity $\sigma$ of a material describes the behavior of free charges, as they are given in any conductor. The conductivity explains how strongly the current densitity in a tissue may be influenced by the strength of the electrical field $E$, i.e. the higher the conductivity of a material the stronger the current. Therefore, 2.6 is also called "Ohms law for linear conductors". There are tissues which have only dielectric or conductive properties. However, biological tissues have both free and fixed charges and hence both parameters are of relevance here [31].

It is important to know that the behavior of a linear material is not always isotropic, i.e. parameters may differ dependending on the direction of the current flow. It has for instance been shown that the conductivity of white matter in the brain is anisotropic [53].

### A closer look at the Maxwell equations

What do the Maxwell equations describe now? First of all they give a description of the electrical and magnetic sources in the tissue, which are represented by the behavior of the divergence of $D$ and $B$:

**Gauss's law** (2.1) states that the sources of the electrical fields can be described by the electrical charges of the tissue:

$$\nabla \cdot D = \rho$$

(For a proof see for example [30])

On the other hand, **Gauss's law for magnetism** states that magnetic fields are always solenoidal. This shows that there is no such thing like a single magnetic charge like in electrostatics: For magnetic fields we always need two different poles. This law can be followed easily from a variation of the law of Bio-Savart, which shows that $B$ can described as a curl field $B = \nabla \times A$, for a vector field $A$ [30]. It follows:

$$\nabla \cdot B = 0$$

as the divergence of a curl is always zero.

The two remaining equations describe the interactions between the electric and the magnetic field:

The **Maxwell-Faraday equation** is the differential form of *Faraday's law of induction*, which states that when a magnet (or a current circuit) is moved relative to another current circuit it induces a current in the latter. It was shown by Michael Faraday in 1931. The divergence form simply states that the temporal change of $B$ dictates the direction of E:

$$\nabla \times E = -\frac{\partial B}{\partial t}$$

Finally, the **Maxwell-Ampere equation** deals with induction into the other direction: It describes how a current carrying conductor induces a magnet field again (which is the principle of electromagnets). This equation is a further development of Ampere's circuital law, which states originally:

$$\nabla \times H = J$$

Consequently, direction and magnitude of the magnetic field are usually equal to direction and magnitude of the current density.

However, the Maxwell-Ampere equation includes a second term: the displacement current $\frac{\partial D}{\partial t}$. The reason for this can be seen if we take the divergence of $J$:

$$\nabla \cdot J = \nabla \cdot (\nabla \times H) = 0$$

This holds only in magnetostatics, where $J$ is solenoidal. In general $\nabla \cdot J$ has to be described by the continuity equation:

$$\nabla \cdot J = \frac{\partial \rho}{\partial t}$$

i.e. changes of electrical charges form the sources of the current density $J$. If we now have a look at Gauss' law again we see that $\frac{\partial \rho}{\partial t} = \nabla \cdot \frac{\partial D}{\partial t}$. Thus, $\frac{\partial D}{\partial t}$ is the term added by Maxwell, so the continuity equation holds again:

$$J = (\nabla \times H) + \frac{\partial D}{\partial t}$$

### 2.2.2. The quasi-static approach

One can already guess from the last paragraph that calculations with electromagnetic fields can become very complex. Hence, to develop a useful model it is neccessary to investigate under which conditions we can assume a less complex behavior.
Obviously much less complex cases are those of static fields, where we do not have interaction effects and can rather deal with the equations independently:
In electrostatics where we don't have temporary changes of $E$ and hence no induced magnetic field we receive:

$$\nabla \cdot D = \rho \tag{2.1}$$

$$\nabla \times E = 0 \tag{2.2a}$$

For similar reasons there is no time-varying field $D$ in the magnetostatic case and we get:

$$\nabla \cdot B = 0 \tag{2.3}$$

$$\nabla \times H = J \tag{2.4a}$$

So we see that in these cases the "'interaction-equations"' Maxwell-Faraday and Maxwell-Ampere are each reduced by one summand: The temporary change of B or D.

These equations yield two conclusions which do not hold in general electrodynamics: First of all, the Helmholtz decomposition (cf. [30]) tells us that a curl-free vector field is a gradient field. With 2.2a it follows:

$$E = -\nabla V \tag{2.8}$$

with $V$ being the well-known **electric potential**. Note that $V$ can indeed be defined with the help of the divergence free part of the electrical field $E$, which leads to the

important fact that $V$ is a quantity which is capable of describing differences rather than absolute values, since those are not well-defined (cf. 2.3).
Secondly, with 2.4a it is

$$\nabla \cdot J = \nabla \cdot (\nabla \times H) = 0 \tag{2.9}$$

like already mentioned in the last paragraph. (This means we again ignore the displacment current $\frac{\partial D}{\partial t}$ introduced by Maxwell.)

Equation 2.8 would highly simplify our work, since it is a scalar field. Furthermore, both equations give a good basis for a PDE: If we assume that the current density $J$ can be devided into a primary current $J^p$ (active current due to brain activity) and a volume current $J^s$ which can be described through the conductive term $J^s = \sigma E$, we get:

$$\boxed{0 = \nabla \cdot J = \nabla \cdot (J^p - \sigma \nabla V)} \tag{2.10}$$

This is Poisson's equation and a good approach for a model.
In reality, however, we often do not have a static current. This also holds for brain modelling since currents in the brain are not static (see Section 2.1.3), just as little as in tACS. So we assume now that we have a time harmonic current of a frequency $\omega$, which induces the time harmonic fields:

$$E = \tilde{E}e^{i\omega t} \text{ and } B = \tilde{B}e^{i\omega t}$$

Under which circumstances can we ignore the terms $\frac{\partial D}{\partial t}$ and $\frac{\partial B}{\partial t}$?

In the first case this is easy to answer. Obviously, the first term can be neglected if:

$$\left|\frac{\partial D}{\partial t}\right| \ll |J| = |\sigma E|$$

and since it is $D = \epsilon E$ it has to be:

$$\epsilon \omega E \ll \sigma E \Leftrightarrow \frac{\omega \epsilon}{\sigma} \ll 1$$

Hence, effects of bound charges (capacitive effects) represented by $\epsilon$ should be small compared to effects of free charges (conductive effects) which are represented by $\sigma$.

In the second case we have to investigate the contribution of the magnetic induction to the electrical field $E$. In [31] it was shown that we can neglect $\frac{\partial B}{\partial t}$ as soon as it holds:

$$\omega \mu \sigma R^2 \sqrt{1 + \frac{\omega^2 \epsilon^2}{\sigma^2}} \ll 1$$

Here $R$ is a characteristic wavelength in the human body, which can be estimated conservatively by a length of about $1m$ [31].

We now see that electromagnetic properties of living tissues play an important role in the applicability of the quasi-static approach. However, it is normally assumed that frequencies and properties in biomedical engineering legitimate its use. A dataset of typical properties of living tissues can for example be found in Schwan et al. 1957 [44]. Next to the explanation in [31], another detailed description of the quasi-static approach was for example given by Plonsey et al. in 1967 [36].

## 2.3. Additional information about tES and EEG

As an introduction to chapter 3, a few additional aspects of EEG and tES will be described now. With the main topic of the thesis being the comparison of CEM and PEM, this also includes a more vivid description of the CEM and the shunting effects, which are modelled in the CEM but not in the PEM. A mathematical description of both models will then be given in the main part. However, before we give an explanation of the shunting effects, we will start with a short general description of tES and EEG (2.3.1), followed by an overview about resistivity matrices and lead fields (2.3.2). This part shall also give an idea of how those matrices can be linked to each other (Principle of reciprocity ).

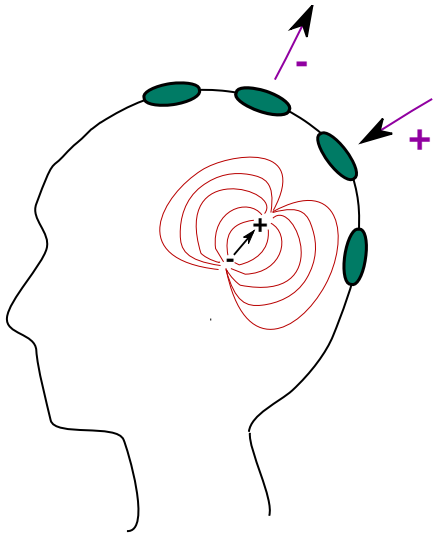


***Figure 2.6.:*** *General installation of tES and EEG: Measured potentials at applied electrodes (green) can either reflect induced currents (violet) or brain activity (red)*

### 2.3.1. General setting and zero potentials

We start this section with a general overview about the installation of tES and EEG: In both cases a fixed number of electrodes is attached to the head (cf. fig. 2.6). Each electrode can act in two different ways: we either apply a current to it or use it to measure potentials, which are evoked by currents from the brain (cf. section 2.1.3) or stimulation, respectively. The aim of this work is the simulation of EEG-measurements due to the tES. However, we will see in this section that this aim is closely linked to the normal EEG forward problem.

### Reference potentials in EEG

We have seen in the last section that an electrical potential as measured by the EEG can only describe the difference between two points, and hence one will always need a reference potential. Therefor one could e.g. create a virtual ground potential in the amplifier of the EEG and use this to create a ground electrode on the subjects body. However, if one would use this electrode as a reference, measurements would be greatly influenced by noise in the measurements device [22]. To solve this problem EEG systems use differential amplifiers: Measurements are done in comparison to a ground potential, but in the following one or more EEG-electrodes are chosen as a virtual reference to get rid of the ground potential again (i.e. the reference is used as the new ground potential) [22]. There are a few different prevalent choices for the ground potential: It is very common to place a reference electrode on earlobe or mastoid and use this as a reference. Normally one will use both sides as a reference here, since patterns would be unsymmetrically otherwise. It is also common to use the average potential of all electrodes as a reference, what will be our assumption in later chapters.
In practical EEG reference installations can influence the outcome of the experiment, since different installations lead to different patterns of potential measurements. However, this is not relevant in this work, but rather for interpretation of real measurements, when more complex potential patterns are investigated (for example the change of patterns over time). Reference installations have of course no impact on the calculation of currents on the other hand, since these do not depend on the choice of potential. For further information on this topic see e.g. [22] (p.105 ff.).

## 2.3.2. Lead field and resitivity matrices

It is the main focus of this work to investigate the relationship between a current pattern $I_l$ applied to several of the electrodes on the head and the EEG potentials $U_l$ measured due to this applied current in use of different models. Therefore, we search for a matrix $L_{tES}$, for which holds:

$$L_{tES} I = U$$

at which $I = (I_l)_l$ and $U = (U_l)_l$. In EIT such a matrix is called a **resistivity matrix** (cf. [46]) and we will later see that the connection between $I$ and $U$ is indeed linear. We will furthermore have the opportunity to investigate the behavior of resulting currents in the head. Hence, we will also search for a matrix $L_{tES2}$ with

$$L_{tES2} I = u$$

and $u$ describing the potential in the head.

In contrast to the tES problem described above, in usual EEG forward modeling one investigates EEG potentials induced by brain activity which is represented by the primary current density $J^p$. An equivalent matrix to the matrices described above is hence

a matrix $L_{EEG}$ with:

$$L_{EEG}J^p = U$$

This matrix is called the **lead field matrix** and is of great relevance in EEG, since once it is known, potential distributions of the EEG can be calculated for each possible current density $J^p$ in an effective way.
This work is essentially based on a computer code which was originally written for the calculation of lead field matrices. Therefore, an insight into lead field matrices and the connection between $L_{EEG}$ and the tES forward problem will also be given. However, we will start with the concept of current dipoles, which delivers a proper way to describe the current density in the head:

### Current dipoles

In EEG forward modeling as well as in inverse modeling one normally treats current sources in form of dipoles, instead of volume sources. It has been shown that dipoles can represent volume sources sufficiently well, and they are much easier to construct and dealt with than volume sources are [27].
One distinguishes between two different kinds of dipoles. The first one can be imagined as the description of a current sink and a current source, separated by a distance $h$. Sink and source are both of the same strength $I$ ,and the current source has a certain direction, namely the orientation from source to sink. The dipole moment can then be defined as $hI$. On the basis of this description, one can now define the mathematical dipole (or real dipole). Therefor we assume that $h \longrightarrow 0$. To keep the dipole moment finite, $I$ is increased analogously to $h$, i.e.: $I \longrightarrow \infty$. We can then describe such a dipole at a fixed position as the vector:

$$d = hIe_d = qe_d$$

where $e_d$ is a unit vector describing the direction of the dipole [27]. One can now describe $J^p$ as a vector of dipole moments, belonging to a fixed number of dipole direction vectors. If we assume that the connection between $U$ and $d$ is linear (linearity asumption), $L_{EEG}$ can be calculated for one constellation of dipoles moment vectors (normally unit vectors) and applied to every other set of dipoles. This will be described in the following:

### Linearity assumption

The descriptions in the next three paragraphs follow mainly [52]. We want to calculate the potential $U_l$ at an electrode $e_l$ caused by a single dipole $d$. We can describe $d$ as a linear combination of unit vectors $i_1$, $i_2$, $i_3$, localized at the same position as $d$:

$$d = q_1i_1 + q_2i_2 + q_3i_3$$

Normally $i_1$, $i_2$ and $i_3$ are assumed to be those vectors which are orientated parallel to the x-, y- and z-axis. However, they could of course also describe another set of

linearly independent vectors (cf. 4.1.2). The linearity assumption [52] now states that $U_l$ depends on $d$ in a linear way, e.g.:

$$U_l(d) = q_1 U_l(i_1) + q_2 U_l(i_2) + q_3 U_l(i_3) = \langle q, I_l \rangle$$

Thereby it holds $I_l = (U_l(i_j))_j$ and $q = (q_i)_{1 \leq i \leq 3}$. Hence, we can calculate $U_l(d)$ for every $d$ if $I_l$ is known. This principle can be expanded to the whole current density field $J^p$, described by a set of dipoles $(d_k)_{1 \leq k \leq K}$. If we define $\widetilde{q} = (q_i^k)_k$ as the representation vector of $J^p$, we can find an equivalent description as explained above for the whole vector field:

$$U_l = \langle \widetilde{I}_l, \widetilde{q} \rangle$$

with $\widetilde{I}_l = (I_{l_k})_k$.

### Description of $L_{EEG}$

With the above representation we can find a closer description of the matrix $L_{EEG}$. If $\langle \widetilde{I}_l, \widetilde{q} \rangle = U_l$, we can replace the vector $U = (U_l)_l$ by:

$$\begin{pmatrix} \widetilde{I}_1^{\,T} \\ \vdots \\ \widetilde{I}_L^{\,T} \end{pmatrix} \widetilde{q} = \begin{pmatrix} U_1 \\ \vdots \\ U_L \end{pmatrix}$$

Then the matrix $(\widetilde{I}_l)_l^T$ is exactly the matrix $L_{EEG}$.

### Leads and lead fields

We assume now that we have a single electrode $e_r$ which serves as a reference electrode. In this case, the vector $(U_l)_l$ can be described as a vector of length $(L-1)$ instead of $L$ and every entry can be represented by the term $\widehat{U}_l = U_l - U_r$. Like indicated above, we can find a vector $I_{l,r}$ with:

$$I_{l,r}^T q^k = \widetilde{I_{l,r}}^{\,T} \widetilde{q} = U_l - U_r$$

Thus, we can get a more vivid idea of $\widetilde{I_{l,r}}$: It is a measurement for the voltage between the two electrodes as it is caused by a set of dipoles $q^k$. We call $I_{l,r}$ a *lead vector* as it describes the voltage generated by a dipole at a fixed position for a given *lead*, which is the denotation for a pair of electrodes in biomedical engineering. $(\widetilde{I_{l,r}})$ is then referred to as the lead field, because it describes a vector set of lead field vectors, all belonging to $(U_l, U_r)$. We can again generalize this concept for all $\hat{U}_l$ and receive:

$$L_{EEG}\widetilde{q} = (\widetilde{I_{l,r}})_l^T \widetilde{q} = (\widehat{U}_l)_l$$

Hence, $L_{EEG} = (\widetilde{I_{l,r}})_l^T$ is a matrix consisting of different lead fields if we choose the embodiment $\hat{U}$ for the potentials at the electrodes.

It is common to describe $L_{EEG}$ in this way instead of the way described above. First of all, this has the advantage that the reference potential is already well defined, which leads to a well defined solution of the investigated equation system. We will see later that solutions of such systems are indeed unique except for a constant. Defining $L_{EEG}$ as a $\mathbb{R}^{K\times(L-1)}$ matrix leads to a unique solution, i.e. the problem is elliptic now.
The other advantage of the lead field description is that it delivers a direct link between the tES and the EEG forward problem:

### Reciprocity approach

Indeed, the lead field approach in EEG leads to a similar situation as in the tES stimulation. In both cases a given lead is investigated regarding its connection to electrical fields in the head. However, position of source and generated voltages is interchanged: In tES we apply a current to the lead and ask for its influence on the brain, in the EEG lead field approach we search for voltages at the lead, which are evoked by currents in the head.
To understand the relationship of both situations one can now make use of the so-called reciprocity principle, which is e.g. described in [27]: It traces back to Helmholtz in 1853 and describes essentially the fact that the voltage induced to a measurement device by a volume source $d$ in a conductor is exactly the same as the voltage induced to the volume source would be, if the measurement device was a current source of the same strength. In a more exact form it states the following: For a physical dipole located at the points $p_{sink}$ and $p_{source}$ and two sources $p_{in}$ and $p_{out}$ at the surface of the head (e.g. electrodes) it holds:

$$I_H(U_O(p_{source}) - U_O(p_{sink})) = I_O(U_H(p_{in}) - U_H(p_{out})) \tag{2.11}$$

Here $I_H$ and $I_O$ are the current strengths of the volume source or at the surface sources, respectively. Correspondingly, $U_H$ is the potential difference at the electrodes evoked by $I_H$, and $U_O$ describes the voltage at the source evoked by $I_O$. The ratio of the voltage differences is now equal to the ratio of current densities, i.e. if $I_O = I_H$ voltage differences are the same.
In order to show the practical consequences of these observations, let us first state that the physical dipole can be described as a mathematical dipole again ($h \longrightarrow 0, I_H \longrightarrow \infty$) and it is:

$$\begin{aligned} I_H(U_O(p_{source}) - U_O(p_{sink})) &= I_H((U_O(p_{sink}) + \nabla U_O(p_{source})h + O(\nabla^2)) - U_O(p_{sink})) \\ &\approx I_H h \nabla U_O(p_{source}) \longrightarrow q\nabla U_O(p_{source}) \end{aligned}$$

If we now assume a unit current flowing from $p_{in}$ to $p_{out}$ ($I_O = 1$) at the surface of the head, 2.11 delivers:

$$q\nabla U_O(p_{source}) = U_H(p_{in}) - U_H(p_{out})$$

Since $U_H$ is evoked by the source, we can write the right hand side with a lead vector again. It follows:

$$U_H(p_{in}) - U_H(p_{out}) = \langle I_{in,out}, q\rangle = \langle \nabla U_O(p_{source}), q\rangle$$

This means that the gradient of the potential evoked by the applied current to the electrodes describes exactly the lead vector for each volume source.

In other words: Calculation of $EEG$ and $tES$ is closely tied to each other and $L_{EEG}$ can even be followed from calculations of $L_{tES2}$. However, this requires to write $L_{EEG}$ in the proper form and to calculate the lead fields for all involved EEG electrodes. In this work the tES will only be calculated for one pair of electrodes. Moreover, we will see that $L_{EEG}$ was not computed in a classical lead field form in the original code, hence the reciprocity theorem was not used here. Therefore, the last two paragraphs shall only give a short idea of this important approach. A much deeper insight into this topic can be found in [27], [52] or [34].

### 2.3.3. Whats the idea of the complete electrode model (Shunting effects)?

The complete electrode model is an alternative model to the current standard model in EEG. Standard models normally assume that electrodes are neutral elements on the surface on the head, i.e. are just identified with a point on the head where the potential is measured.

The idea of the CEM was originally described for the EIT. In EIT one aims to find out resistivities of conductors. Therefore, a current is applied through a number of electrodes placed around the conductor and the resulting voltage is measured at the applied electrodes. One then aims to recalculate the resitivities based on those measurements [4].
In 1989 Cheng et al. [4] measured the relative resistance of electrodes for different spatial frequencies of currents applied to a homogenous bath (fig. 2.7a). The relative resistance

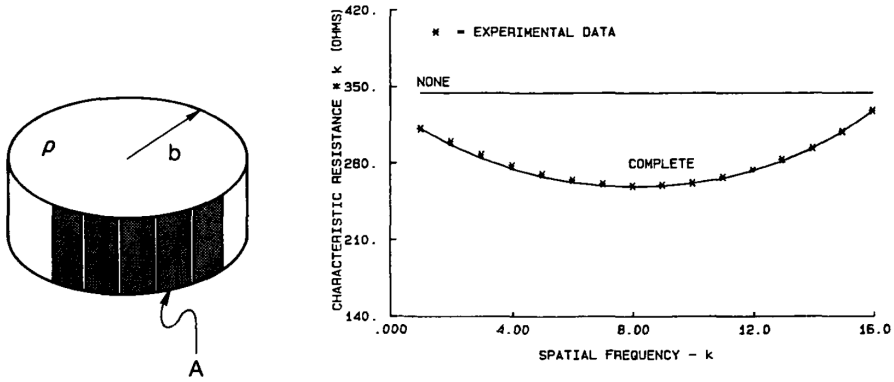


*(a) Installation of the experiment* *(b) Illustration of results and model approaches*

***Figure 2.7.:*** *Experiment of Cheng et al. [4]*

at each electrode is here defined as the ratio between voltage and current, restricted to the electrode, i.e: $r_l = V_l/JA_l$. If $J$ is a spatial sine or cosine wave of a frequency $k$, i.e $J$ is continuous on the surface of the object in particular, $J$ is supposed to be proportional to $k$ [4, 10] and hence it should be:

$$r_l \sim \frac{1}{k}$$

for every frequency $k$. However, the experiment showed that this is not the case. Fig 2.7b presents the results of the experiment, at which the asterisks represent the characteristic resistances calculated from the data multiplied with the frequency $k$. If the equation described above would hold, the data should follow the horizontal line, but the data shows that resistances do not develop as aspected. Cheng et al. argued that this is because the current distribution is not continuous on the surface, as aspected in the theoretical approach, but rather discretized by the applied electrodes[4]. Moreover, they pointed out two effects at the electrodes, which influence the current flow:

- since electrodes are highly conducting parts of the currents, **parts of the current will shunt** through the electrode instead of the bath
- there is an **effective contact impedance (ECI)** between electrode and the object, which is mainly influenced by the electrolyte applied to the electrode

The complete model is an approach to incorporate those effects. The lower line in figure 2.7b shows the calculation of the complete electrode model, where the parameters are calculated from the measurements [4, 46]. Obviously the model reflects the experimental results very well.

What is the effect of the model in context of EEG and tES calculations now? To answer this question we start with the assumption, that the effective contact impedance (ECI), described above is very low. Figure 2.8a shows the effect of such an installation. A low ECI represents a very good contact between skin and electrode. If this is the case, the shunting currents can flow freely through the electrodes and into the skin. Since electrodes are a much better conductor than the skin, currents will distribute equally through and - due to the good contact - under the electrode: potentials will become constant here. This can obviously influence current patterns on the skin. Due to the effects underneath the electrode, it is also obvious that **form and size of the electrodes** will have an influence on the computation results. This is not the case in the PEM, which has two reasons: Firstly, the PEM assumes the electrode to be pointwise. Secondly, even if this assumption was not made, in the standard model the EEG electrodes do not have an influence on current distribution[5]. Hence, their size does not matter.
Shunting effects will be influenced by the contact impedance in the opposite way: If the ECI increases, shunting effects will decrease, because the exchange between electrode

[4] In the experiments the bath was surrounded by electrodes, which were assumed to lead a continuous current trough the bath. However, small gaps prohibit such a continuous distribution, leading to current effects at the edges of the electrodes -cf. [4]

[5] cf. section 3.1.2, where the infinite case is described

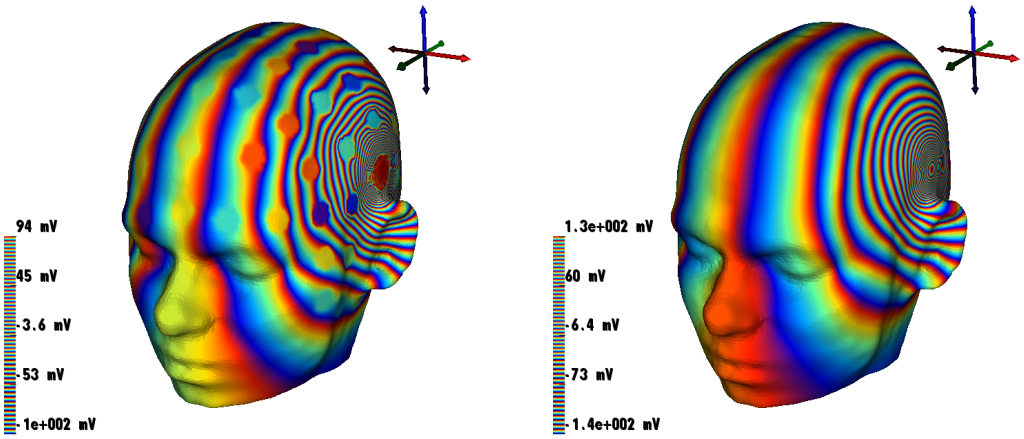


*(a) CEM for low ECIs ($Z_l = 1\,\Omega \cdot |e_l|$)* *(b) Standard model*

***Figure 2.8.:*** *Comparison of potential distributions in combined EEG and tES simulations, using different models*

and skin will get worse. Therefore, the PEM can be seen as a limit case of the CEM, with the ECI raised to infinity (cf. 3.1.2).

# 3. Modelling PEM and CEM in tES and EEG

## 3.1. Finding a model

We now want to find an appropriate model for tES and EEG. The first section aims to elaborate the basic equations for both models. Thereby the next paragraphs are mainly based on [39], [51], [46] and [33].

### 3.1.1. The model in general

To find an appropriate model let $\Omega$ be the head and $(e_l)_l$ $L$ electrodes on its surface $\partial\Omega$ with size $|e_l|$, potential $U_l$ and impedance $Z_l$. The current applied to each of the electrodes is described by $I_l$. Normally it will be $I_l \neq 0$ for only a few electrodes (or none in EEG). Additionally, we assume:

$$\sum_{i=1}^{L} I_l = 0 \tag{3.1}$$

From the described quasi-static approach in chapter 2.2.2 we have already received equation 2.10 as a description of the potential $u$:

$$0 = \nabla \cdot J = \nabla \cdot (J^p - \sigma \nabla u) \tag{2.10}$$

This holds because

$$0 = \nabla \cdot (\nabla \times H) \approx \nabla \cdot J \quad \text{and} \quad J - J^p = J^s = \sigma E \approx \sigma \nabla u$$

$J^s$ represents the passive current in the head, whereas $J^p$ is the primary current of the head, i.e. the current sources inside of the head.
In tES the stimulating electrodes on the boundary $\partial\Omega$ are the only relevant current sources. Hence it is $J^p = 0$ and we receive:

$$\nabla \cdot (\sigma \nabla u) = 0 \tag{3.2}$$

for a pure tES simulation. However, EEG and tES can both be described with Poisson's equation.

We have to take into account that $u$ will be rarely continuous, since $\Omega$ consists of different structures with different behavior, i.e. different conductivities. Therefore, we assume $J \in H^1(\Omega)$ and $u \in H^1(\Omega)$ instead and search for the weak solution $u$ which fullfills:

$$\int_\Omega \nabla \cdot (\nabla u(x))\varphi(x)dx = \int_\Omega J^p(x)\varphi(x)dx \quad \forall \varphi \in H^1(\Omega)$$

(The right hand side becomes zero in tES, of course).

To find a unique solution for Poisson's equation, we need additional boundary conditions, which are often given by a function $g \in H^1(\partial\Omega)$ and functions $\alpha, \beta \in H^1(\partial\Omega)$ [8]:

$$\alpha(x)u + \beta(x)\frac{\partial u}{\partial n}(x) = g(x) \quad \forall x \in \partial\Omega \tag{3.3}$$

Again, equation 3.3 only needs to be fulfilled in the weak sense. Hence it should be:
$\left(\alpha u + \beta\frac{\partial u}{\partial n} - g_D\right) \in H_0^1(\Omega)$ for a function $g_D \in H_1(\Omega)$ with $g_{D|\partial\Omega} = g$
Furthermore, there are sometimes additional conditions for the function $g$, i.e. for Robin boundary conditions (cf. 3.1.2). The boundary conditions are very important here, since these are the equations which are actually different for both models. Hence in the next paragraph these boundary conditions will lay the basis for the comparison.

However, another problem persists in this situation. It was already described in section 2.3 that the potential $u$ cannot be described in a fixed scala. $u$ can only describe the difference between two points. Hence we need a reference potential to prohibit infinite possible solutions. Here the zero reference potential is defined as:

$$u_0 = \sum_{I=1}^{L} U_l \coloneqq 0 \tag{3.4}$$

So the zero potential here is the mean of the potentials of the electrodes, a common installation in EEG.
We will look at the necessity of $u_0$ for both electrode models (FEM and PEM) separately in the next section and proof in 3.2 that the described conditions 2.10 (or 3.2), 3.3 and 3.4 guarantee a unique solution $u \in H^1(\Omega)$ in the weak sense.

## 3.1.2. Boundary conditions: Distinguishing CEM and PEM

### Point electrode model (PEM)

We start with the standard point electrode model. In this case equation 3.3 is replaced by:

$$\sigma\frac{\partial u}{\partial n}(x) = 0 \qquad \forall\, x \in \partial\Omega \backslash \cup_{s=1}^{S} e_s \tag{3.5}$$

$$\sigma\frac{\partial u}{\partial n}(x)_{|e_s} = j_s = \frac{I_s}{|e_s|} \qquad \forall\, 1 \leq s \leq S \tag{3.6}$$

The electrodes $e_1 \dots e_S$ represent the stimulating electrodes on the head.
Since $\sigma \frac{\partial u}{\partial n}(x)$ equals the current flowing over the the surface of the head, the *current flux*, equation 3.5 simply states that there's no current expected to flow out of the head, except for the current due to the stimulating electrodes.
These have to be treated in a special way: Since those electrodes are much bigger than the other electrodes it makes no sence to ignore their form and size. Hence another model is used for the stimulating electrodes here: It simply assumes a constant current density $J_s = \frac{I_s}{|e_s|}$ over the whole electrode. This is called the gap model [51]. It is similar to the current standard model in tES forward simulation. However, it is even a simpler version. In fact current standard models for tES stimulation are a combination of CEM and gap model: They assume a constant current density over the whole electrode but combine this model with a "'sponge"' underneath the electrode. This "'sponge"' symbolizes the saline gel underneath the electrode and is assumed to have a conductivity which is much higher then the surrounding tissue. This way the "'sponge model"' allows effects which are similar to the shunting currents in the CEM. Therefore, it can be assumed that the standard model for the stimulating electrodes will lead to results which lie between the results of CEM and the gap model. To reproduce standard models as good as possible we will later use both options for the simulation at the stimulating electrodes and combine them with the PEM at the normal EEG electrodes.

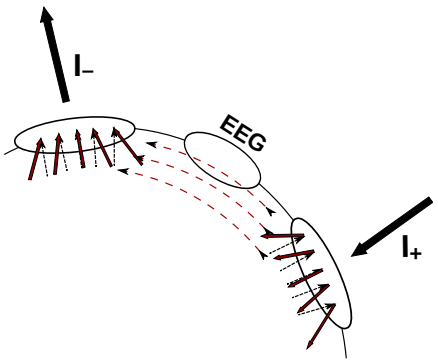


***Figure 3.1.:*** *In the PEM the current density $J$ is constant in normal direction. Since no current flux is allowed on normal EEG electrodes, those electrodes do not influence the behavior of $J$.*

Additionally, a description of the constant electrode potential $U_l$ is needed. Since the PEM does not take impedances of electrodes into account, $U_l$ is simply assumed to be the mean of the potential underneath the electrode:

$$U_l = \frac{\int_{e_l} u \, \mathrm{d}S}{|e_l|} \tag{3.7}$$

Since $|e_l| \longrightarrow 0$ for the "'normal"' measurement electrodes, 3.7 becomes:

$$U_l = u(p_l) \tag{3.8}$$

in this case. Here $p_l$ is the position of the electrode.

Equations 3.5 and 3.6 represent a Neumann boundary condition ($\alpha = 0$ in 3.3). One can see easily why the zero reference potential is needed here:
We assume $\tilde{u}$ is a solution of the boundary conditions and equation 2.10. Then all equations hold as well for every solution $\tilde{u} + c$, if $c$ is constant. However, with equations

3.4 and 3.7 we receive:

$$0 = \sum_l \frac{\int_{e_l} \tilde{u} + c\, dS}{|e_l|} = \sum_l \frac{\int_{e_l} \tilde{u} dS}{|e_l|} + Lc$$

Hence $u = \tilde{u} + \tilde{c}$ with

$$\tilde{c} = -\frac{1}{L} \sum_l \frac{\int_{e_l} \tilde{u} dS}{|e_l|}$$

is a more restricted solution of the model.
In section 3.2 it will be proofed that such a solution is existent and unique.

### Complete electrode model (CEM)

In contrast to the point electrode model the boundary conditions for the CEM represent a mixed type of boundary conditions:

$$\sigma \frac{\partial u}{\partial n}(x) = 0 \qquad \forall\, x \in \partial\Omega \setminus \cup_{l=1}^{L} e_l \tag{3.9}$$

$$\int_{e_l} \sigma \frac{\partial u}{\partial n}(x) dS = I_l \qquad \forall\, 1 \leq l \leq L \tag{3.10}$$

$$u(x) + Z_l \sigma \frac{\partial u}{\partial n}(x) = U_l \qquad \forall\, 1 \leq l \leq L \tag{3.11}$$

For the surface of the head which isn't covered by electrodes, the model shows the same behavior like the PEM, i.e. we receive a Neumann condition describing that no current may flow out of or into the head (3.9).
3.11 is a Robin boundary condition ($\alpha$ and $\beta \neq 0$ in 3.3). Equation 3.10 gives additional information about the current flux $\sigma \nabla u \cdot n$ and especially about the relationship between the induced current and the behavior of $u$.

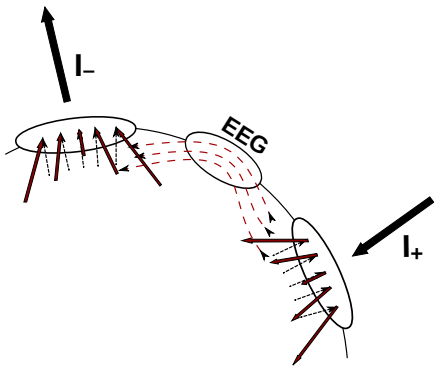


***Figure 3.2.:*** *In the CEM the current density $J$ is allowed to change intensity and direction over the surface of the electrodes.*

Equation 3.10 provides the most interesting information here, since this is the equation allowing the shunting currents to take place.
The PEM model doesn't allow currents to flow freely out of or into the head at the measurement electrodes and even the gap model (i.e. the above model for the stimulating electrodes) allows only a very restricted flux, stating that this flux has to be constant over the whole electrode.
In the CEM, on the other hand, the current flux is allowed to diversify over the electrode. Particularly it is allowed to take place at the measurement electrodes at all. The only

restriction here is that the current flux over the whole electrode is equal to the applied current $I_l$ (which is zero at most of the electrodes). Hence the current can leave the head if it flows back at another point underneath the electrode (see figure 3.2).
Now equation 3.11 describes the connection between the electrode potential $U_l$ and the potential $u$ underneath the electrode. Since the contact impedance is taken into account here, there is a difference term $Z_l\sigma\nabla u \cdot n$ which is proportional to the current flux. This is not surprising, since the current flux gets stronger if the potential difference increases. On the other hand, the difference also increases if the effective contact impedance $Z_l$ (ECI) does. This explains why the potential underneath the electrode gets almost constant for a low ECI: If $Z_l$ vanishes, the difference term vanishes, too, and it is $u \approx U_l$. Because $U_l$ is a constant $u$ becomes constant as well.

It is important to point out that the ECI does not describe a normal impedance, but illustrates the behavior of the actual impedance on the electrode as an abstract parameter defined on every point of the electrode surface [4]. The actual impedance can be identified with the average contact impedance (ACI) over the whole electrode, stating [39]:

$$ACI = \overline{U}I = \frac{\int_{e_l} |U_l - u| \, \mathrm{d}S}{|e_l|} \int_{e_l} |\sigma\nabla u \cdot n| \, \mathrm{d}S = \frac{\int_{e_l} Z_l |\sigma\nabla u \cdot n| \, \mathrm{d}S}{|e_l|} \int_{e_l} |\sigma\nabla u \cdot n| \, \mathrm{d}S$$

The ECI can vary over the surface of the whole electrode [4]. However, we will assume that the ECI is constant over the whole surface. Under these circumstances it holds:

$$Z_l = ACI \cdot |e_l|$$

This approach was also used for the calculations, as the ACI over the whole electrode can be measured easily, while we have no information about the actual ECI here.

Similarly to the PEM case, a possible solution $\tilde{u}$ of the equations above would deliver an infinite number of possible solutions $\tilde{u}+c$, which would also fulfill all necessary equations, if $U_l$ could be freely chosen. Hence equation 3.4 is necessary here, too, and we have to prove the uniqueness and existance of a weak solution for all described conditions (3.2).

### From CEM to PEM in EEG

Although the details of both models seem to be quite different at the first view, it can be pointed out that the PEM is in fact only a special case of the CEM, namely the limit case of the CEM, with $Z_l \longrightarrow \infty$ and $|e_l| \longrightarrow 0$. This holds at least for the non-stimulating electrodes, whereas it can't be easily applied to an electrode with an injected current.

To point this out we have a look at a variation of 3.11 again:

$$\sigma\nabla u \cdot n = \frac{1}{Z_l}(U_l - u)$$

Therefore it holds:

$$\lim_{Z_l \longrightarrow \infty} \sigma\nabla u \cdot n = 0 \tag{3.12}$$

This is exactly the proposition of equation 3.5 for all pure EEG measurement electrodes, which states that the current flux is zero on all of these electrodes.
On the other hand equation 3.12 also shows why this approach is problematic for a stimulating electrode: Obviously we want a current flux to be allowed in case of a stimulation, otherwise the stimulation can't take place. Hence this equivalence holds only for the other electrodes.
In fact, taking the limit of $Z_l$ makes up the main part to get the PEM again: Since there is no current flux allowed through the electrodes anymore, the electrodes have a neutral position in the behavior of the head potential, just as they have in the PEM and the distribution of the head potential will be the same in both situations.
However, the electrodes aren't pointwise yet. Integrating over equation 3.11 and replacing with 3.10 delivers:

$$\int_{e_l} U_l \,\mathrm{d}S = \int_{el} u + \sigma \nabla u \cdot n \, dS = \int_{el} u \,\mathrm{d}S + I_l = \int_{el} u \,\mathrm{d}S$$

This holds since $I_l = 0$ for normal EEG electrodes. Hence it is:

$$U_l = \frac{\int_{e_l} u \,\mathrm{d}S}{|e_l|}$$

which describes the Gap model! (3.6 holds anyway, since $I_l = 0$.) Therefore, to get to the PEM, the size of the electrodes has to be shrinked to zero again:

$$\lim_{|e_l| \longrightarrow 0} U_l = \lim_{|e_l| \longrightarrow 0} \frac{\int_{e_l} u \,\mathrm{d}S}{|e_l|} = u\left(p_l\right) \tag{3.13}$$

## 3.2. Weak formulations

The following section will describe weak formulations of the model. It will lay the foundation for the FEM approach in section 4.1. Moreover it will be proofed that there is always a unique solution for every approach described above.

### 3.2.1. Weak form of the PEM

To get a weak solution of the PEM in $H^1(\Omega)$ we multiply 2.10 with a test function $\varphi \in H^1(\Omega)$ and integrate over $\Omega$:

$$\begin{aligned}
\int_\Omega \left(\nabla \cdot J^p\right) \varphi \,\mathrm{d}V &= \int_\Omega \nabla \cdot (\sigma \nabla u) \, \varphi \,\mathrm{d}V \\
&= \int_\Omega \nabla u \cdot \nabla \varphi \,\mathrm{d}V + \sum_{i=1}^{L} \int_{e_l} (\sigma \nabla u \cdot n) \, \varphi \,\mathrm{d}S \\
&= \int_\Omega \nabla u \cdot \nabla \varphi \,\mathrm{d}V + \sum_{i=1}^{L} \frac{I_l}{|e_l|} \int_{e_l} \varphi \,\mathrm{d}S \quad \forall \varphi \in H^1\left(\Omega\right)
\end{aligned}$$

where Gauss's divergence theorem and 3.5 is used in the first step and the boundary condition 3.6 in the second. Note that 3.6 is assumed to hold for all electrodes here. This is allowed since $I_l = 0$, if $e_l$ is a pure EEG electrode. Therefore both approaches lead to the same equation.
The weak form of the PEM doesn't include information about $U_l$ now and indeed we will see that $u$ is calculated independently from $U_l$ (except for the zero potential correction). Therefore, one has to add the additional information about $u$. With 3.7 the complete equation system is:

$$\forall \varphi \in H^1(\Omega): \int_\omega \nabla u \cdot \nabla \varphi \, \mathrm{d}V + \sum_{i=1}^{L} \frac{I_l}{|e_l|} \int_{e_l} \varphi \, \mathrm{d}S = \int_\Omega (\nabla \cdot J^p)\, \varphi \, \mathrm{d}V \tag{3.14}$$

$$\text{If } I_L \neq 0: \int_{e_l} u \, \mathrm{d}S - |e_l| \cdot U_l = 0, \quad u(p_l) = U_l \quad \text{otherwise} \tag{3.15}$$

If we have a closer look at equation 3.1, we will see that there is one necessary condition for the existence of a solution. It has to be:

$$\sum_{i=1}^{L} I_l = \int_\Omega (\nabla \cdot J^p) \, \mathrm{d}V \tag{3.16}$$

This follows for $\varphi \equiv 1$ and is the same condition every Neumann problem has to fulfill (cf. e.g.[3]).
Because of the assumption 3.1 both sides have to be zero. This implies that the sum of the sources in $\Omega$ vanishes (right hand side), i.e. the head is no current source itself. It also states all applied currents pass the head (left hand side). While making sense, this conclusion is in fact a simplification. For example, in a pure EEG a very small current will pass the electrodes to reach the measurement device. Otherwise the potentials couldn't be measured [33]. Hence assuming both sides as zero might be a little inaccurate, but is a tolerable assumption, since the currents in the brain are much smaller than the applied currents $I_l$ and this holds even more for those currents leaving the brain.
In the strict sense 3.16 only states that the sum of $I_l$ is equal to the current leaving the head. (Note that $I_l$ as described in equation 3.5 in fact refers to the current in normal direction, i.e. describes the current *leaving* the head, for example it is $-1mA$ at the anode and $1mA$ at the cathode)

### 3.2.2. Weak form of the CEM

For the weak form of the CEM we start just as in the last paragraph and receive with Gauss's divergence theorem, equation 3.9 and finally 3.11:

$$\begin{aligned}\int_\Omega (\nabla \cdot J^p)\,\varphi \,\mathrm{d}V &= \int_\Omega (\sigma\nabla\cdot\nabla u)\,\varphi\,\mathrm{d}V \\ &= \sum_{l=1}^{L}\int_{e_l}(\sigma\nabla u\cdot n)\,\varphi\,\mathrm{d}S - \int_\Omega \nabla u\cdot\nabla\varphi\,\mathrm{d}V \\ &= \sum_{l=1}^{L}\int_{e_l}\frac{1}{Z_l}(U_l-u)\,\varphi\,\mathrm{d}S - \int_\Omega \nabla u\cdot\nabla\varphi\,\mathrm{d}V\end{aligned}$$

On the other hand rearranging 3.10 and 3.11 delivers:

$$Z_l I_l = \int_{e_l} Z_l\sigma\nabla u\cdot n\,\mathrm{d}S = \int_{e_l}(U_l-u)\;\mathrm{d}S$$

Hence we receive the equation system:

$$\forall\varphi\in H^1(\Omega): \sum_{l=1}^{L}\int_{e_l}\frac{1}{Z_l}(U_l-u)\,\varphi\,\mathrm{d}S - \int_\Omega\nabla u\cdot\nabla\varphi\,\mathrm{d}V = \int_\Omega(\nabla\cdot J^p)\,\varphi\,\mathrm{d}V \tag{3.17}$$

$$\forall\, 1\le l\le L: \qquad \frac{1}{Z_l}\int_{e_l}(U_l-u)\;\mathrm{d}S = I_l \tag{3.18}$$

In this situation the equations in the system obviously aren't solvable independently, like they were for the PEM: The relevant information about the stimulation (applied current $I_l$) is described in the additional equation 3.18, whereas the behavior of $u$ in $\Omega$ is described in 3.17. Furthermore, equation 3.17 contains information about the electrode potential $U_l$.
Additionally, no bilinear form can be found in 3.17, like it was the case in the PEM. Since such a form is needed to proof the existence of the solution here, an alternative version of system (3.17, 3.18) will be introduced:

Let $\Phi = (\Phi_l)_l \in \mathbb{R}^L$ be arbitrary. Then it holds:

$$\begin{aligned}&\sum_{l=1}^{L}\int_{e_l}\frac{1}{Z_l}(U_l-u)(\Phi_l-\varphi)\;\mathrm{d}S + \int_\Omega\nabla u\cdot\nabla\varphi\,\mathrm{d}V \\ =&\sum_{l=1}^{L}\underbrace{\int_{e_l}\frac{1}{Z_l}(U_l-u)\,\Phi_l\,\mathrm{d}S}_{\Phi_l\cdot(3.18)} - \underbrace{\left(\sum_{l=1}^{L}\int_{e_l}\frac{1}{Z_l}(U_l-u)\,\varphi\,\mathrm{d}S - \int_\Omega\nabla u\cdot\nabla\varphi\,\mathrm{d}V\right)}_{(3.17)} \\ =&\sum_{l=1}^{L} I_l\Phi_l - \int_\Omega(\nabla\cdot J^p)\,\varphi\,\mathrm{d}V\end{aligned} \tag{3.19}$$

The left side now is a bilinear form on $H^1(\Omega) \times \mathbb{R}^L$ and equation 3.19 is equivalent to the system above, if it is fulfilled for all $(\varphi, \Phi) \in H^1(\Omega) \times \mathbb{R}^L$.
Furthermore, setting $\varphi \equiv 1$ and $\Phi_l \equiv 1$ in 3.19 leads to equation 3.16 again. Hence the CEM has to fulfill the same conditions as the PEM.

### 3.2.3. Existence and uniqueness of solutions

One can proof that there exists a unique solution for each of the described problems. The next theorem summarizes the expectations so far. A proof is given in appendix A.

**Proposition 3.1 (*Existence of solutions*)**

*Let* $\beta_P : H^1(\Omega) \times H^1(\Omega) \longrightarrow \mathbb{R}$ *and* $\beta_C : \left(H^1(\Omega) \times \mathbb{R}^L\right) \times \left(H^1(\Omega) \times \mathbb{R}^L\right) \longrightarrow \mathbb{R}$ *be defined as follows:*

$$\beta_P(u, \varphi) \coloneqq \int_\omega \nabla u \cdot \nabla \varphi \, \mathrm{d}V,$$
$$\beta_C(u, U, \varphi, \Phi) \coloneqq \sum_{l=1}^{L} \int_{e_l} \frac{1}{Z_l} (U_l - u)(\Phi_l - \varphi) \, \mathrm{d}S + \int_\Omega \nabla u \cdot \nabla \varphi \, \mathrm{d}V$$

*Thereby* $U = (U_l)_l$, $\Phi = (\Phi_l)_l \in \mathbb{R}^L$ *and* $e_l \subset \partial\Omega$ *for all* $0 \leq l \leq L$.
*Furthermore, the linear forms* $f_P : H^1(\Omega) \longrightarrow \mathbb{R}$ *and* $f_C : H^1(\Omega) \times \mathbb{R}^L \longrightarrow \mathbb{R}$ *shall be given by:*

$$f_P(\varphi) \coloneqq \int_\Omega \nabla \cdot J^p \varphi \, \mathrm{d}V - \sum_{l=1}^{L} \frac{I_l}{|e_l|} \int_{e_l} \varphi \, \mathrm{d}S$$
$$f_C(\varphi, \Phi) \coloneqq \sum_{l=1}^{L} I_l \Phi - \int_\Omega (\nabla \cdot J^p) \, \varphi \, \mathrm{d}V$$

*with* $J_P \in H^1(\Omega)$, $(I_l)_l \in \mathbb{R}^L$.
*Additionally it shall be:*

$$\int_\Omega \nabla \cdot J^p \, \mathrm{d}V = \sum_{l=1}^{L} I_l$$

*If then* $X \subset H^1(\Omega)$ *is a closed finite-dimensional subspace or* $X = H^1(\Omega)$, *there exist* $u_P \in X$, $\hat{u_C} = (u_C, U_c) \in X \times \mathbb{R}^L$ *with*

$$\beta_P(u_P, \varphi) = f_P(\varphi) \quad \forall \varphi \in X \tag{3.20}$$
$$\beta_C(u_C, U_c, \varphi, \Phi) = f_C(\varphi, \Phi) \quad \forall (\varphi, \Phi) \in X \times \mathbb{R}^L \tag{3.21}$$

*and* $u'_P \in X$ *is an alternative solution of 3.21 if and only if:*

$$u'_P = u_P + c$$

*for any* $c \in \mathbb{R}$. *Analogously* $\hat{u_C}' = (u'_C, U'_C) \in X \times \mathbb{R}^L$ *is a solution of 3.21 if and only if:*

$$\hat{u_C}' = \hat{u_C} + c_L$$

*with* $c_L = (c, c, \ldots, c) \in \mathbb{R}^L$, $c \in \mathbb{R}$ *arbitrary.*

Proposition 3.1 delivers a solution for the PEM and the CEM, regarding to the last two paragraphs. Then with 3.4 we can fix the constant $c$ and get a unique solution.

# 4. Computation

## 4.1. Discretization

### 4.1.1. FEM: a short introduction

To facilitate the understanding of the following paragraphs this chapter will start with a short overview of the basic principles of the finite element method (FEM). For a detailed introduction see e.g. [3].
(This section follows ([3],II.4-II.5) and [32])

#### Galerkin Method

We have seen in the last chapter that we can find a unique solution for each of the described models. However, this solution is not easy to find. To solve the problem numerically one searches for an approximation instead. Therefor instead of a solution $u \in H^1(\Omega)$ with

$$\beta(u, \varphi) = f(\varphi) \quad \forall \varphi \in H^1(\Omega)$$

one can search for a solution $u_h \in S_h$ in a finite-dimensional subspace $S_h \subset H^1(\Omega)$ with:

$$\beta(u_h, \varphi_h) = f(\varphi_h) \quad \forall \varphi_h \in S_h \tag{4.1}$$

Since $S_h$ is finite-dimensional there exists a basis $(\psi_j)_{1 \leq j \leq N}$, and hence the equation above is already solved for all $\varphi_h$ if

$$\beta(u_h, \psi_i) = f(\psi_i) \quad \forall\, 1 \leq i \leq N \tag{4.2}$$

Moreover, $u_h$ can be described with:

$$u_h = \sum_{j=1}^{N} y_j \psi_j$$

for constants $y_j \in \mathbb{R}$ and equation 4.2 becomes:

$$\sum_{j=1}^{N} u_j \beta(\psi_j, \psi_i) = f(\psi_i) \quad \forall 1 \leq i \leq N \tag{4.3}$$

which can also be described in a matrix form:

$$By = \beta(\psi_j, \psi_i)_{i,j}(y_j)_j = f(\psi_i)_i \tag{4.4}$$

This equation can be solved then with respect to $y$. This is called the *Galerkin method*, or rather Ritz-Galerkin method if $\beta$ is symmetric and positiv definite [3]. (The bilinear forms described above are not positive definite in general, but they are if restricted to the space $V_0 = \{\varphi \in H^1(\Omega) | \int_\Omega \varphi = 0\}$, like shown in section 3.2.3.)

**Finite elements**

Searching for a family of functions which make calculations as easy as possible one often uses a finite element method:
Here the area $\Omega$ is divided into simpler parts, mostly polyhedra, e.g. tetrahedra or prisms. Every function $\psi_i \in S_h$ has to fulfill certain conditions on such a part. Mostly it is: $\psi_{i|T} \in \mathbb{P}_k$, where $\mathbb{P}_k$ is the polynomial space of degree $k$. However, in general $\psi_{i|T}$ has only to lie in $C(T)$ [3]. A *finite element* then is the combination of the polyhedron, the function $\psi_{i|T}$ and a set of functionals, which can be used for a unique description of the functions. A common finite element, which is also the one used in this work is the following:

**Definition 4.1 (*Linear Lagrange elements*)**

*A linear 3-dimensional Lagrange element is the triple $(T, \Psi, \mathcal{N})$ with the following properties:*

- *$T$ is a tetrahedron in $\mathbb{R}^3$, (also called a 3-dimensional simplex)*
- *$\mathcal{N}_T = \{a_1, a_2, a_3, a_4\} \in \mathbb{R}^3$ is the set of nodes defining the vertices of the simplex*
- *$\Psi_T = \{\psi_j | \psi_j(a_i) = \delta_{i,j}\} \subset \mathbb{P}_1(T)$ is the nodal basis of $\mathbb{P}^1(T)$. (The basis functions of a finite element are also called the shape functions)*

At the first view the set $\mathcal{N}_T$ does not define a set of functionals here. However one can identify each vertex $a_i$ with the functional $N_i(\psi) = \psi(a_i)$. These functionals uniquely define each polynom in $\mathbb{P}^1(T)$ since every linear polynom is already well-defined by given values at the vertices of the tetrahedron (see [3] for a proof). This also shows that $\Psi_T$ is indeed a basis of $\mathbb{P}_1(T)$.

We can now subdivide $\Omega$ into a set of such tetrahedra $T_n$, i.e it has to hold

$$\Omega = \bigcup_{n=1}^{N} T_n \tag{4.5}$$

and additionally:

$$T_i \cap T_j = 0 \text{ or } T_i \cap T_j \text{ is a vertex, an edge or a side face of } T_i \text{ and } T_j \tag{4.6}$$

If 4.5 and 4.6 hold, the set $\mathcal{T} = \{T_n | 1 \leq n \leq N\}$ is called a *feasible decomposition.*

If now $\mathcal{T}$ is a feasible decomposition we can combine finite elements. We define the linear Lagrange space $S_h^1$:

$$S_h^1 = \{\psi \in C^0(\Omega) | \psi_{|T} \in \mathbb{P}_1(T), T \in \mathcal{T}\}$$

If then $\mathcal{N} = \{a_i | 1 \leq i \leq N\}$ is the union of $\bigcup_{T \in \mathcal{T}} \mathcal{N}_T$, one can prove again that the set of functions

$$\Psi = \{\psi_j | \psi_j(a_i) = \delta_{i,j}\}$$

forms a basis of $S_h^1$ and hence all functions in $S_h^1$ are uniquely defined by the specification of values on all given nodes in $\mathcal{N}$.

The benefit of the finite element approach is that due to the unique structure of the finite elements one usually only has to make computations for one element, and map the results to the other elements afterwards. Furthermore, each element supports only a small number of basis functions. In case of the Lagrange elements, every function $\psi_i$ is supported only at the adjacent tetrahedra to the node $a_i$.

We will therefore assume in the following that $\mathcal{T}$ is a feasible triangulation (i.e. a composition using tetrahedra) of $\Omega$, at which $N$ is the number of nodes (i.e the dimension of $S_h^1$), $K$ is the number of tetrahedra and $M$ the number of 2-dimensional faces. Furthermore, $S_h^1$ shall be defined as above and $\Psi = \{\psi_i | 1 \leq i \leq N\}$ is the nodal basis of $S_h^1$.

### 4.1.2. Stiffness matrices

With the descriptions from the last section we can discretize the unknown potential $u$ with:

$$u_h = \sum_{i=1}^{N} y_i \psi_i$$

and find matrices describing the bilinear forms like explained in the last section.

Based on this approach one can now find the matrices $L_{tES}$ and $L_{tES2}$ which describe the relationship between $I$ and the resulting potentials (cf. section 2.3.2):

$$L_{tES_1} I = U, \quad L_{tES_2} I = y,$$

Although the main focus of this work is the implementation of the CEM and PEM in tES, each section will also give a description of a lead field matrix $L_{EEG}$.
This is because the original code is written for the implementation in EEG. Hence the description is necessary to get a better idea of the changes that were done in the code. Like already said in 2.3.2 the lead field matrix describes the connection between current sources inside of the head which form the primary current $J^p$ and the resulting electrode potentials:

$$L_{EEG} x = U$$

The vector $x$ represents the primary current $J^P$, i.e. the existing dipoles in the head. Normally $x$ is referring to a number of unit dipoles which are oriented parallel to the x, y- and z- axis and are localized at each possible dipole position of the mesh (cf. section 2.3.2). This means for $M$ dipole positions x is of length $3M$.

However, in the given case another representation of $J^P$ is used. It is discretized by a family of lowest order Raviart-Thomas basis functions ($\omega_k$):

$$J^P = \sum_{m=1}^{M} x_m \omega_m$$

As stated before, $M$ is the number of 2-faces of the mesh. The number of R-T functions is equal to $M$, because every function $\omega_m$ is supported on two adjacent tetrahedra of the mesh, i.e. refers to the face both tetrahedra share.
The original code uses R-T functions as a discretization of $J^p$ because it aims to calculate the matrix $G$ directly [1], i.e. to compute $\int_\Omega \nabla \cdot J^P \, \mathrm{d}V$. This cannot be done using a dipole vector field. Therefore one can use a number of basis functions again. R-T functions are the most reasonable choice here, since they are the simplest functions to have square integrable divergence [38].
Since the focus of this work is not the EEG but the tES, where the R-T functions are not needed, they won't be described here in detail. For further information see for example: [40], [38] or [3]. However, it is important that R-T functions can be represented as dipoles again: One can find a dipole moment vector $q_m e_m$ and a position $r_m$ for every $\omega_m$. Hence the vector $x$ can again be seen as a dipole vector field. Furthermore, we can convert this vector field to an euclidian field again: The euclidean dipole of every element can be calculated with the help of the four R-T-functions, which are supported on the element. This is also described in [40] and [38].

Now we have in fact three different cases for both tES and EEG. All three of them were investigated in [39] and hence in the original code: The CEM, the PEM and a model 'in-between', which is the CEM with $Z_l \longrightarrow \infty$ (cf. 3.1.2).

### CEM

We will start with the CEM here, since the other models are special cases of it (cf. section 3.1.2).

[1] Calculating G directly is only one possible approach. It is for instance not necessary to compute the matrix $G$ if the reciprocity principle (cf. section 2.3.2) is being used.

In section 3.2.2 we have received the equations:

$$\forall \varphi \in H^1(\Omega) : \sum_{l=1}^{L} \int_{e_l} \frac{1}{Z_l} (U_l - u)\, \varphi \, \mathrm{d}S - \int_\Omega \nabla u \cdot \nabla \varphi \, \mathrm{d}V = \int_\Omega (\nabla \cdot J^p)\, \varphi \, \mathrm{d}V \tag{3.9}$$

$$\forall\, 1 \leq l \leq L : \qquad \frac{1}{Z_l} \int_{e_l} (U_l - u)\ \mathrm{d}S = I \tag{3.10}$$

We can now define the matrices $A$, $B$, $C$ by:

$$\begin{aligned} a_{i,j} &= \int_\Omega \sigma \nabla \varphi_i \cdot \nabla \varphi_j + \sum_{l=1}^{L} \frac{1}{Z_l} \int_{e_l} \varphi_i \varphi_j \, \mathrm{d}S \\ b_{i,l} &= -\frac{1}{Z_l} \int_{e_l} \varphi_i \, \mathrm{d}S \\ c_{l,l} &= \frac{1}{Z_l} \int_{e_l} \mathrm{d}S, \quad c_{i,l} = 0 \text{ otherwise} \end{aligned} \tag{4.7}$$

Since $J^P = 0$ in the tES, the equation system (3.9, 3.10) can be described by:

$$\begin{pmatrix} A & B \\ B^T & C \end{pmatrix} \begin{pmatrix} y \\ U \end{pmatrix} = \begin{pmatrix} 0 \\ I \end{pmatrix} \tag{4.8}$$

This system delivers:

$$\begin{aligned} L_{tES_1} I &= -\left(B^T A^{-1} B - C\right)^{-1} I = U \\ L_{tES_2} I &= -A^{-1} B U = -A^{-1} B L_{tES_1} I = y \end{aligned} \tag{4.9}$$

In the EEG the current density $J^P$ has to be taken into account, and an additional matrix $G$ has to be defined:

$$g_{i,k} = \int_\Omega (\nabla \cdot \omega_k) \psi_i \, \mathrm{d}V \tag{4.10}$$

Equation 4.8 becomes:

$$\begin{pmatrix} A & B \\ B^T & C \end{pmatrix} \begin{pmatrix} y \\ U \end{pmatrix} = \begin{pmatrix} -Gx \\ 0 \end{pmatrix} \tag{4.11}$$

In this case, it we search for a correlation with $x$:

$$L_{EEG} x = \left(B^T A^{-1} B - C\right)^{-1} B^T A^{-1} G x = U$$

### PEM and infinite impedances

For the PEM it holds (cf. section 3.2.1):

$$\forall \varphi \in H^1(\Omega): \int_\omega \nabla u \cdot \nabla \varphi \, \mathrm{d}V + \sum_{i=1}^{L} \frac{I_l}{|e_l|} \int_{e_l} \varphi \, \mathrm{d}S = \int_\Omega (\nabla \cdot J^p)\, \varphi \, \mathrm{d}V \tag{3.14}$$

$$\text{If } I_L \neq 0: \int_{e_l} u \, \mathrm{d}S - |e_l| \cdot U_l = 0, \quad u(p_l) = U_l \quad \text{sonst} \tag{3.15}$$

In case of infinite impedances, we will receive quite similiar equations: If we have a look at equation 3.9 in the section above again, we will notice that the first summand vanishes for all EEG electrodes if $Z_l$ converges to infinity. However, in section 3.1.2 we have seen that we have to exclude the electrodes where a stimulation takes place. These have either to be modelled with the CEM or already with the Gap model. Here the Gap model is chosen and therefore equation 3.9 holds for the infinite impedance case as well. This is no surprise, since it was already stated in section 3.1.2 that $Z_l \longrightarrow \infty$ already delivers the same behavior for $u$ like the PEM does.
The only difference for the infinite case is that the left hand side of 3.15 now hold for all electrodes instead:

$$\forall\, 1 \leq l \leq L: \quad \int_{e_l} u \, \mathrm{d}S - |e_l| \cdot U_l = 0 \tag{3.15 a}$$

Thus, for the infinite impedance model, we rearrange the matrices described for the CEM above and get the alternative matrices $A_\infty$,$B_\infty$ and $C_\infty$ instead:

$$\begin{aligned} a_{\infty i,j} &= \int_\Omega \sigma \nabla \varphi_i \cdot \nabla \varphi_j \\ b_{\infty i,l} &= \int_{e_l} \varphi_i \, \mathrm{d}S \\ c_{\infty l,l} &= \int_{e_l} \mathrm{d}S, \quad c_{i,l} = 0 \text{ otherwise} \end{aligned} \tag{4.12}$$

which fulfill:

$$\begin{pmatrix} A & 0 \\ B_\infty^T & C_\infty \end{pmatrix} \begin{pmatrix} y \\ U \end{pmatrix} = \begin{pmatrix} Gx - B_\infty C_\infty^{-1} I \\ 0 \end{pmatrix} \tag{4.13}$$

We notice that $\lim_{Z_l \longrightarrow \infty} B \neq B_\infty$ and $\lim_{Z_l \longrightarrow \infty} C \neq C_\infty$. This is because these matrices are only needed for equation 3.15 a) now, which doesn't include information about $Z_l$.

For the tES that delivers ($G = 0$):

$$\begin{aligned} y &= L_{tES_2} I = -A^{-1} B_\infty C_\infty^{-1} I \\ U &= L_{tES_2} I = C_\infty^{-1} B_\infty^T y = C_\infty^{-1} B_\infty^T L_{tES_2} I \end{aligned} \tag{4.14}$$

and for the EEG ($I = 0$) we receive:

$$C_\infty^{-1} B^T A^{-1} G x = U \tag{4.15}$$

To get the PEM model again, the computation of the EEG voltages has to be changed. Now equation 3.10 holds again. Instead of $B_\infty$, $C_\infty$ one could define $B_P$, $C_P$:

$$\begin{aligned} b_{Pi,l} &= \int_{e_l} \varphi_i \, \mathrm{d}S \text{ if } I_l \neq 0 \quad b_{Pi,l} = \psi_i(p_l) \text{ otherwise} \\ c_{Pl,l} &= \int_{e_l} \mathrm{d}S \text{ if } I_l \neq 0 \quad c_{Pi,l} = \delta_{i,l}, \text{ otherwise} \end{aligned} \tag{4.16}$$

Then for the PEM one can use the same equations systems as described in the infinite case. In a normal EEG $C_P$ is simply the unit matrix(cf. [39]). However, it is important here that it makes no difference if equation 3.14 is described with:

$$Ay = Gx - B_\infty C_\infty^{-1} I$$

or

$$Ay = Gx - B_P C_P^{-1} I$$

because $I_l = 0$ for all normal electrodes anyway. Like already said before, the only difference in both systems is the computation of $U$.

## 4.2. Implementation

### 4.2.1. Efficient computation

Regarding the equations of the last chapter, the computation of the solutions might become a complex task: In all cases one has to compute the inverse of the matrix $A^{-1} \in \mathbb{R}^{N \times N}$. Although $A$ is a sparse matrix, i.e. most of the entries are zero, that does not hold for the inverse matrix. Since every mesh which is fine enough to allow a realistic simulation of the electric currents contains a huge number of nodes $N$, this would require a large amount of computer memory.
This is a well known problem concerning the EEG forward problem and possible solutions are for example described in [56]: It makes sense here not to treat $A^{-1}$ separately but in combination with other matrices, which are multiplied by $A^{-1}$. Luckily, the matrix A is meant to be mapped to the electrode potentials anyway. This is done by the Matrix $B^T \in \mathbb{R}^{L \times N}$. Hence, we examine the matrix $T = B^T A^{-1}$ instead, because $A$ is always involved in this form or as $T^T = A^{-1} B$, respectively.
Then $T$ is a $\mathbb{R}^{L \times N}$ matrix which can be solved much easier:
One can now use an iterative method to solve the system: $B = AT^T$, which means that one has to solve $L$ equations instead of $N \gg L$ equations now. In the given case a classical PCG-iteration was used.

### 4.2.2. Description and comparison of code versions

This thesis is mainly based on the code used in [39], which was originally computed to compare different lead field matrices in the EEG. It was part of this work to modify this code for combined tES and EEG. This section shall now give an overview about the function of both versions. The complete code can be found on the attached CD.

Since the original code and the modified version follow the same idea, we start with a description of the general structure.

| **Original code (EEG)** | **Modified version (tES)** |
|---|---|
| **Data**: nodes,elements,sigma electrodes,varargin | **Data**: I,nodes,elements,sigma electrodes,varargin |
| **Result**: $L_{EEG}$, locations and directions of dipoles | **Result**: $U$,$y$ |
| read in data; | - |
| identify model ; | read in data; |
| Calculate A,B,C,G; | identify model ; |
| solve $AT^T = B$ with a PCG iteration; | Calculate A,B,C; |
| calculate $L_{EEG}$; | solve $AT^T = B$ with a PCG iteration; |
| **if** *directionmode=cartesian* **then** | calculate $U$,$y$; |
| transform $L_{EEG}$; | - |
| **end** | - |
| | - |

#### Input

The required input is very similar for both code versions. In both cases the mesh is given by the three matrices "'nodes"', "'elements"' and "'sigma"'. Thereby "'nodes"' defines the euclidian coordinates of the nodes, "'elements"' defines each element of the mesh as it gives a set of nodes for each element and "'sigma"' describes the conductivities for each of these elements. In the original code "'elements"' can include simplices, i.e. a tetrahedrical mesh like it was described in section 4.1, as well as prisms. However, in the concrete case a pure tetrahedrical mesh was used, and therefore the tES code was only changed for the tetrahedrical version.
Next to the mesh the input also requires the matrix "'electrodes"', which gives either a description of the electrode centers or those triangles on the border which are meant to be covered by an electrode. Furthermore, the struct "'varargin"' can specify a number of optional parameters. That information includes additional computation options like the limit of tolerance for the PCG iteration. However, "'varargin"' may also give important information like the ECI of each electrode.
In case of the tES, we need the additional vector $I$, which gives the applied current at every electrode in $mA$.

### Output

The output of the code was different for both versions:
The original code calculates the lead field matrix $L_{EEG}$. Since $L_{EEG}$ was calculated with help of the Raviart-Thomas basis functions it does not refer to euclidian dipoles by default, like it would usually be the case for $L_{EEG}$. Instead, it refers to those dipoles which match the positions of the Raviart-Thomas basis functions. Hence, by default we need additional information about dipole locations and directions, which is given as a second output. However, it is also possible to give a description of the matrix in the common form. This output form can be specified by an optional parameter in "'varargin"'(directionmode=cartesian). If this option is chosen the matrix $L_{EEG}$ will be recalculated at the end of the code. The output will then be given referring to euclidian dipoles and the output vector of dipole directions will be empty (since those are clear-cut in this case).
The modified version of the code does not yield the calculated matrices as a result, but does rather directly calculate the vector $U$ which specifies the electrode potential for each electrode and the general potential vector $y$, which describes the potential at each node of the mesh. It would of course also be possible to calculate the matrices $L_{tES}$ and $L_{tES2}$ instead. This would be a more general result since it could be applied to every input current distribution $I$. However, in most cases every distribution of applied current will require its own mesh, since the stimulation electrodes are normally bigger and maybe even of a different shape than the other electrodes. Since saving the involved matrices would also need much more memory than just saving the resulting potentials, potentials are calculated directly here. Still, it would not require complex changes to the code to give out the involved matrices instead.

### General structure and choice of model

In both cases the form of the input (form of "'electrodes"', existence of certain values in "'varargin"') defines which model (PEM or CEM or infinite impedances) is used by the code. There are some internal parameters, which change depending on the given input. The code will then compute all necessary matrices $A$,$B$,$C$,$G$ and the matrix $T^T$ (cf. last section), which is used to produce the final output.

The next two sections will describe both versions of the code in detail.

### Code in EEG

Algorithm 1 shall give an idea of the algorithm of the EEG code. Note that the algorithm is simplified, and that in the real code some computations are made in a different order.

As already described in section 4.1, three different models can be computed: CEM, PEM and the CEM with infinite impedances.

The three different cases are differed with help of two variables in the original code: *electrode_ model* which can be CEM or PEM and *inf_ impedance*, which is boolean (i.e. 1 or 0 in matlab) and specifies if the impedances for the CEM are supposed to be infinite or not. The values of these parameters are based on the input: If "'electrodes"' is a matrix containing a sample of triangles for each electrode, *electrode_ model* is set to "'CEM"', otherwise it is assumed that "'electrodes"' does only contain the positions of the electrodes and $L_{EEG}$ is computed for the "'PEM"' instead. Moreover, if varargin contains a vector "'impedances"', *inf_ impedance* is set to false (which is only relevant for the CEM), otherwise the impedances are supposed to be infinity. To simplify matters, algorithm 1 assumes that those identification parameters are already given.

The computation is straightforward: It starts with the calculation of the matrices $A$,$B$,$C$ and $G$, which are calculated corresponding to the chosen model .
However, in case of the PEM matrices A and G are computed only. The reason becomes clear if we have a look at equation 4.16 again: In case of the PEM the matrix $C$ becomes the unit matrix. It has to be computed: $L_{EEG}x = B^T A^{-1} G x = U$. Furthermore, we simplify the case of the PEM in the code and identify every electrode position with the node $elecind(i)$ next to it. Then $B$ just becomes: $B_{i,l} = \delta_{elecind(i),j}$ and can be directly used in the PCG-iteration loop as it does not need additional calculation.
In case of the CEM, the calculation of $B$ and $C$ has to be done for every element of the mesh using some geometrical considerations which are described in the appendix in more detail (ref). In case of the infinite impedances only the first summand of $A$ has to be computed. Additionally, $B$ and $C$ have to be calculated without $Z_l$, which is realized here by setting $Z_l = 1$. Hence for *inf_ impedance=false* the code delivers the matrix system described in 4.14. Similarly, *inf_ impedance=true* and *electrode_ model=CEM* deliver the model of the normal CEM.
After the calculation of the matrices, the PCG-iteration is made separately for every column of $T^T$. Moreover, due to the form of the term which describes $L_{EEG}$, most calculations can already been done separately for those columns (i.e. the rows of the matrix $T$). As the final step the mean of $L_{EEG}$ is subtracted and $L_{EEG}$ is also divided by the dipole strength. This is because the current dipoles belonging to the Raviart Thomas functions are not of unit length originally, but are normalized later.

## Code in tES

In the tES we have the same distiction between PEM, CEM and the CEM with infinite impedances as in the EEG. However, we have to be aware that we will never have a "'pure"' PEM, since anode and cathode will always have to be calculated with respect to their size. To make this difference clear, we define the boolean specification variable *gappem*, instead of *electrode_ model=PEM*. If *gappem* is set true, it is assumed that the PEM shall be used for the EEG electrodes, while the gap model is used for anode and cathode. By default we set *gappem=false*.
In contrast to the EEG, the variable "'electrodes"' will always include the exact form

**Algorithm 1:** Matrix calculation for the EEG

**if** *electrodemodel=PEM;*
**then**
  $(eleind_l)_l$=node next to electrode position l;
**end**
**if** *electrodemodel=CEM AND infimpedance=false* **then**
  $(Z_l)_l$=varargin.impedances;
**else**
  $(Z_l)_l$=ones;
**end**
$A_{i,j} = \int_\Omega \nabla\psi_i \nabla\psi_j \mathrm{d}V$;
**if** *electrodemodel=CEM* **then**
  $B_{i,l} = \frac{1}{Z_l} \int_{e_l} \psi_i \mathrm{d}S$;
  $C_{i,l} = \frac{1}{Z_l} \int_{e_l} \mathrm{d}S$;
  **if** *infimpedance=false* **then**
    $A_{i,j} = A_{i,j} + \frac{1}{Z_l} \int_{e_l} \psi_i \psi_j \mathrm{d}S$
  **end**
**end**
$G = (\nabla \cdot \omega_k)\psi_i \, \mathrm{d}V$;
⋮
**for** *i=1:L* **do**
  **if** *electrodemodel=PEM* **then**
    $b_i = \delta_{eleind(i),j}$;
  **end**
  **if** *electrodemodel=CEM* **then**
    b=$B(:,i)$
  **end**
  solve $Ax = b_i$ with a pcg iteration;
  $L_{EEG}(i,:) = -x^T * G$;
  **if** *electrodemodel=CEM* **then**
    **if** *impedanceinf=0* **then**
      Auxmat(:,i)=$B^T x - C(:,i)$
    **else**
      Auxmat(:,i)=-C(:,i)
    **end**
  **end**
**end**
**if** *electrodemodel=CEM* **then**
  Auxmat=Auxmat$^{-1}$;
  $L_{EEG}$ =Auxmat*$L_{EEG}$
**end**
$L_{EEG}$ = ($L_{EEG}$−mean($L_{EEG}$))/dipole strength;

of the electrodes in case of the tES, since the exact form is needed for the stimulating electrodes. Therefore, we cannot use the form of "'electrodes"' here to specify *gappem*. Instead "'gappem"' is assumed to be true as soon as *varargin* includes the additional parameter *centerpoints*, which specifies the positions of the electrode centers. The modified code keeps the treatment of *inf_ impedance*: If *varargin* includes the parameter *impedance* we set *inf_ impedance=false*, otherwise impedances are assumed to be infinite (*inf_ impedance=true*).

Calculations of the matrices involved in the tCS forward calculation are the same as in the infinite and finite case of the CEM for EEG, while the final calculation of the output differs. This holds for the PEM/gap combination as well, since main calculations are the same as for the full infinite impedance model here. Hence, the main changes to the code appear in the final part.
Algorithms 2 and 3 show a direct comparison between the final part of the EEG forward simulation and the the modified code. In fact, the tES code follows exactly the equations described in Section 4.1.2.
Since the PEM is only a different version of the gap model, one can use a similar code for its calculation. Thereby, it is the simplest way to calculate the whole gap model and define the voltages of the point electrode based on the resulting skin potential in the gap model which was done in this version of the code.
Although the described approach will lead to good results, it is surely an expensive one. In fact, one could reduce the cost for the calculation of $T^T$ in case of the PEM and the infinite case: If we have a look at equation 4.14 again, we see that the expensive matrix $T^T = A^{-1}B_\infty$ is only needed for the calculation of $y$. But $y$ is linearly calculated from $I$, which vanishes almost everywhere. Therefore, one can conclude that we only need those columns of $T^T C_\infty^{-1}$ which refer to a stimulation electrode. Since $C_\infty$ is diagonal, this principle is passed to $T^T$: For *inf_ impedance=1* or the PEM (combined with the gap), $T^T$ has to be computed only for those columns belonging to stimulating electrodes. This highly reduces the cost of the PCG-iteration.
In case of the PEM/gap model one can reduce the costs even more. Here it is not necessary to calculate the matrices $B$ and $C$ completely, since these are only needed to compute $U_l$. However, for all normal EEG electrodes it is just $U_l = u(p_l)$. Hence, it would be sufficient to calculate $C_{l,l}$ and $B_{i,l}$ for all $l$ which belong to a stimulation electrode.

**Original code (EEG)**

**Algorithm 2:** Final calculation of EEG

```
⋮
for i=1:L do
    if electrodemodel=PEM then
        b_i = δ_{eleind(i),j};
    end
    if electrodemodel=CEM then
        b=B(:,i)
    end
    solve Ax = b_i with a pcg iteration;
    L_EEG(i,:) = −x^T ∗ G;
    if electrodemodel=CEM then
        if impedanceinf=0 then
            Auxmat(:,i)=B^T x − C(:,i)
        else
            Auxmat(:,i)=-C(:,i)
        end
    end
end
if electrodemodel=CEM then
    Auxmat=Auxmat^{-1};
    -
    -
    -
    -
    L_EEG =Auxmat*L_EEG
end
-
-
-
-
-
-
-
-
-
L_EEG = (L_EEG−mean(L_EEG))/dipole strength;
```

**Modified version (tES)**

**Algorithm 3:** Final calculation of tES

```
⋮
for i=1:L do
    b=B(:,i);
end
-
-
-
-
solve Ax = b_i with a pcg iteration;
T^T = x;
-
if impedanceinf=0 then
    Auxmat(:,i)=B^T x − C(:,i)
else
    Auxmat(:,i) = −B^T x
end
-
-
if impedanceinf=0 then
    Auxmat=Auxmat^{-1};
else
    C = C^{-1};
    Auxmat = C ∗ Auxmat ∗ C;
end
U=-Auxmat*I;
if impedanceinf=1 then
    y = −T^T ∗ C ∗ I;
else
    y = −T^T U ;
end
if gappem=1 then
    CP_l=nodes next to electrode
    position l;
    U(EEG)=y(CP(EEG));
end
y=y-mean(U);
U =U-mean(U);
```

# 5. Numerical Experiments

## 5.1. Mesh

### 5.1.1. Head model

For the numerical experiments the same mesh as in [39] was used. The basis of the mesh were the T1- and T2- weighted magnetic resonance images of a healthy 24-year old subject. The combined data[1] was segmented into the most important brain tissues using different techniques. After that a mesh was extracted from the data, using the software CURRY. For a deeper insight into the construction methods used for this mesh see [39].
The result was a tetrahedrical mesh, divided into six compartments, including two different structures of the skull and CSF (cf. 2.1.1), brain and skin. Furthermore, skull holes like the foramen magnum[2] and the optic canals were incorporated [39]. Table 5.1 shows the exact number of nodes as well as the tissue segmentation, including the assumed conductivities.
Segmentation of brain meshes can be done with more or less accuracy. In the last years there were several studies concerning this topic. It has been shown for example, that a differentiation of gray and white matter has a significant effect on numerical results, as well as the consideration of the anisotropic behavior of those tissues [53]. However, we will see that the difference between CEM and PEM is not relevant enough in the brain,

[1] The T2 data was registered to the T1 data, i.e T2 images were mapped to T1 images
[2] This is were the spinal cord enters the brain. It is the biggest opening in the skull.

| **Number of...** | |
|---|---|
| Nodes | 628 032 |
| Tetrahedra | 3 912 563 |

***(a)*** *Size of the mesh*

| **Tissue** | **Conductivity ($\sigma$)** |
|---|---|
| Skin | 0.43 |
| Skull compacta | 0.0064 |
| Skull spongiosa | 0.02865 |
| Brain | 0.33 |
| CSF | 1.79 |
| Eyes | 0.505 |

***(b)*** *Conductivities*

***Table 5.1.:*** *Properties of the mesh*

| **EEG electrodes** | |
|---|---|
| Number | 77 |
| Radius | $\sim 6\,mm$ |

| **tES electrodes** | |
|---|---|
| Number | 2 |
| Radius | $\sim 12.5\,mm$ |

***Table 5.2.:*** *Size and number of electrodes*

making it unnecessary to take such effects into account.

### 5.1.2. Electrodes

For the simulations a set of 79 electrodes was used, which were directly included in the mesh. Therefor each electrode was identified with a number of faces on the surface of the head. Standard EEG electrodes were assumed to have an average radius of $6mm$. Furthermore, we assumed a stimulation of the auditory cortex. Because of that two electrodes over the ears were slightly moved and increased in their size, to represent anode and cathode.

## 5.2. Simulations

### 5.2.1. Used models and parameters

In all cases it was assumed that a current of 1 mA is applied to the head, at which the anode was the enlarged electrode above the left ear, while the corresponding electrode on the other side was assumed to be the cathode.

Potentials and currents where calculated using five different versions of the models described above:

- $\mathbf{CEM_{real}}$: The CEM with an impedance of $5\,k\Omega$ on each point of the electrode, i.e. an ECI $Z_l = 5\,k\Omega \cdot |e_l|$.
- **PEM**: The PEM in combination with the gap model for anode and cathode
- **INF**: Infinite impedances were assumed at the EEG electrodes, while the gap model was used for the stimulation. As already described in the last chapters, this model differs from the PEM only in the calculation of EEG potentials.

Additionally two combined models were used. Those used the realistic CEM at the stimulating electrodes, while EEG measurements were calculated with infinite impedances or point electrodes. The reason for these combined models is the current standard "'sponge"' model in tES simulation. Compared with the models used in this work, simulations of stimulations which use the "'sponge"' model can be assumed to lie between

results for stimulations using the CEM and results for stimulations using the gap model. Therefore, to get a realistic impression of model differences it makes sense to use both CEM and gap model for the stimulating electrodes. Hence, PEM and infinite case at the EEG electrodes were both combined with the standard CEM model at the stimulating electrodes:

- **C/I**: Infinite impedances at the EEG electrodes were combined with the CEM with a realistic impedance ($Z_l = 5\,k\Omega \cdot |e_l|$ ) at the anode and cathode.
- **C/P**: Point electrodes at the EEG electrodes were combined with the CEM with a realistic impedance ($Z_l = 5\,k\Omega \cdot |e_l|$ ) at the anode and cathode.

To compute these combinated results the CEM part of the code was used. Results at the EEG electrodes were approximated, using a CEM with very high impedances ($Z_l = 500\,\mathrm{M}\Omega \cdot |e_l|$) at the EEG electrodes.

Finally, in addition to those five realistic models another CEM model was computed:

- $\mathbf{CEM_{low}}$: A CEM with a very low contact impedance ($Z_l = 1\,\Omega \cdot |e_l|$). This impedance is highly unrealistic and only chosen for the demonstration of shunting effects.

### 5.2.2. Potentials

Potentials $U_l$ at the electrodes and the potential distribution $u$ were calculated for each model using the code described in 4.2. The distribution of both $U$ and $u$ were plotted for each model. Thereby $u$ was plotted on both the scalp and the brain surface.

#### Electrode comparisons

The relative difference between the electrode potentials was computed for different combinations of models. In each comparison the model which was closer to the PEM was used as the reference, which was the **INF** model in most cases. For example the comparison between $\mathbf{CEM_{real}}$ and **INF** was calculated via:

$$E_{U_l}(CEM, Inf) = \frac{U_{l,CEM} - U_{l,Inf}}{U_{l,Inf}}$$

at each electrode, while for the comparison between $\mathbf{CEM_{real}}$ and **C/I** it was computed:

$$E_{U_l}(CEM, C/I) = \frac{U_{l,CEM} - U_{l,C/I}}{U_{l,C/I}}$$

#### RDM and MAG

The potentials at skin and brain surface were compared using the RDM and MAG, which gives a description of topographic error and magnitude rerror, respectively, and are described as follows [34]:

$$RDM_{1,2}(T) = \left\| \frac{u_1}{\|u_1\|_{L^2(T)}} - \frac{u_2}{\|u_2\|_{L^2(T)}} \right\|_{L^2(T)}, \quad MAG_{1,2}(T) = \frac{\|u_1\|_{L^2(T)}}{\|u_2\|_{L^2(T)}}$$

Thereby 1 and 2 represent two different model versions.

### 5.2.3. Source simulations

As already stated in the introduction, the idea of this work was examining the significance of the CEM in tES, if compared to current sources in the head. Therefore, in the last experiment we assumed the existence of current sources $d$ in the head, which were represented by a set of dipoles (cf. 2.3.2). The lead field matrix $L_{EEG}$ was computed for the CEM using the original code and the EEG measurements due to the sources were simulated computing:

$$U(d) = L_{EEG}d$$

We used this test voltages to evaluate the voltage differences at EEG electrodes due to tES stimulation as they were described in section 5.2.2. For two different models $M_1$ and $M_2$ it was calculated:

$$E^d_{U(d)}(M_1, M_2) = \frac{U_{l,M_2} - U_{l,M_1}}{|U(d)|_l}$$

Again the model closer to the PEM was chosen as $M_1$. Moreover, to make a more conservative estimation of errors, $E^d_{U_l}(CEM, Inf)$ was just divided by the maximum value instead:

$$\widetilde{E^d_{U_l}}(M_1, M_2) = \frac{U_{l,M_2} - U_{l,M_1}}{\max_k |U(d)|_k}$$

### 5.2.4. Currents and lead fields

Current densities and leads in the brain were calculated from $u$ on each tetrahedron, using the formula:

$$\nabla u_{|T} = \sum_{i=1}^{4} y_{i_T} \nabla \varphi_{i_T}$$

with $a_{1_T} \cdots a_{4_T}$ being the four nodes of the tetrahedron. It was set:

$$L_{s1,s2} = \nabla u, \quad J = \sigma \nabla u$$

Here $L_{s1,s2}$ represents the lead field between anode($s_1$) and cathode($s_2$), while $J$ is a vector field representing the current density by a vector on each tetrahedron. For a closer description of the calculation of $\nabla\varphi_i$, see appendix. Section 2.3.2 ff. gives a description of the lead fields.

### Angle and magnitude differences

To illustrate the differences between the currents resulting from the different models, angles and magnitude differences were calculated on each tetrahedron:

$$\sphericalangle(j_1, j_2) = \frac{\langle j_1, j_2 \rangle}{\|j_1\| \, \|j_2\|}, \quad Mag(j_1, j_2) = \frac{\|j_1\|}{\|j_2\|}$$

# 6. Results

This chapter presents the results of the numerical experiments. We start with an overview on the EEG and skin potentials in section 1. This also includes a first comparison of all involved models. Section 2 will then give an impression of the current density inside of the brain, to find out if one can expect significant current differences due to the use of CEM. Finally, section 3 shows some simulated source induced EEG measurements and answers the question how strong the differences in section 1 are compared to those voltages.

## 6.1. Potentials

### 6.1.1. EEG measurements

We will start with an overview of the EEG potentials induced by the tCS. Figure 6.1 gives an impression of these potentials. It can be seen that distributions look exactly alike for all five models which reflects the linearity of the forward problem. This holds even for the low impedance model.
However, values are slightly different for the models (Table 6.2).Thereby, stimulation electrodes are presented separately. It can be seen that the CEM does not differ very much from the infinite impedance (INF) and the combined model (C/I) if realistic impedances are used. Differences appear at the stimulation electrodes only, which is not surprising, since the gap model was used here in the infinite case, while in case of $\text{CEM}_{\text{real}}$ and C/I the CEM was applied at the stimulation electrodes. Hence, due to the involved impedances potentials at anode and cathode are much higher for $\text{CEM}_{\text{real}}$ and C/I.
PEM and C/P show bigger differences to the other models. However, it has to be pointed out here again that the PEM is calculated in the same way as the INF (and the C/P in the same way as the C/I), hence the stronger effects are only due to the calculation of the final electrode potentials. Thereby, it is very important that points are only approximated here, since the nearest node of the mesh was used instead of the real center points.
The differences to the $\text{CEM}_{\text{low}}$ are more noticeable. This shows that higher differences due to the CEM are imaginable and that the potential tends to decrease if the impedance gets smaller, i.e. shunting effects seem to lower head potentials. Nevertheless, the impedance values of $\text{CEM}_{\text{low}}$ are highly unrealistic.

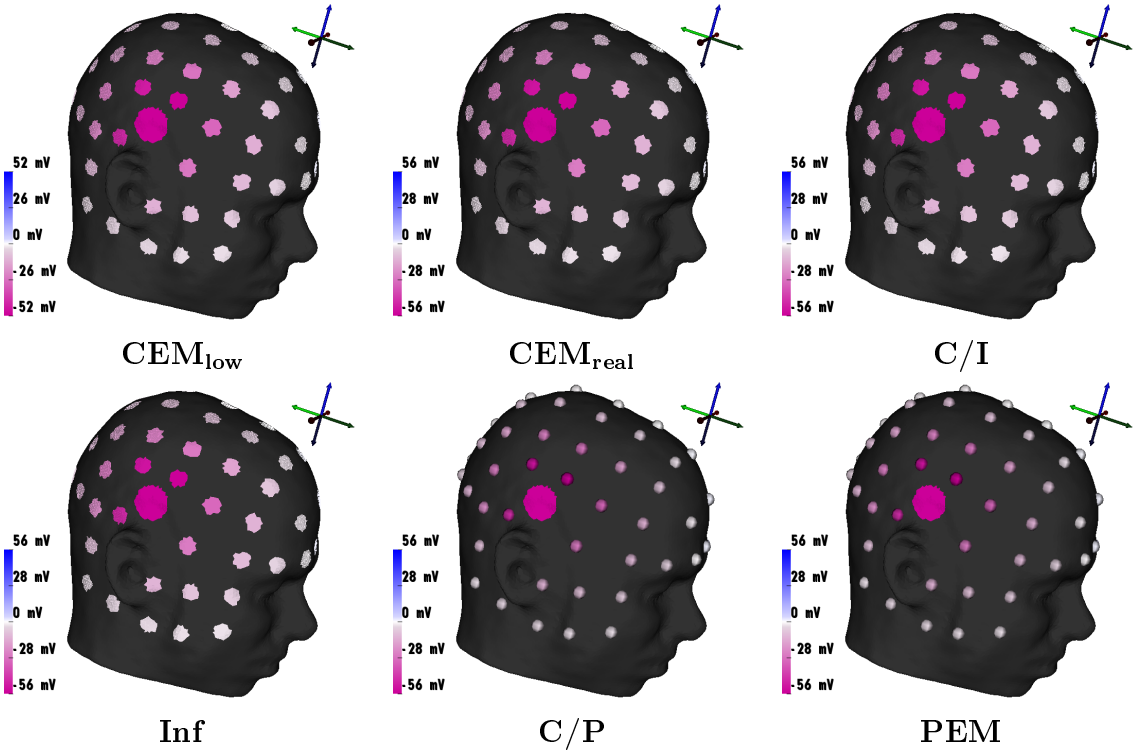


***Figure 6.1.:*** *EEG measurements due to different electrode models. To show the similarity of patterns, the spectrum of all pictures is restricted to the weakest and strongest value of pure measurement electrodes, i.e. potential at anode and cathode lie beyond the presented scale.*

| | EEG | | Stimulation | |
|---|---|---|---|---|
| | Min | Max | Anode | Cathode |
| **CEM$_{low}$** | −52.22 | 38.61 | 94.15 | −101.19 |
| **CEM$_{real}$** | −56.23 | 42.11 | 5108.1 | −5118.5 |
| **C/I** | −56.25 | 42.13 | 5108.1 | −5118.6 |
| **C/P** | −56.37 | 41.86 | 5108.1 | −5118.6 |
| **Inf** | −56.25 | 42.14 | 108.14 | −118.60 |
| **PEM** | −56.37 | 41.88 | 108.14 | −118.60 |

***Table 6.1.:*** *Overview of the electrode potentials occuring for different models (in* mV*)*

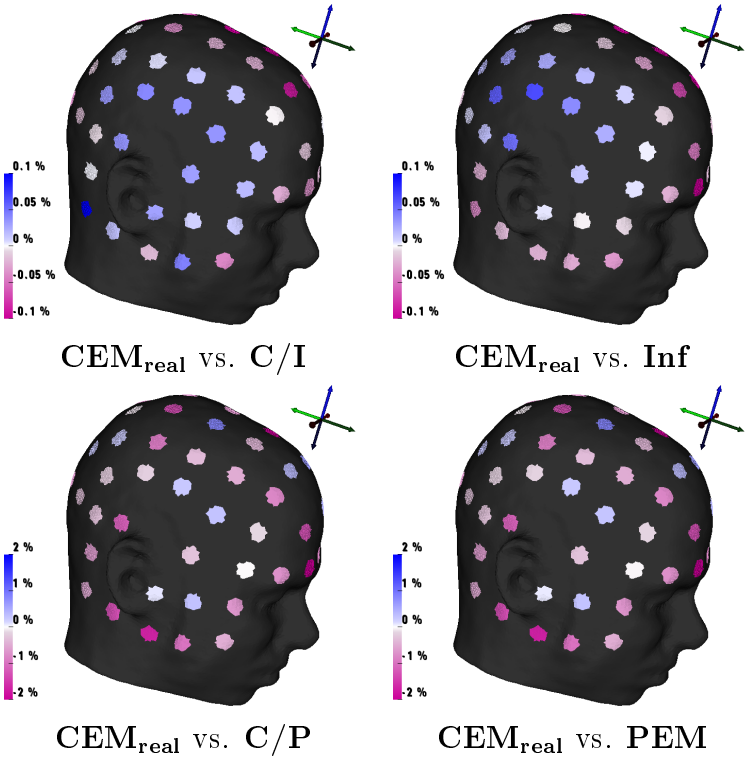


***Figure 6.2.:*** *EEG measurements of the CEM compared to those of other models (relative differences)*

### Differences

To get a better impression of the differences, the results of the models were directly compared to each other for eight different cases. First of all $\text{CEM}_{\text{real}}$ was compared to all other realistic models (Figure 6.2). Furthermore, C/I was compared to the INF, while C/P was compared to PEM to find out if different stimulation models lead to a significantly different behavior of potentials (Figure 6.3). Finally, the effect of the point size was investigated doing a comparison of Inf and PEM or C/I and C/P, respectively (Figure 6.4).
Table 6.2 presents an overview of common relative differences. In all cases there are few electrodes which tend to show extreme values greatly differing from the others. The majority of these outliers can be found on electrodes where the potential is almost zero, i.e. at the center of the head. Those values are less reliable, since it is likely that computation errors will occur if one divides by values near to zero. However, a few outliers can also be found at other electrodes. These electrodes are typically located next to the output electrode or at a few positions behind the ear. These values should not be excluded from interpretation. Anyway, the most extreme values are shown separately in Table 6.2, to give a better impression of more common values. Outliers at the center line are only presented in brackets. A detailed description of outliers and the corresponding electrodes is given in Appendix B.

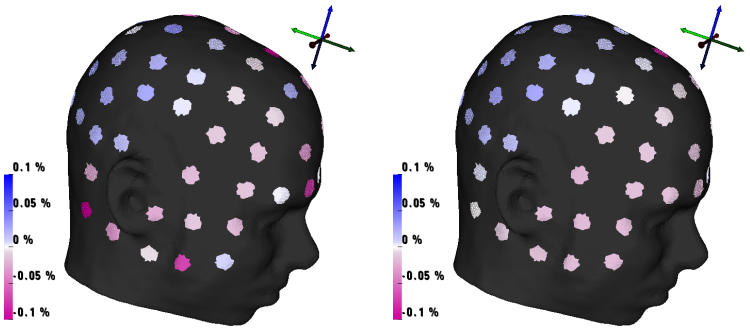


***Figure 6.3.:*** *Comparisons of different stimulation models (gap vs. CEM) for INF and PEM (relative differences)*

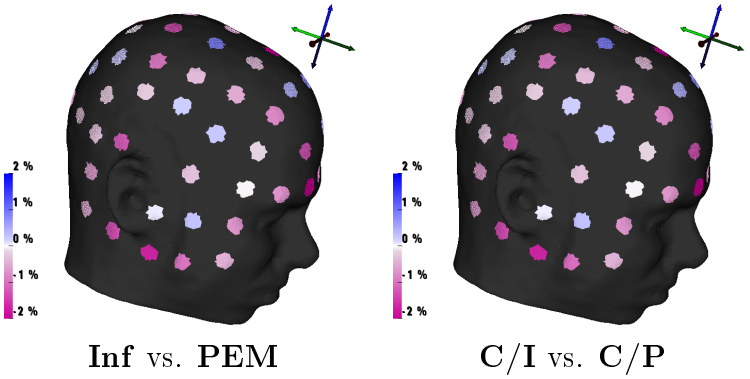


***Figure 6.4.:*** *Comparisons of INF and PEM or C/I and C/P, respectively(relative differences)*

| | General values | | Outliers | | | |
|---|---|---|---|---|---|---|
| | Min | Max | Min | | Max | |
| **$CEM_{real}$ vs. C/I** | −0.09% | 0.07% | - | (−1.76%) | 0.11% | |
| **$CEM_{real}$ vs. Inf** | −0.07% | 0.04% | - | (−2.55%) | 0.07% | |
| **$CEM_{real}$ vs. PEM** | −1.69% | 1.56% | - | (−42.72%) | 3.1% | |
| **$CEM_{real}$ vs. C/P** | −1.68% | 1.57% | - | (−42.67%) | 3.08% | |
| **C/I vs. Inf** | −0.06% | 0.05% | −0.15% | (−0.8%) | - | |
| **C/P vs. PEM** | −0.02% | 0.05% | - | (−0.08%) | - | (0.08%) |
| **Inf vs. PEM** | −1.68% | 1.60% | - | (−41.22%) | 3.10% | |
| **C/I vs. C/P** | −1.66% | 1.60% | - | (−41.64%) | 3.09% | |

***Table 6.2.:*** *Relative differences between EEG measurements in %. Outliers are presented on the right hand side. Outliers at the center line are only given in brackets (cf. Appendix B).*

Table 6.2 shows that neither of the presented values is of a significant magnitude. The highest differences can be found in comparisons involving PEM or C/P in combination with one of the other models. Comparisons between $\text{CEM}_{\text{real}}$ and C/I or $\text{CEM}_{\text{real}}$ and Inf deliver much lower values. Again, this suggests that the final calculation of the PEM, i.e. the choice of the electrode points, leads to much bigger differences than ignoring the shunting effects. This can also be seen in the direct comparison of INF and PEM (or C/I and C/P): Differences here are almost the same as differences between CEM and PEM (cf. Table and Figure 6.2).
The inaccuracy occuring due to the choice of the electrode points can also be observed in figure 6.2: The comparisons between CEM and infinite cases are comparatively smooth. Relative differences tend to be bigger near to the stimulation sides where electrode potentials are higher and tend to decrease with increasing distance to anode and cathode. In comparison, differences between CEM and PEM are distributed in a more irregular way: Adjacent electrodes tend to differ in magnitudes and even in polarities. This is due to the fact that inaccuracies in the choice of center points do not depend on the actual potential distribution, but occur in a more randomized way.
The lowest differences can be found in the comparisons C/I vs. Inf and C/P vs. PEM. Thereby, the values for the latter case seem to be even lower than those for the first one. This is noteworthy, since one would assume greater inaccuracies for the PEM. However, Figure 6.3 shows that both models show very similar magnitudes. The only differences can be found at some isolated electrodes lying at typical outlier positions. Indeed, one can see in appendix B that the highest values of the comparison of C/I and INF can be found at typical outlier electrodes or electrodes next to them. Comparing figure 6.3 and figure 6.2 indicates that the comparisons of different stimulation models deliver lower values than the other models.

### 6.1.2. Skin and brain potentials

#### Distribution

The next part shalldeals with the potential distribution on the skin. Just as in case of the electrodes, differences in potential distribution are not visible to the naked eye. Therefore, Figure 6.5 shows the potential distribution of the realistic CEM as an example for all cases.
However, to get an impression of distribution differences, Figure 6.6 illustrates the potential for the most important cases using another color scale. Even then, shunting effects in the realistic CEM are not visible. However, one can recognize the constant potentials underneath the electrodes in case of the low CEM.
Table 6.3 shows the maxima and minima on the surface of the head as well as the $L^2$-Norm over the surface. Note that INF and PEM as well as C/I and C/P describe the same model when it comes to potentials and currents in the head. Hence, to simplify explanations those models will often be referred to as PEM and C/P in the following sections.

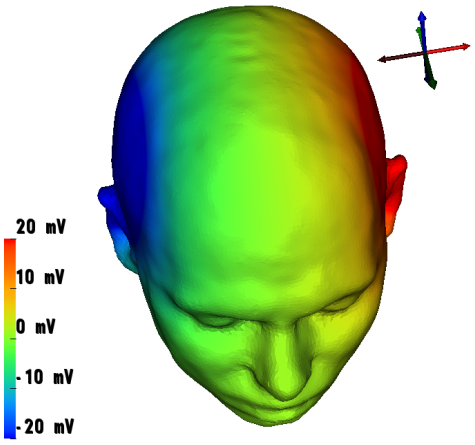


***Figure 6.5.:*** *Example of potential $y$ on the scalp. The spectrum was restricted to $20\,mV$. For a description of the magnitude of potentials see Table 6.3.*

| | Min | Max | $\|y\|_{L^2(\partial\Omega)}$ | $\frac{\|y\|_{L^2(\partial\Omega)}}{\|1\|_{L^2(\partial\Omega)}}$ |
|---|---|---|---|---|
| $\mathbf{CEM_{low}}$ | $-101.61$ | 94.33 | 6.395 | 17.531 |
| $\mathbf{CEM_{real}}$ | $-139.43$ | 126.66 | 6.926 | 18.987 |
| **Inf & PEM** | $-139.59$ | 126.78 | 6.929 | 18.995 |
| **C/I & C/P** | $-139.47$ | 126.68 | 6.929 | 18.993 |

***Table 6.3.:*** *Numeric description of scalp potentials(in $mV$)*

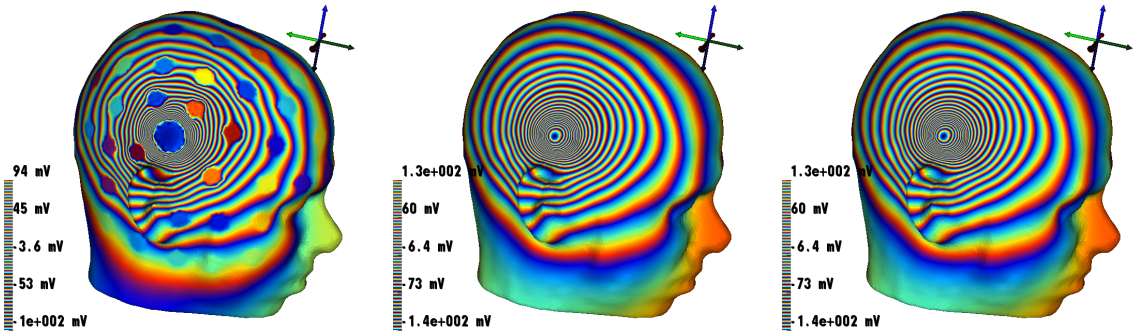


$\mathbf{CEM_{low}}$ $\mathbf{CEM_{real}}$ **PEM& Inf**

***Figure 6.6.:*** *Distribution of potentials (Visualization of shunting currents)*

Table 6.3 again reflects the fact that potentials hardly differ for realistic models. Moreover, one can see once more that the use of the CEM, i.e. the incorporation of the shunting effects, tends to decrease the magnitude of the potentials. This can be observed as values decrease if more electrodes are modeled with the CEM or the ECI is decreased. Looking at the norms of $y$ one can again see that the overall potential does hardly differ for PEM and C/P. However, this is different for the extrema. Here, the PEM shows the most deviating behavior compared to all realistic models. Since the most extreme values occur underneath the stimulating electrodes, this is not surprising: The PEM is the only model which does not use the CEM for stimulation. Anyway, these higher extrema seem to have no strong influence on the overall distribution.

### 6.1.3. RDM and MAG

Values as they are described in Table 6.3 give no idea of topographic differences. However, those can investigated by means of RDM and MAG. Figure 6.8 visualizes MAG and RDM for different comparisons. The resulting patterns come up to our expectations in all described cases, since they reflect differences in shunting currents quite well. However, we can see that the measured values are very low. This holds especially for pattern differences between PEM and C/P (note that different scales were used here and in the low impedance model), but also in other cases and corresponds to the observations described in the last paragraph.
To get an idea if the CEM has an influence on brain currents figure 6.7 shows MAG and RDM on the brain surface for the comparison between CEM and PEM. However, it is obvious that effects are very low here, again. Moreover, no remarkable change in the pattern can be seen. The strong red line represents the zero potential line again, which explains high values in this area (cf. section 6.1.1). We will investigate influences on the brain currents much closer in the next section.

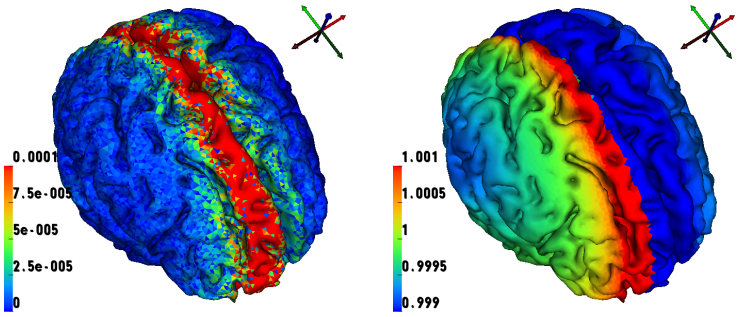


***Figure 6.7.:*** *RDM and MAG in the brain ($CEM_{real}$ vs. PEM/INF )*

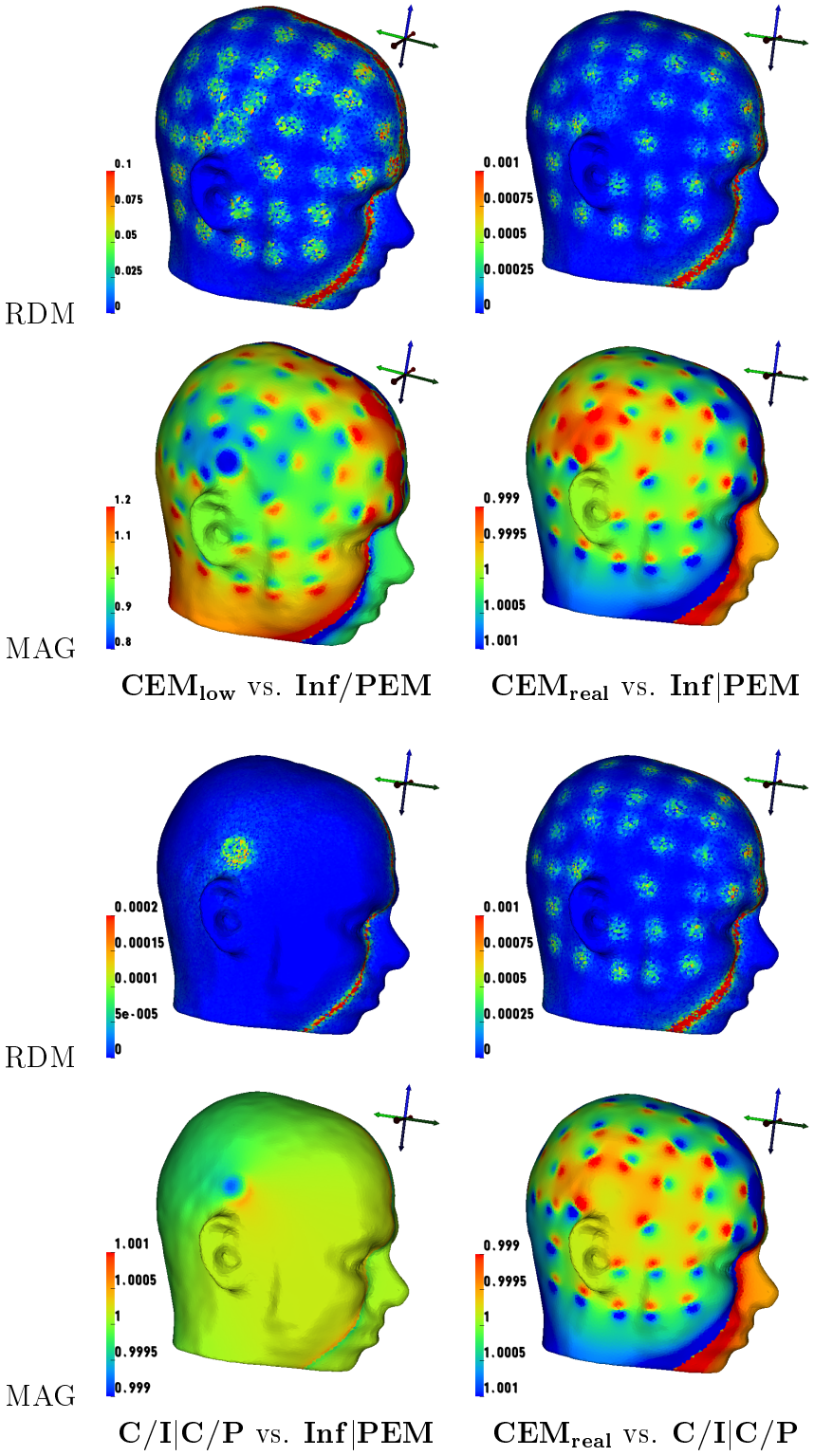


***Figure 6.8.:*** *MAG and RDM*

## 6.2. Currents

### 6.2.1. Current densities in head and brain

Before the current differences in brain and head are investigated we will have a general look at the current density. Table 6.4 gives an idea of typical current strength in brain and head. Again, we can see that all realistic models do not differ strongly.
If we do not take $CEM_{low}$ into account biggest differences of maximal current densities in the head can be found between the INF (or PEM) and the other models. This is due to the different modeling of the stimulation electrodes where the highest currents occur. Interestingly, the CEM increases maximal values here, while it was shown before that the maximal skin potentials are decreased by the CEM. The reason for this phenomenon can be seen in Figure 6.9. This figure shows the current density on the anode for $CEM_{low}$ and PEM. It can be seen here that currents in the CEM tend to concentrate on the edges of the electrodes. This occurs because the CEM allows for the current to distribute freely over the whole electrode. Since currents tend to flow through the skin rather than through the skull (because the skin is a better conductor) they will take the shortest way and leave the electrode at the edges. These strong currents are reflected by the maximum values in Table 6.4. In contrast the gap model (i.e. the PEM) forces the current to distribute evenly, i.e. the current density has to be constant in normal direction (cf. Section 3.1.2). However, the effects shown in Figure 6.9 are not as strong for the realistic CEM, therefore differences due to this phenomenon are very small.
In contrast to the whole head, differences inside of the brain seem to occur mainly due to the shunting effects at the EEG electrodes. This is indicated by the fact that in case of the brain it is the CEM that differs the most from the other models. Figure 6.10 shows the currents in brain and head exemplary for $CEM_{real}$ and PEM: It is visible here again that currents tend to flow through the skin instead of the brain. However, one can

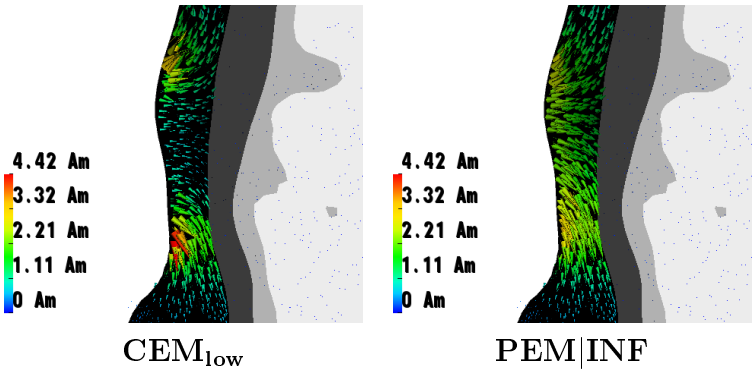


***Figure 6.9.:*** *Visualization of shunting effects at the anode. For low impedances currents tend to concentrate on the edges. The gap model (as it is used in PEM and INF) forces a more regular behavior. In reality shunting effects will be much smaller than demonstrated on the left hand side.*

| | $B$ | | $\Omega$ | |
|---|---|---|---|---|
| | Min | Max | Min | Max |
| **$CEM_{low}$** | 2.8704 | 83.2630 | 0.0056 | 5 8121 |
| **$CEM_{real}$** | 3.0521 | 89.5206 | 0.0075 | 4 2166 |
| **INF & PEM** | 3.0530 | 89.5476 | 0.0075 | 4 2160 |
| **C/I & C/P** | 3.0531 | 89.5498 | 0.0075 | 4 2166 |

***Table 6.4.:*** *Current extrema on brain $B$ and head $\Omega$ in $\frac{mA}{m^2}$*

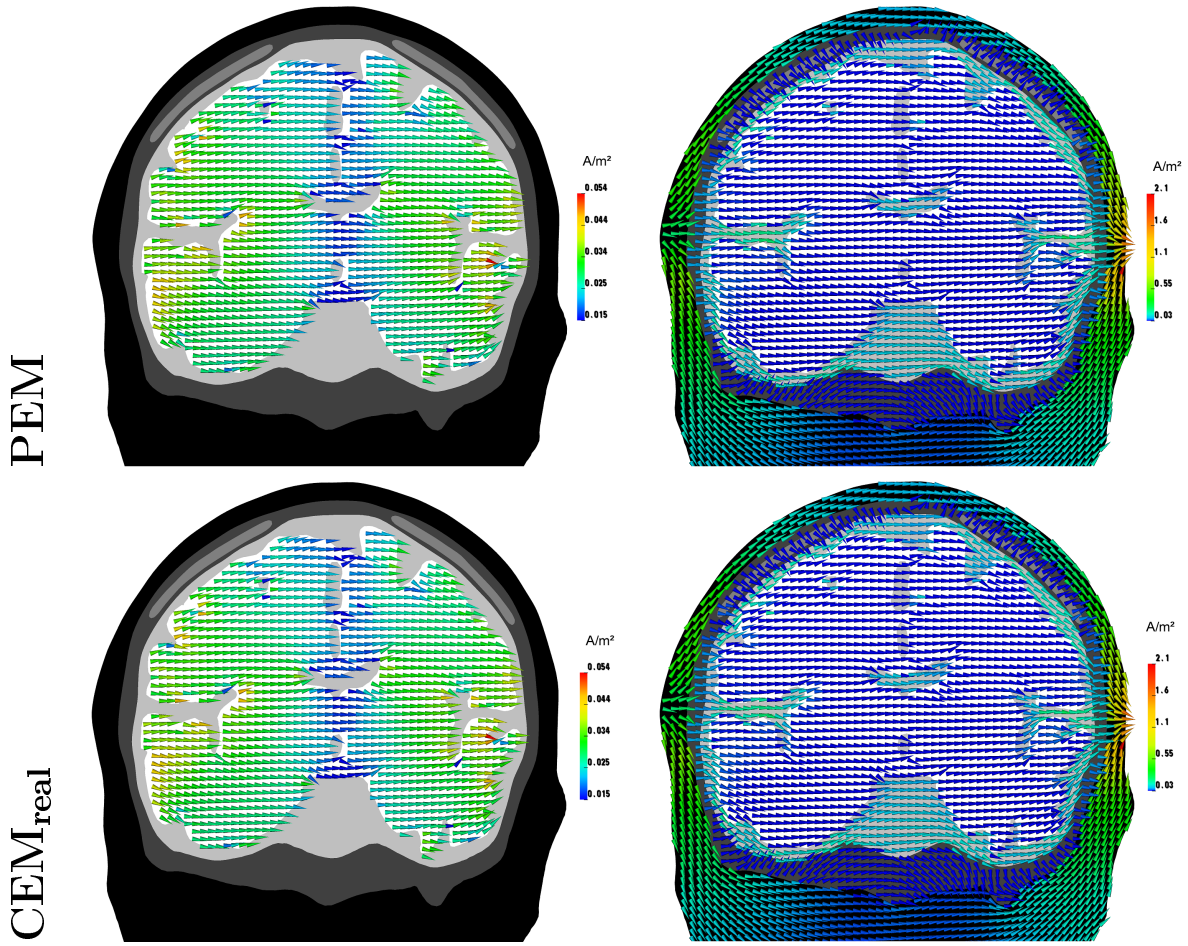


***Figure 6.10.:*** *Currents in brain and head (PEM and CEM)*

see that parts of the current pass the skull and stimulate certain brain regions like the auditory cortex.
Again, we see that patterns look extremely similar. Hence, to get an idea of the actual differences, angle and magnitude differences were calculated directly.

### 6.2.2. Angle and magnitude differences

| | $B$ | | $\Omega$ | |
|---|---|---|---|---|
| | Min | Max | Min | Max |
| $\mathbf{CEM_{real}}$ vs. **PEM** | $3.72° \cdot 10^{-6}$ | 0.040° | $8.54° \cdot 10^{-7}$ | 1.038° |
| **C/P** vs. **PEM** | $3.56° \cdot 10^{-6}$ | 0.041° | 0° | 0.205° |
| $\mathbf{CEM_{real}}$\|**C/P** | $1.48° \cdot 10^{-6}$ | 0.024° | 0° | 1.036° |

| | $B$ | | $\Omega$ | |
|---|---|---|---|---|
| | Min | Max | Min | Max |
| $\mathbf{CEM_{real}}$ vs. **PEM** | −0.086% | 0.010% | −1.707% | 1.313% |
| **C/P** vs. **PEM** | −0.041% | 0.036% | −0.458% | 0.353% |
| $\mathbf{CEM_{real}}$\|**C/P** | −0.059% | −0.003% | −1.715% | 1.300% |

***Table 6.5.:*** *Maximal and minimal angle(top) magnitude(bottom) differences in brain and head*

Maximal and minimal angle und magnitude differences are presented in Table 6.5. Unsurprisingly, currents differ the most when the $\text{CEM}_{\text{real}}$ is compared to the PEM, but even then differences lie below 2 % and 2°, respectively. In case of the brain - which is the more interesting part in case of brain stimulation - differences are even below 0.01 % and 0.05°, respectively. In contrast to the whole head, lowest differences are given for the comparison between $\text{CEM}_{\text{real}}$ and $C/P$ here. Hence, it seems that in this case the choice of the model of brain stimulation has a stronger influence than the choice of the EEG measurement model. However, differences in the brain are small enough to be ignored in all cases.
Figure 6.11 gives an impression of the distribution of angle and magnitude differences in head and brain using the example of $\text{CEM}_{\text{real}}$ vs. PEM. One can observe here, as well, that differences occur mainly on the skin, but hardly in the brain. Furthermore, differences on the skin are mainly visible next to electrodes, which corresponds to the expectations, as differences will mainly reflect shunting effects. However, this also means that shunting effects will mainly have a local influence, and differences in other parts of the head will be much lower.
Although differences in the brain are very low, patterns in the brain show that differences occur mainly near to the stimulation sides. This verifies the assumption that shunting effects at the stimulating electrodes have a bigger influence on the brain than those at the measurement electrodes.

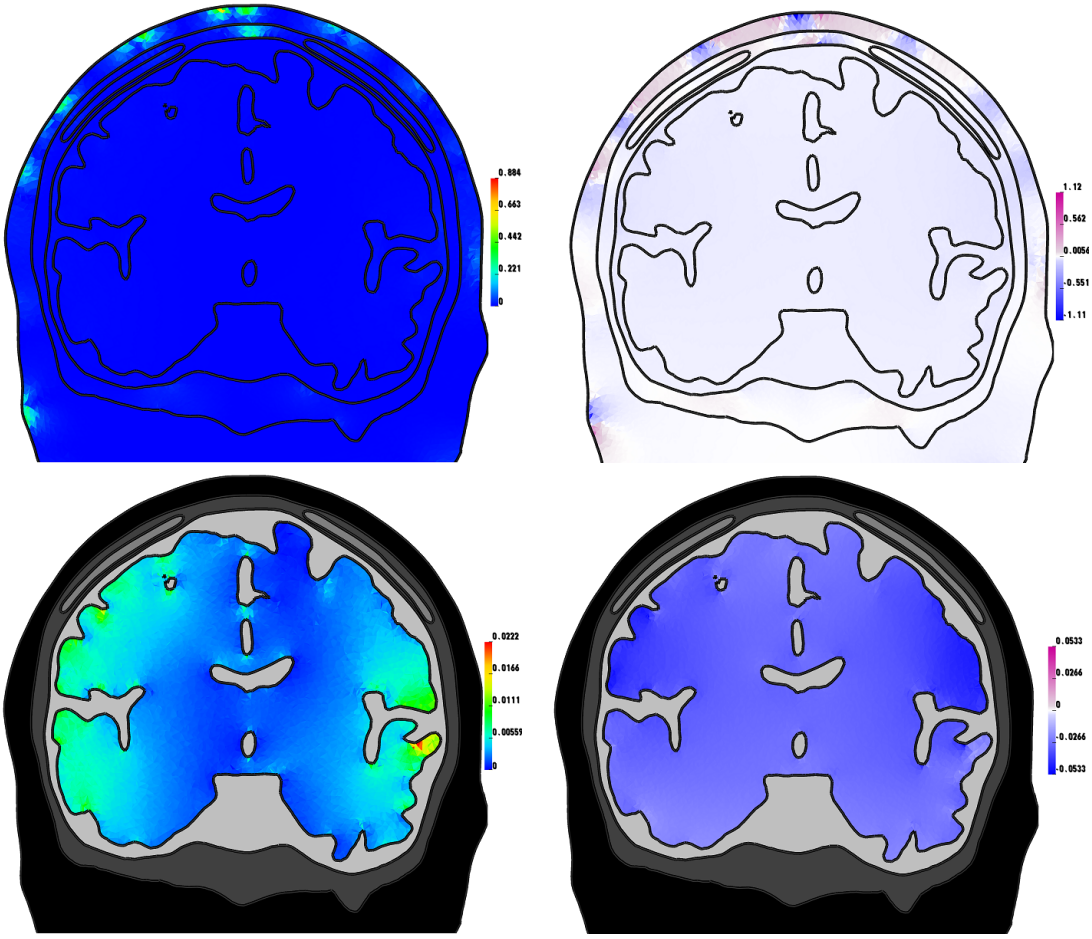


Angle differences Magnitude differences (in %)

***Figure 6.11.:*** *Currents in brain and head (PEM and CEM)*

## 6.3. Source comparisons

Section 6.1.1 gives a first impression of the differences in the brain. However, it is the focus of this thesis to work out the importance of differences for combined EEG and tCS. EEG measurements during tCS aim to measure brain activity rather than currents due to brain stimulation, but currents due to tCS interfere with brain activity. An adequate model of tCS induced EEG measurements could e.g. serve as a filter for such an interference. In this scenario even differences of small magnitude might be relevant, since brain activity is accompanied by currents which are much smaller than currents of brain stimulation. Hence, in this final section model differences are compared to some exemplary EEG measurements, induced by typical sources in the brain.
Therefore, three pairs of dipoles were localized in the primary cortices. Figure 6.12 shows these dipoles and the resulting EEG simulations. A dipole strength of 50 nV was assumed for each of the dipoles. This is a comparatively strong dipole and hence already a conservative choice.

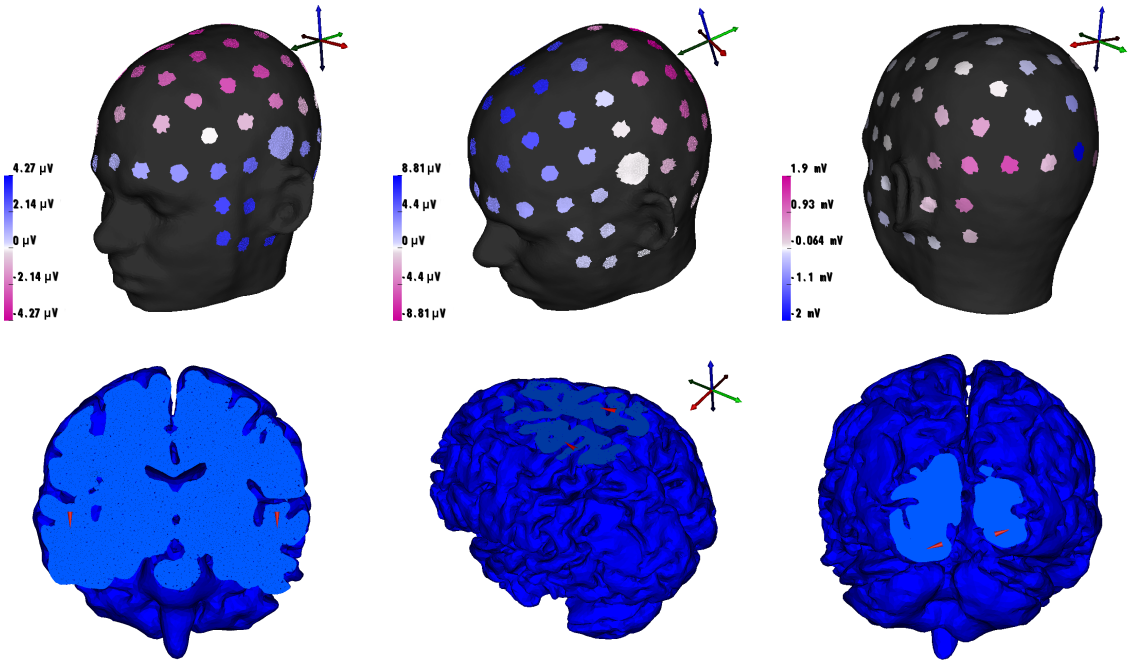


| AUD | | SOM | | VIS | |
|---|---|---|---|---|---|
| Min | Max | Min | Max | Min | Max |
| $4.27\,\mu V$ | $3.61\,\mu V$ | $-8.81\,\mu V$ | $8.13\,\mu V$ | $-2.04\,\mu V$ | $1.92\,\mu V$ |

***Figure 6.12.:*** *Primary sources (*50 nV*) and resulting EEG measurements for an assumed dipole strength of* $50nAm$*. Strongest values are presented in the attached table.*

Figure 6.13 and 6.14 show the comparison of the CEM with INF, C/I, PEM and C/P in relation to each of the three sources. To give a better impression of the caused patterns, the presented spectrum was restricted to the most common values, i.e. there are few values higher or lower than the used color scale. However, all of these values occured only in an isolated way. The actual extrema are shown in Table 6.6. Additionally, the right hand side of the table shows the most extreme values within the modified spectrum as well as the number of electrodes excluded by this spectrum which should give an impression of the uniqueness of the outlying data. Note that the excluded values are not defined as classical outliers like they are described in Appendix B. The results presented here show very disparate values in general. Hence, if classical outliers would be calculated here, a much larger number of values had to be excluded.

One can see now that the differences happen to be very high in comparison to the sources. Even the mean of the magnitudes (Table 6.6) is higher than 250% in all cases. Moreover, table 6.7 shows that for each model and each source more than one third of the electrodes show differences of more than 30%. This holds especially for $PEM$ and $C/P$. Here, nearly all differences are bigger than 100%.

However, figures 6.13 and 6.14 show that the magnitudes vary strongly. Thereby, dif-

| Comparison | | Mean($\lvert\cdot\rvert$) | Extrema Min | Extrema Max | Moderate Extrema Min | Moderate Extrema Max |
|---|---|---|---|---|---|---|
| **CEM** | • AUD | 296% | −2 654% | 4 826% | −1 706% (2) | 1 555% (1) |
| vs. | • SOM | 287% | −6 737.6% | 2 776% | −935% (1) | 1 595% (1) |
| **Inf** | • VIS | 503% | −150 460% | 23 767% | −34 340% (2) | 23 767% (0) |
| **CEM** | • AUD | 251% | −3 179% | 2 719% | −1 513% (1) | 1 328% (1) |
| vs. | • SOM | 277% | −4 361% | 2 528% | −1 475% (1) | 1 120% (1) |
| **C/I** | • VIS | 443% | −133 500% | 21 643% | −37 550% (1) | 21 643% (0) |
| **CEM** | • AUD | 8 355% | 28 930% | 396 490% | 28 930% (0) | 37 140% (1) |
| vs. | • SOM | 6 605% | −59 509% | 80 184% | −36 117% (1) | 34 354% (2) |
| **PEM** | • VIS | 109 340% | −2 552 300% | 1 329 200% | 1 439% (1) | 5 340% (2) |
| **CEM** | • AUD | 8 383% | 28 890% | 367 860% | 28 890% (0) | 37 390% (1) |
| vs. | • SOM | 6 634% | −60 053% | 79 834% | −36 563% (1) | 34 585% (2) |
| **C/P** | • VIS | 110 180% | −2 549 000% | 1 357 000% | −1 473% (1) | 6 948% (1) |

***Table 6.6.:*** Top: *Highest and lowest results of source comparisons. The most extreme values are presented in the middle. Alternative extrema can be seen on the right hand side. The brackets behind the alternative values show the number of values higher or lower, respectively. Furthermore the mean of absolute values is presented on the left hand side.*

| Comparison | AUD >30% | AUD >100% | SOM >30% | SOM >100% | VIS >30% | VIS >100% |
|---|---|---|---|---|---|---|
| **CEM** vs. **Inf** | 52 | 31 | 43 | 32 | 75 | 65 |
| **CEM** vs. **C/I** | 48 | 20 | 52 | 29 | 75 | 68 |
| **CEM** vs. **PEM** | 78 | 77 | 78 | 72 | 78 | 78 |
| **CEM** vs. **C/P** | 77 | 76 | 78 | 72 | 79 | 78 |

***Table 6.7.:*** *Number of electrodes showing a magnitude difference of more than* 30 *or* 100 *percent, respectively. Presented for each model comparison and source.*

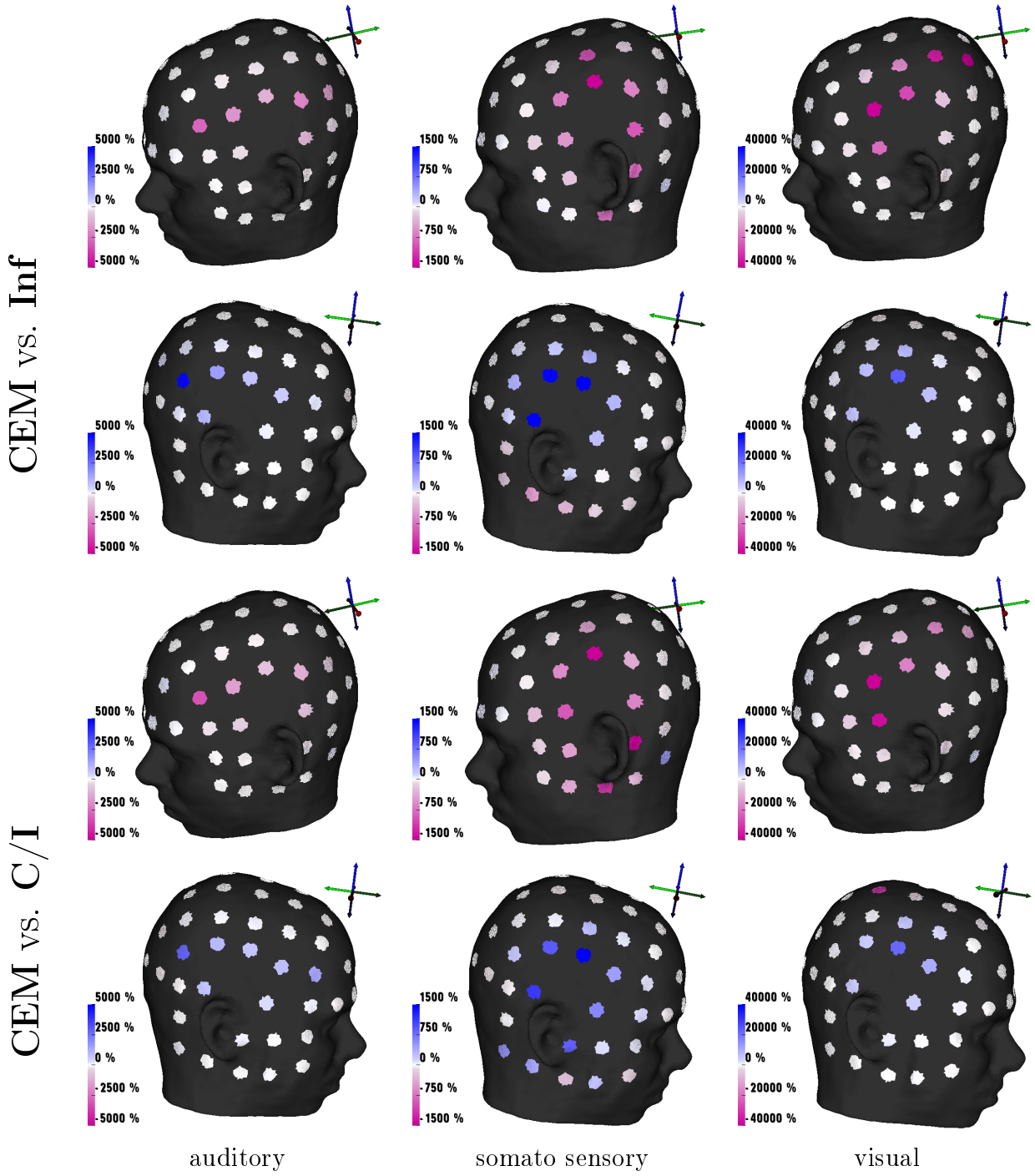


***Figure 6.13.:*** *Comparison between CEM/INF and CEM/C/I differences and the primary sources*

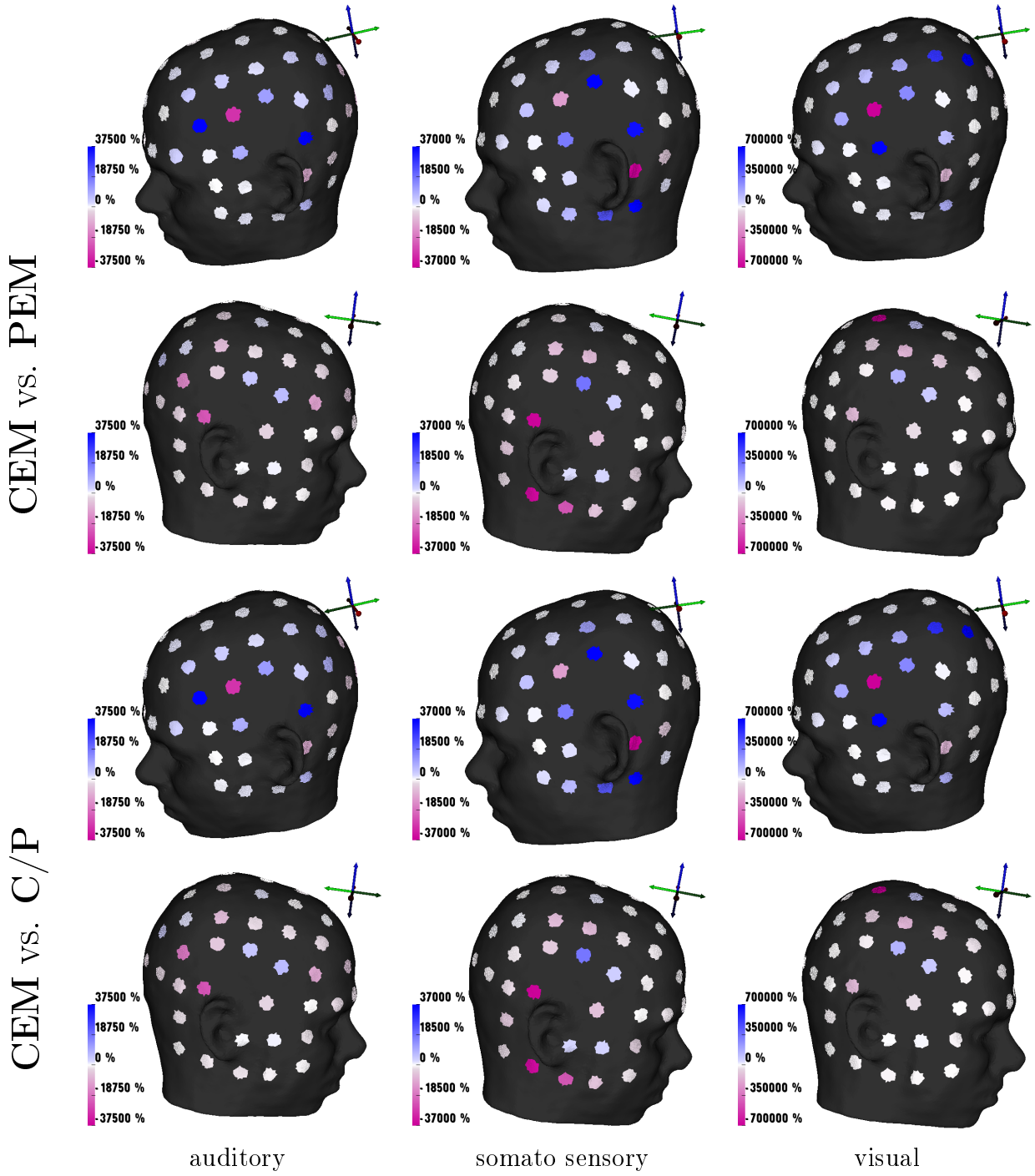


***Figure 6.14.:*** *Comparison between CEM/PEM and CEM/C/P differences and the primary sources*

ferences are strongest on electrodes with a weak source induced potential. This makes sense, since we divide by very low values again (cf. section 6.1.1). Additionally, the magnitude of difference is influenced by the distance to the stimulating electrodes, since the electrode potentials are generally higher here. Moreover, it can be seen here again, that potential differences involving the PEM tend to differ in polarities, while this not the case for the infinite models. This is due to the fact that differences occuring in context of the PEM depend mainly on the choice of the point electrode, instead of shunting effects.
The divison by values close to zero gives an explanation for the very high results, but also leads to the thought that results are not very reliable if calculated this way. To get more expressive results, it makes sense to divide each electrode difference by a constant value instead. Therefor one can take a typical EEG value again. To make the estimation as conservative as possible, the biggest magnitude of EEG source simulations was used here. Here, this is the minimum of the potentials induced by the somato sensory source. The results of the comparisons can be seen in Figure 6.15, while Table 6.8 presents the biggest values. Due to the choice of the reference it is no surprise that the values are much lower than before. Anyway, results are still big enough to be seen as significant. Table 6.9 displays the number of electrodes showing differences bigger than 30% or 100%: Again the results are most obvious in case of comparisons with PEM and C/P. Still almost all electrodes show values above 30% and most are even beyond 100%. But even in case of INF and C/I it holds that a relevant part of the electrodes shows a significantly different behavior.

| Comparison | Mean($\lvert\cdot\rvert$) | Extrema | | Moderate Extrema | |
|---|---|---|---|---|---|
| | | Min | Max | Min | Max |
| **CEM** vs. **Inf** | 40% | −255% | 385% | −255% (0) | 385% (0) |
| **CEM** vs. **C/I** | 35% | −164% | 236% | −164% (0) | 236% (0) |
| **CEM** vs. **PEM** | 765% | −5 747% | 7 300% | −3 369% (1) | 2 621% (1) |
| **CEM** vs. **C/P** | 771% | 5 818% | 7 350% | −3 400% (1) | 2 702% (1) |

***Table 6.8.:*** *Highest and lowest results for model comparisons compared to the constant value* $\min U(SOM)$*. Extrema on the right hand side exclude the strongest outliers. The mean of the absolute values is presented on the left hand side.*

| $\mathbf{CEM_{real}}$ vs. **Inf** | | $\mathbf{CEM_{real}}$ vs. **C/I** | | $\mathbf{CEM_{real}}$ vs. **PEM** | | $\mathbf{CEM_{real}}$ vs. **C/P** | |
|---|---|---|---|---|---|---|---|
| >30% | >100% | >30% | >100% | >30% | >100% | >30% | >100% |
| 24 | 10 | 22 | 11 | 77 | 68 | 76 | 68 |

***Table 6.9.:*** *Number of electrodes showing a magnitude difference of more than* 30 *or* 100 *percent if compared to* $\min U(SOM)$*.*

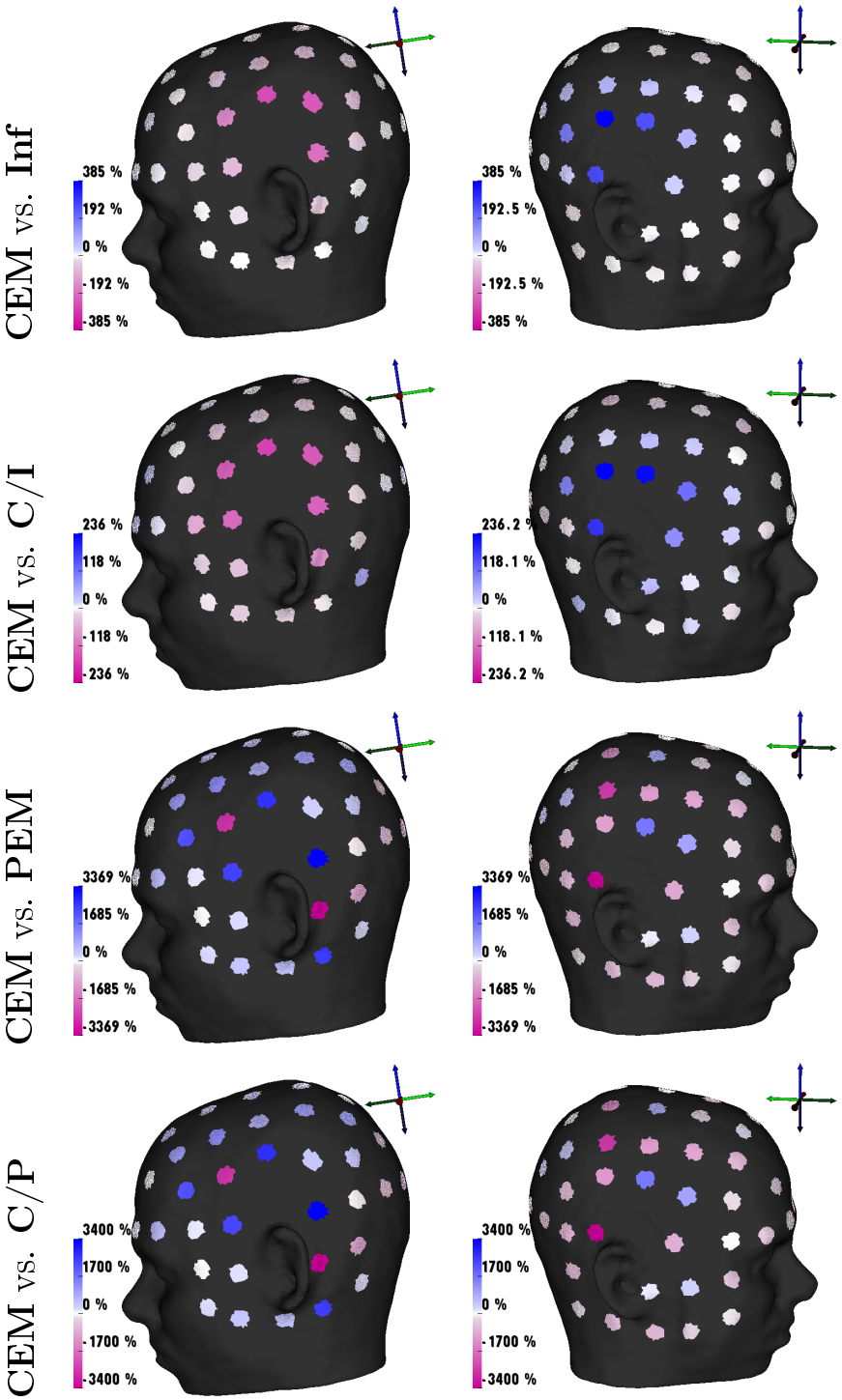


***Figure 6.15.:*** *Differences between the CEM and other models, each compared to a potential induced by brain activity* ($\min U_{SOM}$).

# 7. Discussion

This work compared different model approaches for forward simulation of combined tCS and EEG. These models include the point electrode model (PEM), the so-called gap model and the complete electrode model (CEM).
Model choice was done separately for stimulation and remaining EEG electrodes, using all three models for the normal EEG, while stimulation electrodes were modeled with CEM and gap model, respectively. Subsequently, EEG measurements, as well as current densities and potentials in head and scalp were investigated for different model combinations.
It was shown that EEG measurements do not differ significantly for all applied models, if they were described in relation to their actual magnitude (Section 6.1.1). This holds as well for distribution and magnitude of potential and currents in the head (Section 6.1.2 and 6.2). However, EEG differences were also compared to the magnitude of typical EEG measurements due to brain activity (Section 6.3). In this case, EEG differences turned out to be highly significant. This was true, even if very conservative values were chosen, i.e. the differences were divided by comparatively high activity induced EEG measurements (here a constant value of $8.81\,\mu V$).
In all investigated cases the differences between CEM and PEM turned out to be much bigger than differences between CEM and gap model. Hence, biggest differences between CEM and PEM seem to occur due to the comparable inaccurate choices of points representing the electrode potential of the PEM, rather than due to the ignorance of shunting effects described by the CEM. This can be assumed because both PEM and gap model lead to the same currents in the head, as they both do not incorporate shunting effects (cf. Section 3.1.2).

The results above imply that the relevance of the CEM depends strongly on the application of the model. For instance, usage of the CEM will not lead to significant differences in current orientation. It was shown in Section 6.2 that the orientation of currents in the head does not differ in a significant way, especially for the brain, where differences are shown to be below 0.05°. This suggests that there are no relevant differences in current distribution. Hence, for studies of stimulation focality it will not be relevant which of the presented models is used.
However, it was shown in 6.2.2 that direction differences occur mainly due to stimulation electrodes, which were only modeled by CEM and gap model here. Since the PEM also leads to much more deviant results in other cases, it is very likely that usage of the PEM will lead to higher orientation differences. This would come up to expectations, as it is a well known fact that the size of stimulation electrodes has a strong impact

on focality and current magnitudes [24]. One can therefore assume that the use of the PEM does not make much sense here, especially if large stimulation electrodes are used, which is why the PEM was not used in this work. Most actual studies incorporate size of electrodes, as well [26] [42] [48] [6]. Anyway, some studies also used the PEM in the past [15] [47].

The use of the CEM becomes more interesting when it is applied to EEG measurements in combined tES and EEG. If the application of the model deals with brain currents, the CEM will lead to significant differences.
Hence, there are several possible applications, where the model should be taken into account. For instance, in several practical studies a combination of EEG and tES is used to investigate effects of tES on brain activity [12] [57]. Since tES currents interfere with the much lower currents of brain activity, one has to filter these artifacts out. Momentarily this is done with practical methods. However, one could imagine to filter data with the help of a highly accurate model. As a matter of course, the acccuracy of the used model should lie in the range of activity induced EEG measurements. Due to the results presented in Section 6.3 it would therefore be advantageous to make use of the CEM here. However, constructing a filter this accurately would require a lot of other detailed information, especially a highly accurate head model.
Another application where the CEM might be relevant is the usage of a combined tCS and EEG model to predict conductivities, like it is done in EIT [4] [51]. Thereby, comparisons between real measurements and simulated data are used to adapt conductivities in an existing head model. This approach was already suggested in [6] and leads to a highly realistic and individual head model which can then be utilized for other applications like EEG source analysis. Obviously, such a model should be precise enough to predict brain currents accurately, and hence one can assume that usage of the CEM will lead much better results than PEM and gap model here, as well.
Despite the examples above, one cannot state that the CEM will be relevant in all cases of combined tCS and EEG modeling, as one can also imagine applications, where magnitudes of brain currents do not matter. For instance, it was also suggested in [6] to combine tES stimulations with EEG measurements to ensure safety due to stimulation. It is the idea here to predict voltage patterns on the electrodes by a highly detailed FEM model. If a fault in stimulation occurs, the patterns will change and can hence serve as an indicator that something went wrong. Differences will only matter in the range of typical tDCS induced currents and therefore the CEM will not be relevant for such an application.

It has to be pointed out here again that neither PEM nor CEM are standard models for actual tES foward modeling, although the PEM was sometimes used for stimulation in the past [15] [47]. Instead, it is very common to model electrodes as a sponge lying on the surface of the head, which is assumed to have the conductivity of saline [42]. This is due to the fact that stimulation electrodes in tCS are indeed often given by large saline soaked sponges [26]. Nevertheless, the sponge model has also been applied to disc electrodes in combination with saline gel [6] [5].Current is assumed to be applied to these sponges. Thereby, it is supposed that either the resulting potential [26] [42] or

the current density is constant over the whole electrode [6] [48]. In terms of the models described in this work, one can argue that the latter case, i.e. the assumption of constant current densities over the whole electrode, describes the application of the gap model, whereas the former case describes the CEM with a vanishing contact impedance, i.e. a model with maximal shunting currents. However, it is more likely that both approaches lead to results similar to a classical CEM, as the sponge can be seen as a respresentation of the shunting electrode. It could be interesting to investigate actual differences between the CEM and both versions of the sponge model in future work. The CEM could be an interesting alternative to the sponge model. This is due to the fact that the actual shape of the sponge is not well-known in all cases, especially for electrodes using pure saline gel instead of a classical sponge [5]. On the other hand, contact impedances on the electrodes can be measured exactly and could therefore deliver a more accurate result. However, one has to be aware that the CEM uses a simplification as well, namely the assumption of a constant ECI over the electrode. This is necessary as one has to calculate the ECI with respect to the actual contact impedance (cf. Section 3.1.2). Hence, it would be an interesting goal for future investigations to compare the accuracy of both models pertaining to real data.

The code used here calculates the resistivity matrices for every given case and directly applies them to a given stimulation pattern, which leads to a specific output of resulting potentials. However, under specific circumstances it could be advantegous to concentrate on the resistivity matrices instead: For instance, former modeling studies concerning combined EEG and tCS have suggested the use of small high-definition electrodes for the stimulation instead of large sponge electrodes, to increase precision [6]. Such electrodes can be used as both stimulation electrodes and common EEG electrodes. In this case several stimulating configurations can be investigated with the same installation of electrodes. Hence, if resistivity matrices would be calculated instead of specific potential distributions, it would only be necessary to do calculations once. The resulting matrix could then be applied to every desired configuration of stimulating electrodes. This way, effects of different stimulation configurations could be studied easily. As a matter of course, it would be necessary to apply the same model (i.e. CEM or gap model) to all involved electrodes.

As a conclusion it can be said that the application of the CEM, PEM and gap model seems to be an interesting alternative for combined EEG and tES studies. Thereby, it depends strongly on the situation, if usage of CEM and PEM (or gap model) lead to significantly different results: If EEG measurements take voltages into account induced by brain activity, it is advantegous to use the CEM. Otherwise, the use of PEM or gap might be sufficient. Future goals could incorporate real data or investigate other stimulation configurations.

# List of Figures

# List of Tables

# Bibliography


[1] H. W. Alt. *Lineare Funktionalanalysis: Eine anwendungsorientierte Einführung*. Springer-Verlag, Berlin Heidelberg New York, 5 edition, 2006.

[2] P. S. Boggio, R. Ferrucci, F. Mameli, D. Martins, O. Martins, M. Vergari, L. Tadini, E. Scarpini, F. Fregni, and A. Priori. Prolonged visual memory enhancement after direct current stimulation in alzheimer's disease. *Brain Stimulation*, pages 223–230, 2012.

[3] D. Braess. *Finite Elemente: Theorie, schnelle Löser und Anwendungen in der Elastizitätstheorie*. Springer-Verlag, Berlin Heidelberg New York, 4 edition, 2007.

[4] K.-S. Cheng, D. Isaacson, J. C. Newell, and D. G. Gisser. Electrode models for electric current computed tomography. *IEEE transactions on biomedical engineering*, 36:918–923, 1989.

[5] A. Datta, V. Bansal, J. Diaz, J. Patel, D. Reato, and M. Bikson. Gyri–precise head model of transcranial dc stimulation: Improved spatial focality using a ring electrode versus conventional rectangular pad. *Brain stimulation*, 2:201–207, 2009.

[6] A. Datta, X. Zhou, Y. Su, L. C. Parra, and M. Bikson. Validation of finite element model of transcranial electric stimulation using scalp potentials: implications for clinical dose. *Journal of neural engineering*, 10, 2013.

[7] J. P. Dmochowski, A. Datta, Y. Huang, J. D. Richardson, M. Bikson J. Fridriksson, and L. C. Parra. Targeted transcranial direct current stimulation for rehabilitation after stroke. *Neuroimage*, 75:12–19, 2013.

[8] H. Elman, D. Silvester, and A. Wathen. *Finite Elements and Fast Iterative Solvers - with Applications in Incompressible Fluid Dynamics*. Oxford University Press, New York, 2 edition, 2014.

[9] F. Fregni, P. S. Boggio, M. C. Santos, M. Lima, A. L. Vieira, S. P. Rigonatti, M. T. Silva, E. R. Barbosa, M. A. Nitsche, and A. Pascual-Leone. Noninvasive cortical stimulation with transcranial direct current stimulation in parkinson's disease. *Movement disorders*, 21:1693–1702, 2006.

[10] D. G. Gisser, D. Isaacson, and J. C. Newell. Theory and performance of an adaptive current tomography system. *Clinical Physics and Physiological Measurement*, 9:35, 1988.

[11] B. Guleyupoglua, P. Schestatsky, D. Edwards, F.Fregni, and M. Bikson. Classification of methods in transcranial electrical stimulation (tes) and evolving strategy from historical approaches to contemporary innovations. *Journal of Neuroscience Methods*, 219:297–311, 2013.

[12] R. F. Helfrich, H. Knepper, G. Nolte, D. Strüber, S. Rach, C. S. Herrmann, T. R. Schneider, and A. K. Engel. Selective modulation of interhemispheric functional connectivity by hd-tacs shapes perception. *PLoS Biol*, 12, 2014.

[13] C. Hermann, S. Rach, T. Neuling, and D. Strüber. Transcranial alternating current stimulation: a review of the underlying mechanisms and modulation of cognitive processes. *Frontiers in Human Neuroscience*, 7, 2013.

[14] M. Hämäläinen, R. Hari, R. J. Ilmoniemi, J. Knuutila, and O. V. Lounasmaa. Magnetoencephalography - theory, instrumentation, and applications to noninvasive studies of the working human brain. *Reviews of Modern Physics*, 65:413, 1993.

[15] R. N. Holdefer, R. Sadleir, and M. J. Russell. Predicted current densities in the brain during transcranial electrical stimulation. *Clinical Neurophysiology*, 117:1388–1397, 2006.

[16] S. A. Huettel, A. W. Song, and G. McCarthy. *Functional Magnetic Resonance Imaging*. Sinauer Associates, Sunderland, Massachusetts, 2 edition.

[17] A. H. Javadi and V. Walsh. Transcranial direct current stimulation (tdcs) of the left dorsolateral prefrontal cortex modulates declarative memory. *Brain Stimulation*, 5:231–241, 2012.

[18] V. John. Theorie und Numerik Partieller Differentialgleichungen - Kapitel 5.4. Lecture notes, Weierstrass Institute for Applied Analysis and Stochastics, 2006/2007. `http://www.wias-berlin.de/people/john/LEHRE/TH_NUM_PDE/th_num_pde_WS0607.pdf`.

[19] H. Kimura, M. Kurimura, K. Kurokawa, U. Nagaoka, S. Arawaka, M. Wada, T. Kawanami, K. Kurita, and T. Kato. A comprehensive study of repetitive transcranial magnetic stimulation in parkinson's disease. *ISRN Neurology*, 2011.

[20] J. P. Lefaucheur, A. Antal, R. Ahdab, D. Ciampi de Andrade, F. Fregni, E. M. Khedr, M. Nitsche, and W. Paulus. The use of repetitive transcranial magnetic stimulation (rtms) and transcranial direct current stimulation (tdcs) to relieve pain. *Brain Stimulation*, 1:337–344, 2008.

[21] D. Liebetanz, M. A. Nitsche, F. Tergau, and W. Paulus. Pharmacological approach to the mechanisms of transcranial dc-stimulation-induced after-effects of human motor cortex excitability. *Brain*, 125:2238–2247, 2002.

[22] S. J. Luck. *An Introduction to the Event-Related Potential Technique*. The MIT Press, Cambridge, Massachusetts, 2005.

[23] J.-A. Maller. *Systems Engineering*. Manz-Verlag Schulbuch (Fortis), Wien, 2000.

[24] P. Minhas, V. Bansal, J. Patel, J. S. Ho, J. Diaz, A. Datta, and M. Bikson. Electrodes for high-definition transcutaneous dc stimulation for applications in drug-delivery and electrotherapy, including tdcs. *Journal of Neuroscience methods*, 190:188–197, 2010.

[25] C. Miniussi, J. A. Harris, and M. Ruzzoli. Modelling non-invasive brain stimulation in cognitive neuroscience. *Neuroscience and Biobehavioral Reviews*, 37:1702–1712, 2013.

[26] P. C. Miranda, M. Lomarev, and M. Hallett. Modeling the current distribution during transcranial direct current stimulation. *Clinical Neurophysiology*, 107:1623–1629, 2006.

[27] M. Mohr. *Simulation of bioelectric fields: the forward and inverse problem of electroencephalographic source analysis.* Institut für Informatik, Friedrich-Alexander-Universität Erlangen-Nürnberg, 2004.

[28] M. Nitsche and W. Paulus. Excitability changes induced in the human motor cortexes by weak transcranial direct current stimulation. *Journal of Physiology*, 527:633–639, 2000.

[29] M. A. Nitsche, F. Fregni P. S. Boggio, and A. Pascual-Leone. Treatment of depression with transcranial direct current stimulation (tdcs): A review. *Experimental Neurology*, 219:14–19, 2009.

[30] W. Nolting. *Grundkurs Theoretische Physik 3: Elekrodynamik.* Verlag Zimmermann-Neuanfang, Ulmen, 2 edition, 1992.

[31] P. L. Nunez and R. Srinivasan. *Electric Fields of the Brain: The Neurophysics of EEG.* Oxford University Press, Madison Avenue, New York, New York, 2 edition, 2006.

[32] M. Ohlberger. Numerik partieller differentialgleichungen i. Lecture notes, Westfälische Wilhelms-Universität Münster, 2008/2009.

[33] J. O. Ollikainen, M. Vauhkonen, P. A. Karjalainen, and J. P. Kaipio. Effects of electrode properties on eeg measurements and a related inverse problem. *Medical engineering & Physics*, 22:535–545, 2000.

[34] T. Papadopoulo, S. Vallaghe, and M. Clerc. The adjoint method for general eeg and meg sensor-based lead field equations. *17th International Conference on Biomagnetism Advances in Biomagnetism – Biomag2010*, pages 105–108, 2010.

[35] W. Paulus. Transcranial electrical stimulation. *Neuropsychological Rehabilitation*, 21(5):602–617, 2011.

[36] R. Plonsey and D. B. Heppner. Considerations of quasi-stationarity in electrophysiological systems. *The bulletin of mathematical biophysics*, 29:657–665, 1957.

[37] A. Priori, A. Berardelli, S. Rona, N. Accornero, and M. Manfredi. Polarization of the human motor cortex through the scalp. *Neuro Report*, 9:2257–2260, 1998.

[38] S. Pursiainen. Raviart–thomas-type sources adapted to applied eeg and meg: implementation and results. *Inverse problems*, 28, 2012.

[39] S. Pursiainen, F. Lucka, and C. H. Wolters. Complete electrode model in eeg: relationship and differences to the point electrode model. *Physics in Medicine and Biology*, 57:999–1017, 2012.

[40] S. Pursiainen, A. Sorrentino, C. Campi, and M. Piana. Forward simulation and inverse dipole localization with the lowest order raviart—thomas elements for electroencephalography. *Inverse problems*, 27, 2011.

[41] D. Purves, G. J. Augustine, D. Fitzpatrick, W. C. Hall, A.-S. LaMantia, J. O. McNamara, and S. M. Williams. *Neuroscience*, pages 4–11,15,18. Sinauer, Sunderland, Massachusetts, 3 edition, 2004.

[42] S. M. Rampersad, D. F. Stegeman, and T. F. Oostendorp. Single-layer skull approximations perform well in transcranial direct current stimulation modeling. *IEEE Transactions on neural systems and rehabilitation engineering*, 21:346–353, 2013.

[43] G. Rutherford, R. Gole, and Z. Moussavi. rtms as a treatment of alzheimer's disease with and without comorbidity of depression: A review. *Neuroscience Journal*, 2013.

[44] H. P. Schwan and C. F. Kay. The conductivity of living tissues. *The electrophysiology of the heart*, 65:1007–1013, 1957.

[45] B. Schweizer. *Partielle Differentialgleichungen: Eine anwendungsorientierte Einführung*, page 128. Springer-Verlag, Berlin Heidelberg New York, 1 edition, 2013.

[46] E. Somersalo, M. Cheney, and D. Isaacson. Existence and uniqueness for electrode models for electric current computed tomography. *SIAM Journal on Applied Mathematics*, 52:1023–1040, 1992.

[47] H. S. Suh, S. H. Kim, W. H. Lee, and T.-S. Kim. Realistic simulation of transcranial direct current stimulation via 3-d high-resolution finite element analysis: Effect of tissue anisotropy. *IEEE Engineering in Medicine and Biology Society*, pages 638–641, 2009.

[48] H. S. Suh, S. H. Kim, W. H. Lee, and T. S. Kim. Realistic simulation of transcranial direct current stimulation via 3-d high-resolution finite element analysis: Effect of tissue anisotropy. *IEEE Engineering in Medicine and Biology Society*, pages 638–641, 2009.

[49] M. Tepel. *Neuroanatomie: Struktur und Funktion*, pages 221,269. Elsevier GmbH, München, 5 edition, 2012.

[50] G. Thut, P. Schyns, and J. Gross. Entrainment of perceptually relevant brain

oscillations by non-invasive rhythmic stimulation of the human brain. *Frontiers in Psychology*, 2011.

[51] M. Vauhkonen. *Electric impedance tomography and prior information*. PhD thesis, Department of Applied Physics, University of Kuopio, Kuopio, 1997.

[52] S. Wagner. An adjoint fem approach for the eeg forward problem. Diplomarbeit, Westfälische Wilhelms-Universität Münster, 2011.

[53] S. Wagner, S. M. Rampersad, Ü. Aydin, J. Vorwerk, T. F. Oostendorp, T. Neuling, C. S. Herrmann, and D. F. Stegeman. Investigation of tdcs/tacs volume conduction effects in a highly realistic head model. *Journal of neural engineering*, 11, 2013.

[54] N. Weiduschat, A. Thiel, I. Rubi-Fessen, A. Hartmann, J. Kessler, P. Merl, L. Kracht, T. Rommel, and W. D. Heiss. Effects of repetitive transcranial magnetic stimulation in aphasic stroke: a randomized controlled pilot study. *Stroke*, 42:409–415, 2011.

[55] D. Werner. *Einführung in die höhere Analysis: Topologische Räume, Funktionentheorie, Gewöhnliche Differentialgleichungen, Maß- und Integrationstheorie, Funktionalanalysis*, page 322. Springer-Verlag, Berlin Heidelberg New York, 1 edition, 2006.

[56] C. H. Wolters, L. Grasedyck, and W. Hackbusch. Efficient computation of lead field bases and influence matrix for the fem-based eeg and meg inverse problem. *Inverse problems*, 20:1099–1116, 2004.

[57] T. Zaehle, S. Rach, and C. S. Herrmann. Transcranial alternating current stimulation enhances individual alpha activity in human eeg. *PLoS One*, 5, 2010.

# A. Proof of Proposition 3.1

Since the PEM is a standard Neumann problem, the existence of a solution for 3.20 is well known. Hence the proof of proposition 3.1 will mainly follow a standard proof for the Neumann boundary conditions, like it is described in [45] or [18]. It will be shown that the solvability of the CEM can be proofed in a very similar way. For an alternative proof concerning 3.21 see [46].

The proof is based on the Fréchet-Riesz theorem (see e.g. [55] [3]):

**Theorem A.1 (*Fréchet-Riesz theorem*)**

*Let $H$ be a hilbert space and $f : H \longrightarrow \mathbb{R}$ be a linear and continuous functional. Then a unique element $u \in H$ exists with*

$$f(\varphi) = \langle \varphi, u \rangle_H \quad \forall \varphi \in H$$

Moreover, the following theorem will be needed, which is e.g. proofed in [18][1]:

**Theorem A.2 (*Variation of the Poincaré inequality*)**

*Let $\Omega' \subseteq \Omega$ with $|\Omega'| > 0$. Then for all $u \in H^1(\Omega)$ it holds:*

$$\|u\|^2_{H^1(\Omega)} \leq C \left| \int_{\Omega'} u \, \mathrm{d}V \right|^2 + |u|^2_{H^1(\Omega)}$$

**Proof of proposition 3.1 :** .

**Step 1 (Restriction to a subspace):** We will first show that it will suffice to make sure that there exist unique solutions $u_{P_0}$ and $u_{\hat{C_0}} = (u_{C_0}, U_{C_0})$ for both cases in the linear subspaces $\mathcal{W}_P \subset X$ and $\mathcal{W}_C \subset X \times \mathbb{R}^L$, which are defined as follows:

$$\mathcal{W}_P := \{\varphi_0 = \varphi - c_\varphi | \, \varphi \in X\}, \quad \mathcal{W}_C := \mathcal{W}_P \times \mathbb{R}^L$$

at which $c_\varphi = \frac{1}{|\Omega|} \int_\Omega \varphi \, \mathrm{d}V$ is constant.
To show this we assume:

$$\beta_P \left(u_{P_0}, \varphi_0\right) = f_P \left(\varphi_0\right) \quad \forall \varphi_0 \in \mathcal{W}_P \tag{A.1}$$

$$\beta_C \left(u_{C_0}, U_{C_0}, \varphi_0, \Phi\right) = f_C(\varphi_0, \Phi) \quad \forall (\varphi_0, \Phi) \in \mathcal{W}_C \tag{A.2}$$

[1] In fact it is stated there that the theorem holds for $\Omega' \subset \Omega$. However, the proof shows that it is also true for $\Omega' = \Omega$

It follows directly that in both cases the equation will also hold for all $\varphi \in X$ and $(\varphi, \Phi) \in X \times \mathbb{R}^L$ respectively:

Every function $\varphi \in X$ can be written as

$$\varphi = \varphi_0 + c_\varphi \tag{A.3}$$

with $\varphi_0 \in \mathcal{W}_P$. Then for abitrary $(\varphi, \Phi) \in X \times \mathbb{R}^L$ we can write:

$$(\varphi, \Phi) = (\varphi_0, \Phi - c_{L_\varphi}) + (c_\varphi, c_{L_\varphi}) \tag{A.4}$$

with $c_{L_\varphi} := (c_\varphi, \ldots, c_\varphi) \in \mathbb{R}^L$.

Since $\int_\Omega \nabla \cdot J^p \, \mathrm{d}V = \sum_{l=1}^L I_l$ it holds:

$$f_P(c_\varphi) = 0 = \beta_P(u, c_\varphi) \quad \text{and} \quad f_C(c_\varphi, c_{L_\varphi}) = 0 = \beta_C(u, U, c_\varphi, c_{L_\varphi})$$

Therefore:

$$\beta_P(u_{P_0}, \varphi) = \beta_P(u_{P_0}, \varphi_0) + \beta_P(u_{P_0}, c_\varphi) = f_P(\varphi_0) + f_C(c_\varphi) = f_P(\varphi)$$

Analogously:

$$\begin{aligned} \beta_C(u_C, U_C, \varphi, \Phi) &= \beta_C(u_C, U_C, \varphi_0, \Phi - c_{L_\varphi}) + \beta_C(u_C, U_C, c_\varphi, c_{L_\varphi}) \\ &= f_C(\varphi_0, \Phi - c_{L_\varphi}) + f_C(c_\varphi, c_{L_\varphi}) \\ &= f_C(\varphi, \Phi) \end{aligned}$$

This shows both A.1 and A.2 hold for all $\varphi \in X / \hat{\varphi} \in X \times \mathbb{R}$. If there is a $u_P = (u_{P_0} + c) \in \mathcal{W}_P$ or a $\hat{u_C} = (u_{C_0} + c_{L+1}) \in \mathcal{W}_C \times \mathbb{R}$ now, $u_p$, $\hat{u_C}$ are solutions of 3.20 or 3.21 respectively. This holds because $\beta_P(c, \phi) = 0$, $\beta_C(c_{L+1}, \phi) = 0$, obviously. In particular, such solutions exist because of the definition of $\mathcal{W}_P$.
The proof shows, additionally, that for any other solution $\phi$ or $\hat{\phi}$ of these equations which can't be described by $u_{P_0} + c$ or $\hat{u_{C_0}} + c_L$, we could find another $\tilde{u}$ in $\mathcal{W}_P / \mathcal{W}_C$, for which $\phi = \tilde{u} + c$ holds and which is a solution of 3.20/3.21. This is a contradiction, since $u_{P_0}$ and $\hat{u_{C_0}}$ are meant to be unique.
Hence if equations A.1 and A.2 are true, proposition 3.1 follows.

**Step 2 ($\mathcal{W}_P$ is a closed subspace):** If $X$ contains the family of constant functions $c$ we can see, that $\mathcal{W}_P$ is in fact the subspace:

$$\mathcal{W}_P = \{\varphi_0 \in X | \int_\Omega \varphi_0 = 0\} \subset X$$

since X is closed under addition. Moreover, $\mathcal{W}_P$ is closed, since every cauchy sequence in $\mathcal{W}_P$ converges to a $x \in X$ for which holds: $\int_\Omega x \mathrm{d}V = 0$.

If $X$ does not contain the family of constant functions, the map[2]

$$P_{\mathcal{W}_P}(\varphi) = \varphi - c_\varphi$$

is bijective: If $\varphi_1$, $\varphi_2$ are two functions with $P_{\mathcal{W}_P}(\varphi_1) = P_{\mathcal{W}_P}(\varphi_1)$, it is $\varphi_1 - \varphi_2 = c_{\varphi_1} - c_{\varphi_2}$, which is contradiction, hence $P_{\mathcal{W}_P}$ is injective. The surjectivity is clear.
This implies that there is an inverse map $P^{-1}_{\mathcal{W}_P}$, which is linear as well, and since $X$ and therefore $\mathcal{W}_P$ are finite-dimensional, $P^{-1}_{\mathcal{W}_P}$ is continuous. Because $\mathcal{W}_P$ is the preimage of the closed space $X$, $\mathcal{W}_P$ is closed as well then.

**Step 3 (Proof that $\beta_P$, $\beta_C$ are scalar products):**To proof A.1 and A.2 the preconditions of theorem A.1 have to be shown:

It shall be proofed first that $\beta_p$, $\beta_C$ are scalar products over $\mathcal{W}_P/\mathcal{W}_C$. It is obvious that $\beta_P$, $\beta_C$ define bilinear forms on $\mathcal{W}_P$ and $\mathcal{W}_C$. What remains to be shown is the positive definiteness of both forms:
It is also clear that $\beta_P(w,w) > 0$ and $\beta_C(\hat{w},\hat{w}) > 0$ for all $w \in \mathcal{W}_P$, $\hat{w} \in \mathcal{W}_C$. We assume now that for an $w \in \mathcal{W}_P$ holds:

$$\beta_P(w,w) = 0$$

With the Poincaré inequality (A.2) it is

$$\|w\|_{L^2(\Omega)} \leq C\|\nabla w\|_{L^2(\Omega)} \tag{A.5}$$

since $\int_\Omega w = 0$. It follows:

$$\|w\|_{H^1(\Omega)} \leq (C+1)\|\nabla w\|_{L^2(\Omega)} = (C+1)\beta_P(w,w) = 0 \Rightarrow w = 0$$

because $\|\cdot\|_{H^1(\Omega)}$ is a norm. Hence $\beta_P$ is positive definite.
Analogously let $\hat{w} = (w, W)$ be in such a way that

$$\beta_C(\hat{w},\hat{w}) = \|\nabla w\|_{L^2(\Omega)} + \sum_{l=1}^{L} \frac{1}{Z_l} \int_{e_l} (W_l - w)^2 \,\mathrm{d}S = 0$$

With Poincaré again:

$$\|w\|_{H^1(\Omega)} + \sum_{l=1}^{L} \frac{1}{Z_l} \int_{e_l} (W_l - w)^2 \,\mathrm{d}S \leq (C+1)\,\beta_C(\hat{w},\hat{w}) = 0$$

and it follows $w = 0$ because both summands are positive. Then we know:

$$\beta_C(\hat{w},\hat{w}) = \sum_{l=1}^{L} \frac{1}{Z_l} \int_{e_l} (W_l - w)^2 \,\mathrm{d}S = 0 \Rightarrow W_l = w = 0$$

[2]This is in fact the orthogonal projection of $\mathcal{W}_P$.

Therefore, $\beta_P$ and $\beta_C$ are scalar products over $\mathcal{W}_P$ and $\mathcal{W}_C$.

**Step 4 (Proof that $(\mathcal{W}_P, \beta_P)$, $(\mathcal{W}_C, \beta_C)$ are hilbert spaces):** We notice at first that $\mathcal{W}_P$ and $\mathcal{W}_C$ are hilbert spaces: This is because $\mathcal{W}_P$ is a closed set of the hilbert space $H^1(\Omega)$ and $\mathcal{W}_C$ is the direct sum of the hilbert spaces $\mathcal{W}_P$ and $\mathbb{R}^L$, and therefore a hilbert space concerning the natural scalar product:

$$\langle \hat{w}, \hat{x} \rangle_{\mathcal{W}_C} = \langle w, x \rangle_{\mathcal{W}_C} + \langle W, X \rangle_2$$

To proof now that $\mathcal{W}_P$,$\mathcal{W}_C$ are hilbert spaces concerning $\beta_P$ and $\beta_C$ as well, it has to be shown that both norms are equivalent to the natural norms $\|\cdot\|_{\mathcal{W}_P} \coloneqq \left(\|\cdot\|_{H^1(\Omega)}\right)_{|\mathcal{W}_P}$ and $\|\cdot\|_{\mathcal{W}_C} \coloneqq \left(\|\cdot\|_{H^1(\Omega)\times\mathbb{R}^L}\right)_{|\mathcal{W}_C}$ on $\mathcal{W}_P$ and $\mathcal{W}_C$:

$$\textbf{To be proofed:} \quad \exists\, C_{1*}, C_{1*} : C_{1*}^{-1}\|\cdot\|_{\beta_*} \leq \|\cdot\|_{\mathcal{W}_*} \leq C_{2*}\|\cdot\|_{\beta_*}$$

***Proof for*** $(\mathcal{W}_P, \beta_P)$***:***
For $(\mathcal{W}_P, \beta_P)$ the equivalence is easy to see. It is clear that:

$$\|w\|_{\beta_P}^2 = |w|_{H^1(\Omega)}^2 \leq |w|_{H^1(\Omega)}^2 + \|w\|_{L^2(\Omega)}^2 = \|w\|_{H^1(\Omega)}^2 = \|w\|_{\mathcal{W}_P}^2 \quad \forall w \in \mathcal{W}_P$$

Hence:

$$\|w\|_{\beta_P} \leq \|w\|_{H^1(\Omega)} \quad \forall w \in \mathcal{W}_P \tag{A.6}$$

Moreover, we have already stated in equation A.5 that:

$$\|w\|_{\mathcal{W}_P} = \|w\|_{H^1(\Omega)} \leq C_P|w|_{H^1(\Omega)} = C_P\|w\|_{\beta_P} \quad \forall w \in \mathcal{W}_P \tag{A.7}$$

Therefore, we have proofed that $\|\cdot\|_{\beta_C}$ is equivalent to $\|\cdot\|_{\mathcal{W}_P}$.

***Proof for*** $(\mathcal{W}_C, \beta_C)$***:***
The estimations in this part are roughly based on [46]: To proof the analogical statement in $\mathcal{W}_C$ we notice first that there is a continuous embedding $H^{1/2}(\partial\Omega) \subset L^2(\partial\Omega)$, because of the Sobolev embedding theorem as well as a continuous mapping $\gamma : H^1(\Omega) \longrightarrow H^{1/2}(\partial\Omega)$ due to the trace theorem [46]. Hence it holds:

$$\|w\|_{L^2(\partial\Omega)} \leq C'\|w\|_{H^{1/2}(\partial\Omega)} \leq C\|w\|_{H^1(\Omega)} \tag{A.8}$$

This way the first estimation can be proofed straightforward:

$$\begin{aligned}
\|w, W\|_{\beta_C}^2 &= |w|_{H^1(\Omega)}^2 + \sum_{l=1}^{L} \frac{1}{Z_l} \int_{e_l} (W_l - w)^2 \\
&\leq \|w\|_{H^1(\Omega)}^2 + \max_k \frac{1}{Z_k} \sum_{l=1}^{L} \|w\|_{L^2(e_l)}^2 + \|W_l\|_{L^2(e_l)}^2 \\
&\leq \|w\|_{H^1(\Omega)}^2 + C' \left( \|w\|_{L^2(\partial\Omega)}^2 + \sum_{l=1}^{L} |e_l| W_l^2 \right) \\
&\leq \|w\|_{H^1(\Omega)}^2 + C \left( \|w\|_{H^1(\Omega)}^2 + \|W_l\|_2^2 \right) \\
&\leq C_{C1} \left( \|w\|_{H^1(\Omega)}^2 + \|W_l\|_2^2 \right) = C_{C1}\|w, W\|_{\mathcal{W}_C}^2
\end{aligned} \tag{A.9}$$

For the other direction we assume that $\|\cdot\|_{W_C}^2 \leq C\|\cdot\|_{W_C}^2$ does not hold:

$$\textbf{Assumption:} \quad \forall C > 0 : \exists(\tilde{w}, \tilde{W}) \in \mathcal{W}_C : \|\tilde{w}, \tilde{W}\|_{W_C} > C\|\tilde{w}, \tilde{W}\|_{\beta_C} \tag{A.10}$$

Then it exists a sequence $(w'^n, W'^n)$ with:

$$\frac{\|w'^n, W'^n\|_{\beta_C}}{\|w'^n, W'^n\|_{\mathcal{W}_C}} < \frac{1}{n} \quad \forall n \in \mathbb{N}_{>0}$$

or - after normalization of $(w'^n, W'^n)$ with respect to $\|\cdot\|_{\mathcal{W}_C}$ - a sequence $(w^n, W^n)$:

$$\|w^n, W^n\|_{\mathcal{W}_C} = 1, \quad \|w^n, W^n\|_{\beta_C} < \frac{1}{n} \tag{A.11}$$

It follows:

$$\begin{aligned}
\frac{1}{n} &\geq \|w^n, W^n\|_{\beta_C} \geq \int_{e_l} (w^n - W_l^n)^2 \, \mathrm{d}S \\
&= \int_{e_l} (w^n)^2 \, \mathrm{d}S - 2W_l^n \int_{e_l} w^n \, \mathrm{d}S + \int_{e_l} (W_l^n)^2 \, \mathrm{d}S \\
&\geq -2W^n \int_{e_l} w^n \, \mathrm{d}S + \int_{e_l} (W_l^n)^2 \, \mathrm{d}S
\end{aligned}$$

which can also be written in the form:

$$|e_l| \, (W_l^n)^2 \leq 2W_l^n \int_{e_l} w^n \, \mathrm{d}S + \frac{1}{n}$$

Now because of the left hand side of A.11 it is:

$$\|W^n\|_2^2 \leq 1 - \|w^n\|_{H^1\Omega}^2 \quad \Rightarrow W_l^n \leq \left(1 - \|w^n\|_{H^1\Omega}^2\right)^{\frac{1}{2}}$$

and we receive with the Cauchy-Schwarz inequality and equation A.8:

$$\int_{e_l} w^n \, \mathrm{d}S = \langle 1, w^n \rangle_{L^2(e_l)} \leq |e_l|^{\frac{1}{2}} \|w_n\|_{L^2(e_l)} \leq c\|w^n\|_{H^1(\Omega)}$$

Hence:

$$|e_l| \, (W_l^n)^2 \leq C \left(1 - \|w^n\|_{H^1(\Omega)}^2\right)^{\frac{1}{2}} \|w^n\|_{H^1(\Omega)} + \frac{1}{n} \tag{A.12}$$

But since $w^n \in \mathcal{W}_P$, one can use Poincaré again and we get:

$$\|w^n\|_{H^1(\Omega)} \leq C|w^n|_{H^1(\Omega)} \leq C\|w^n, W^n\|_{\beta_C} < C\frac{1}{n}$$

$$\Rightarrow \lim_{n\to\infty} \|w^n\|_{H^1(\Omega)} = 0$$

With equation A.12 we can now conclude $\lim_{n\to\infty} W_l^n = 0$ as well and it follows:

$$0 = \left(\lim_{n\to\infty} \|w^n\|_{H^1(\Omega)} + \|W^n\|_2^2\right) = \lim_{n\to\infty} \|w^n, W^n\|_{\mathcal{W}_C} = 1 \quad \lightning$$

This shows that the assumption A.10 must be wrong and there exists a $C_{C2}$ with:

$$\|w, W\|_{\mathcal{W}_C} \leq C_{C2}\|w, W\|_{\beta_C} \quad \forall (w, W) \in \mathcal{W}_C \tag{A.13}$$

and because of A.9 and A.13 $\|\cdot\|_{\mathcal{W}_C}$ and $\|\cdot\|_{\beta_C}$ must be equivalent.

Hence $(\mathcal{W}_C, \beta_C)$ is a hilbert space, as well as is $(\mathcal{W}_P, \beta_P)$, at which the latter is clear because of the equivalence proofed in (A.6, A.7).

**Step 5 (Application of Fréchet-Riesz):** To make use of Riesz's theorem it is left to show that $f_P$ and $f_C$ are continuous in $\mathcal{W}_P$ or $\mathcal{W}_C$, respectively. This follows, however, with the inequality of Cauchy-Schwarz and the equivalences described above:

$$\begin{aligned}
|f_P(w)| &\leq \langle \nabla \cdot J, w \rangle_{H^1(\Omega)} + \sum_l \frac{|I_l|}{|e_l|} \langle 1, w \rangle_{L^2(e_l)} \\
&\leq \|\nabla \cdot J\|_{H^1(\Omega)} \|w\|_{H^1(\Omega)} + \sum_l \frac{|I_l|}{|e_l|^{\frac{1}{2}}} \|w\|_{L^2(e_l)} \\
&\leq C\|w\|_{H^1(\Omega)} = C\|w\|_{\mathcal{W}_P} \leq CC_P\|w\|_{\beta_P}
\end{aligned}$$

$$\begin{aligned}
|f_C(w, W)| &\leq \langle I, W \rangle_2 + \langle \nabla \cdot J, w \rangle_{H^1(\Omega)} \leq \|I\|_2 \|W\|_2 + \|\nabla \cdot J\|_{H^1(\Omega)} \|w\|_{H^1(\Omega)} \\
&\leq C \left( \|W\|_2 + \|w\|_{H^1(\Omega)} \right) \\
&= C\|w, W\|_{\mathcal{W}_C} \leq CC_{C2}\|w, W\|_{\beta_C}
\end{aligned}$$

In the first proof A.8 is used again. With Riesz' theorem A.1 follows Proposition 3.1. ■

# B. Outliers

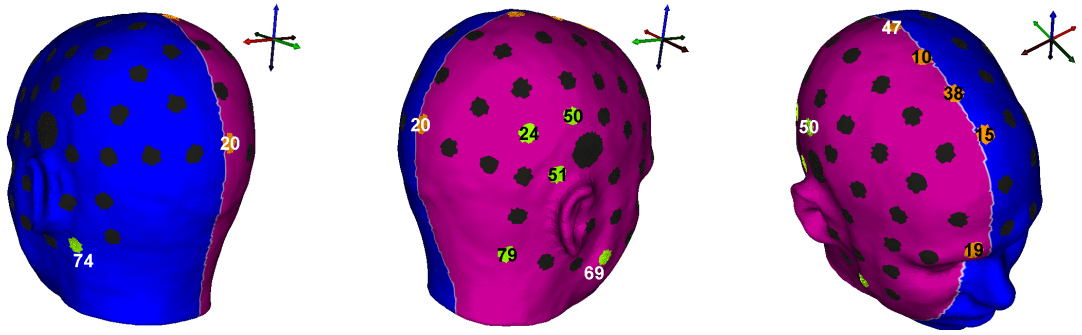


***Figure B.1.:*** *Visualization of electrodes typically showing high relative differences. The pink and blue pattern shows the polarities of the skin potential (blue: positive, pink: negative). Hence, the potential is almost zero at the 'center line'. Electrodes lying on the center line are marked orange, other electrodes showing outliers are given in green.*

When the relative differences between the involved models are calculated at each electrode, a few electrodes show conspiciously extreme values. One can observe these values in Table B.1 which presents the highest and lowest values for each model comparison described in 6.1.1. Obviously extreme values usually occure at similar electrodes in all cases. Figure B.1 shows the most noticeable ones.
A large number of high values appear at electrodes near to the 'center line', i.e. the part of the head where the potential is almost zero. Since relative differences are calculated by dividing by the absolute values at the electrodes, it is most likely that extreme values at the center line occur due to inaccuracies in computation (e.g. rounding errors). This idea is most obvious for electrode 38, which lies exactly on the center line and even shows differences of over 40 %, although no other relative differences are bigger than 3.3 %.
However, there are a few other electrodes showing a striking behavior. Some of these electrodes (24,50,51) lie next to the cathode and it is therefore likely that these electrodes show regular values as currents are very high here. Other electrodes can be found next to the ears (here labeled 74, 69 and 79). It is possible that high results at these places can be explained due to structural differences in the head model. While the first group of outliers can in fact be excluded from interpretation, the last two groups shouldn't. However, all values labeled as outliers were presented separately in Section 6.1.1 to give a better impression of common values.

| **$CEM_{real}$** vs. **C/I** | | **$CEM_{real}$** vs. **Inf** | | **$CEM_{real}$** vs. **PEM** | |
|---|---|---|---|---|---|
| Min | Max | Min | Max | Min | Max |
| **38: -1.76 %** | 79: 0.11 % | **38: -2.55 %** | 50: 0.07% | **38: -42.72 %** | 74: 3.1 % |
| **10: -0.14 %** | 78: 0.07 % | **10: -0.17%**% | 24: 0.06% | **20: - 3.15 %** % | 43: 1.56 % |
| 31: −0.09% | 69: 0.04% | **47: -0.11%** | 51: 0.05% | **19: -2.45 %** | 29: 1.1% |
| 5: −0.09% | 50: 0.04% | **19: -0.11**% | 28: 0.04% | 72: −1.69% | 14: 0.9% |
| 15: −0.06% | 18: 0.04% | **15: -0.10**% | 6: 0.03% | 1: −1.51% | 30: 0.85% |
| 47: −0.06% | 28: 0.04% | 31: -0.07% | 49: 0.03% | 73: −1.33% | 27: 0.82% |

| **$CEM_{real}$** vs. **C/P** | | **C/I** vs. **Inf** | | **C/P** vs. **PEM** | |
|---|---|---|---|---|---|
| Min | Max | Min | Max | Min | Max |
| **38: -42.67 %** | 74: 3.08% | **38: -0.8 %** | 5: 0.05% | **38: -0.08%** | **20: 0.08** % |
| **10: -3.23** % | 43: 1.57% | 79: -0.15 % | 48: -0.03% | 44: −0.02% | 59: 0.05% |
| **19: -2.43 %** | 29: 1.10% | **19:** −0.07% | 67: 0.03% | 42: −0.02% | 5: 0.04% |
| 72: −1.68% | 14: 0.90% | 69: −0.07% | 60: 0.03% | 19: −0.02% | 47: 0.03% |
| 1: −1.50% | 30: 0.85% | 78: −0.06% | 50: 0.03% | 68: −0.02% | 24: 0.03% |
| 73: −1.34% | 27: 0.81% | 47: −0.05% | 24: 0.03% | 65: −0.02% | 50: 0.03% |

| **Inf** vs. **PEM** | | **C/I** vs. **C/P** | |
|---|---|---|---|
| Min | Max | Min | Max |
| **38: -41.22 %** | 74: 3.10 % | **38: -41.64 %** | 74: 3.09% |
| **20: -3.10** % | 43: 1.60 % | **20: -3.18** % | 43: 1.60% |
| **19: -2.34** % | 29: 1.11% | **19: -2.4** % | 29: 1.11% |
| 72: -1.68 % | 14: 0.91 % | 72: -1.66 % | 14: 0.90% |
| 1: -1.51% | 30: 0.85 % | 1: -1.53 % | 30: 0.88% |
| 73: -1.31 % | 27: 0.83 % | 73: -1.31 % | 27: 0.83% |

***Table B.1.:*** *Highest and lowest relative differences for each model comparison described in 6.1.1. Numbers in the table refer to the labels of the electrodes. Bold values show peculiar values near to the center line. Underlined values are noticeable different to other values, but not localized near the center line.*

# C. CD

The applied CD contains the following contents:

- A PDF file of this work
- The folder "'main code"', which includes:
  - The mesh struct "'ms.mat"', representing the head model and necessary additional properties. The mesh was modified by Sampsa Pursiainen, but based on already existing data
  - The original code, also written by Sampsa Pursianen
  - The modified version of the code
  - A short documentation on the usage of the code
- The folder "'results"', containing the most interesting numerical results as well as a short description of the contents.
- The folder "'additionalcode"', containing the most important code used for visualization and investigation of the results
- The folder "'scirun"', containing several files, which can be used in SCIRun for visualization of results. The possible use of each file is described in the text-file in the same folder.

# Eidesstattliche Erklärung

Hiermit versichere ich, Britte Agsten, dass ich die vorliegende Arbeit selbstständig verfasst und keine anderen als die angegebenen Quellen und Hilfsmittel verwendet habe. Gedanklich, inhaltlich oder wörtlich übernommenes habe ich durch Angabe von Herkunft und Text oder Anmerkung belegt bzw. kenntlich gemacht. Dies gilt in gleicher Weise für Bilder, Tabellen, Zeichnungen und Skizzen, die nicht von mir selbst erstellt wurden.

Alle auf der CD beigefügten Programme sind, sofern nicht deutlich anderweitig gekennzeichnet, von mir selbst programmiert worden.

Münster, 16. März 2015

Britte Agsten